FUJIFILM

ISSN : 0915-1478
CODEN : FFRDEK 58, 1-164 (2013)

FUJIFILM RESEARCH & DEVELOPMENT

No.58−2013

富士フイルム研究報告

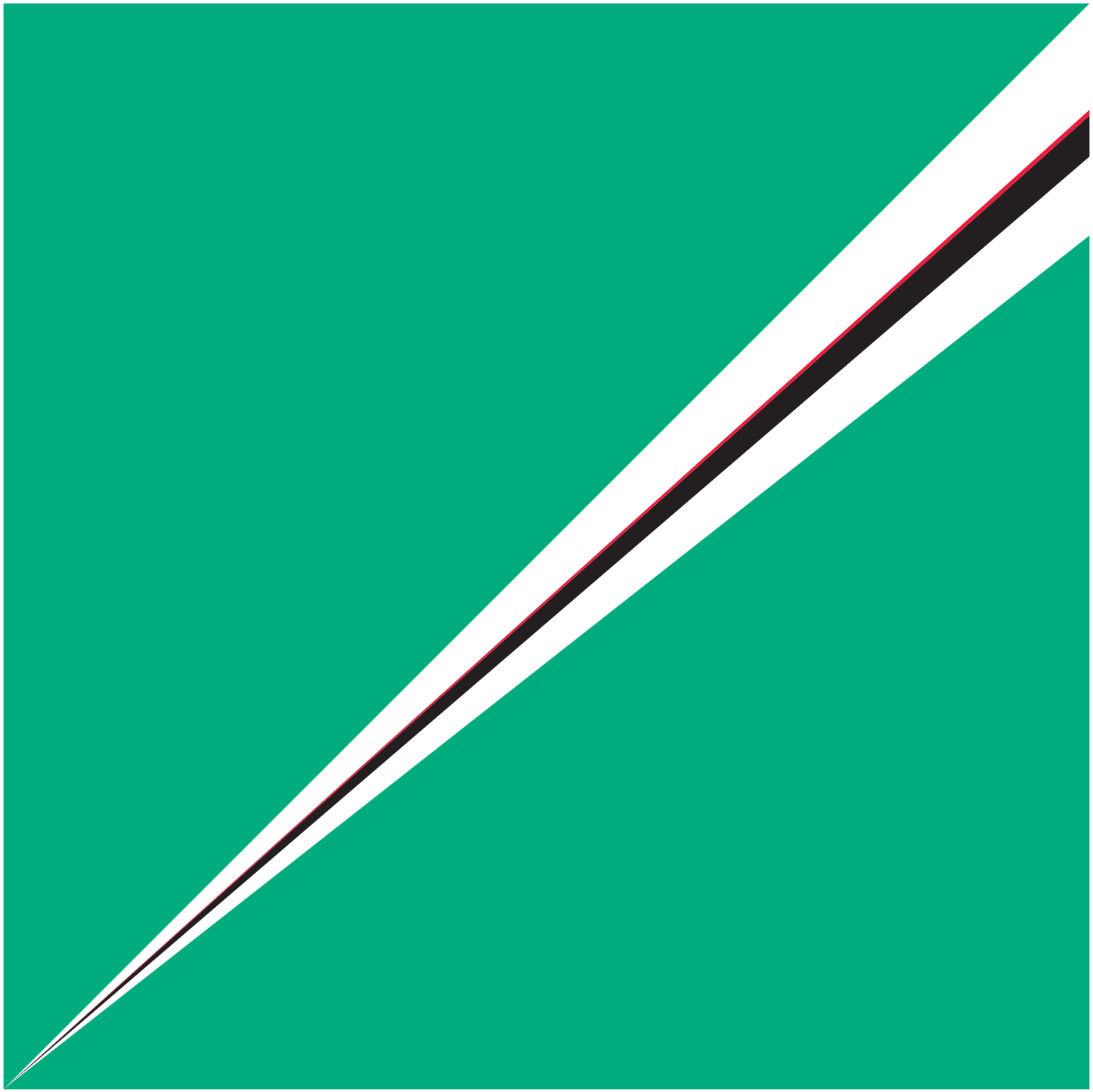

PURPOSE OF PUBLICATION

This annual publication is issued in order to introduce the results of research and development carried out in the laboratories of FUJIFILM Corporation and its subsidiaries. To provide an overview of our wide-ranging R&D activities across numerous business fields, this collection includes the papers, which are newly written or have already been published in various science and technology journals, regarding our noteworthy new products and novel technologies. In addition, a list of such papers published in journals and those presented at academic conferences in the past one year is attached at the end.

Published by Strategic Corporate Technology Planning Division,
Research & Development Management Headquarters,
FUJIFILM Corporation
Ushijima, Kaisei-machi, Ashigarakami-gun, Kanagawa 258-8577, Japan

FOREWORD

Kozo Sato
Fellow
Research & Development
Management Headquarters
FUJIFILM Corporation

Several years ago, I heard an interesting story from the President of the University of Tokyo. “The university has many scientists, the top 10% of whom are extremely talented and expected to achieve research results deserving the Nobel prize. I would like the remainder to support those top 10%,” he said. On another occasion, the CTO of a chemical company remarked that no more than 5% of researchers can get the inspiration needed to create innovative technology. I think that inspiration truly innovative and original depends upon an individual’s talent. It can not easily be acquired by training but is formed mainly by genes, environment where people were born and raised and their life-long experience. Therefore, it is unsurprising that such a talent is limited to a very small number of people.

Creating only one original technology is not always good enough. It is desirable to develop several such technologies to differentiate us from others because, in recent years, innovation takes place very rapidly and alternatives for any technology also appear very soon. To gain unrivaled competence, it is important for us to integrate several differentiated technologies. However, such integration requires careful consideration.

There is the *taru-oke* (wooden barrel) theory, which is written in the book *Karate to Ki* (Karate and Qi) by the renowned karate master, Kenji Ushiro. The theory states that, if your spiritual, technical and physical strength is 40, 80 and 60 respectively, your total strength is 120 not 180. This idea came from the fact that water in a barrel with staves of different lengths (40, 80 and 60) will leak from the shortest stave and the surface of the water comes to this shortest level. That is, you cannot fully exhibit your technical and physical strength if your spiritual strength is weaker. If an excellent technology is integrated with one or more mediocre technologies, the total power remains mediocre. FUJIFILM has an extensive range of expertise and excellent human resources in various technological domains. I would like all employees to make bold efforts for achieving higher goals to develop novel technologies.

I would also like to mention that the efficiency of research and development is important. In turning an innovative technology into products that sell well while overcoming various problems, it is essential to efficiently perform this process.

Ants are an example of social beings whose efficient behavior is well known. Most larvae that hatch from eggs laid by the queen ant grow to be infertile female ants, the so-called worker ants. Their tasks are extensive, including the care of the queen, larvae and pupae; the cleaning, extension and repair of the nest; food procurement; and defense against enemies. They execute those tasks with remarkable efficiency in perfect order, without unnecessary behavior. Surprisingly, they have no leaders in each work team, but come to mutual understanding via various chemical communicators called differentiation pheromones and action-inducing pheromones. By using those pheromones, they recognize what they must do and work by focusing on their particular jobs. Those behaviors show the ultimate on-site activities.

Unfortunately, we do not have such an advantage as pheromones. However, we do have different intelligence from that of ants. To increase the efficiency of research and development, each individual worker on-site needs to be more aware of the existing issues and to act intelligently and vigorously by making the most of their wisdom. Or can you think of another way?

FUJIFILM RESEARCH & DEVELOPMENT

No. 58

CONTENTS

Originals

* Co-researcher outside FUJIFILM Corporation

Development of a New Generation Endoscope System with Lasers "LASEREO"

Yoshinori MORIMOTO*, Masahiro KUBO*, Masayuki KURAMOTO*,
Hiroshi YAMAGUCHI**, and Toshihiko KAKU**

Abstract

We have developed a new generation endoscope system "LASEREO". A new laser illumination technology is applied to LASEREO. Having two kinds of lasers and phosphor, the new illumination is useful in detecting the structure of the mucous membrane. We realized the narrow band light observation BLI (Blue LASER Imaging) that can emphasize a minute change of the mucous membrane structure by using the new illumination technology together with our original image processing technology.

1. Introduction

Conventionally, our endoscope systems employed Flexible spectral Imaging Color Enhancement (FICE) that allows easy observation of tissue characteristics and blood vessels by using signal processing to extract the spectral images of specific wavelengths from the white light generally used in such systems. However, it was regarded as difficult to produce high contrast images of microvessels on the surface of mucous membranes with white light illumination.

To address that issue, the new-generation endoscope system "LASEREO" (Fig. 1) released in September 2012 features a new laser illumination technology that combines two kinds of laser light with a phosphor and our original image processing technology. The system achieved the narrowband light observation function, Blue LASER Imaging (BLI), which enables image-enhanced endoscopy to detect the minute changes on the mucosal surface as key information for cancer diagnosis.

Fig. 1 LASEREO system.

This paper explains the outline, features, principles and capabilities of this new system and foresees the future possibilities of laser endoscopes.

2. Characteristics of the market

Gastroenterological endoscopy is available at the following three types of hospitals: a) core hospitals; b) general hospitals; and c) clinics. Core hospitals are further classified into two groups: Special Functioning Hospitals that provide highly advanced medical care; and Regional Medical Care Support Hospitals that back up general hospitals and clinics in local communities. In those hospitals, there is a strong need for magnifying endoscopy and image-enhanced endoscopy for definitive diagnosis before starting endoscopic therapies such as endoscopic mucosal resection (EMR) and endoscopic submucosal dissection (ESD). In cancer diagnosis, in particular, treatment plans are often determined by closely observing the patterns of microstructures and microvessels on the mucosal surface and examining the condition of lesions with endoscopy. The diagnosis is made according to the classification of those patterns, which exist in several forms for each region such as a pharynx, esophagus, stomach and large intestine, because tissue structures and cancer onset morphology vary depending on the region. In the meantime, in clinics, screening is the main diagnostic method and magnifying endoscopy is hardly ever conducted. However, there is a need for image-enhanced endoscopy for screening.

Original paper (Received December 20, 2012)

* Medical System Research & Development Center
Research & Development Management Headquarters
FUJIFILM Corporation
Miyanodai, Kaisei-machi, Ashigarakami-gun, Kanagawa
258-8538, Japan

** Imaging Technology Center
Research & Development Management Headquarters
FUJIFILM Corporation
Miyanodai, Kaisei-machi, Ashigarakami-gun, Kanagawa
258-8538, Japan

Image-enhanced endoscopy is classified into a) the optical method; b) the digital method; c) the optical digital method; and d) the dye spraying method. For the observation of the above-described superficial structures and microvessels, and also for the screening, the following methods are used: FICE (a digital method); NarrowBand Imaging (NBI) (an optical digital method); and indigo carmine dye spraying or Lugol's iodine solution spraying (a dye spraying method). In FICE, displayed images are enhanced with the organisms' reflection spectral information collected by processing signals obtained during the irradiation of white light. In NBI, the illumination used to collect spectral information is narrowband light obtained by passing white light through optical filters. Compared with the dye spraying methods that require preparation and take not only labor but also running costs before and after the use, there are high expectations for FICE and NBI because they need only button pressing to give a result.

3. Outline and features of the system

LASEREO is the first gastroenterological endoscope system to employ lasers for its illumination. It incorporates not only a function for white light observation but also a function for narrowband light observation that utilizes the characteristics of laser light as standards. In addition, compared with conventional light sources using xenon lamps, its power consumption and heat emission are particularly low. The system configuration is as follows: the "PROCESSOR VP-4450HD"; the laser "LIGHT SOURCE LL-4450" and the special L590 series endoscopes (EG-L590ZW for upper GI magnification endoscope, EG-L590WR for general upper GI endoscope, EC-L590ZW for lower GI magnification endoscope and EC-L590WM for general lower GI endoscope).

3.1 Features of the laser light source LL-4450

The laser light source LL-4450 uses two lasers with different wavelengths. It creates illumination suitable for either normal (white light) observation or narrowband light observation by changing the intensity ratio of those two lasers.

One is the white light mode laser (peak wavelength: 450 nm ±10 nm), which excites phosphors to create white light illumination with broader spectral distribution suitable for normal observation. The other is the short-wavelength narrowband light laser (i.e., BLI laser, peak wavelength: 410 nm ±10 nm), which is used to obtain information about the microvessels and slight uneveness on the mucosal surface as well as the deep blood vessels as high-contrast signals by utilizing its characteristics: short-wavelength and narrow spectral width (Fig. 2).

Other characteristics of this light source is the wide dynamic range of light control required from illumination. When applying narrowband light observation BLI, it is necessary to control the outputs so that the intensity ratio of the white light mode laser and the BLI laser is always constant over a wide range of light control. With the LL-4450, high-accuracy light control over the range is possible by combining multiple laser modulation drive methods.

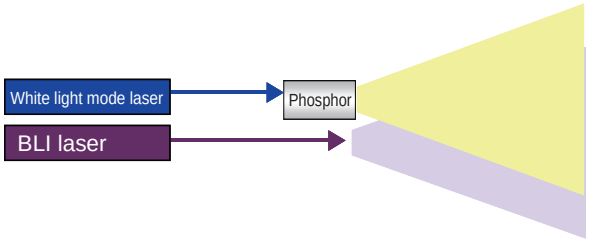

Fig. 2 Laser illumination.

3.2 Three kinds of illumination and four observational modes

LASEREO has four observational modes and employs three kinds of illumination with different spectral distributions (Fig. 3, Table 1).

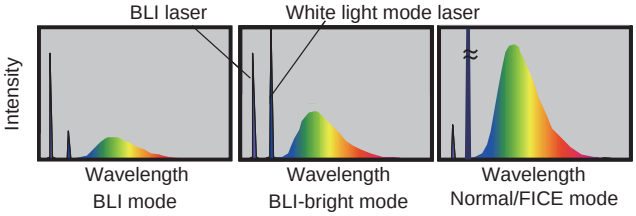

Fig. 3 Spectral distribution of illumination.

Table 1 Types of illumination and observation modes.

Mode	Purpose	Laser intensity		Description
		For white light observation	For BLI	
Normal	White light observation	Strong	Weak	Same color tone as conventional systems (xenon light source)
FICE	Color enhancement	Same as Normal mode		With spectral imaging, finer color changes are enhanced. By increasing the contrast of the colors of mucous membranes and blood vessels, the visibility of the blood vessels is enhanced. The brightness level is the same as normal images.
BLI	Observation of blood vessels and superficial mucosal structures	Weak	Strong	Images suitable for the enhancement of the superficial microvessels are generated by increasing the short-wavelength light components from lasers and improving the contrast originating from the presence of hemoglobin.
BLI-bright	Observation of blood vessels and superficial mucosal structures	Medium	Strong	Bright images are generated even when viewing relatively distant targets by slightly increasing white light components compared with BLI mode. The contrast between blood vessels and superficial structures is higher than in Normal or FICE modes but a little weaker than in BLI mode.

The conventional FICE function can be used for white light observation. The newly developed narrowband light observation BLI's illumination is the well-balanced mixture of short-wavelength narrowband light and white light. Figure 4 is the images which improved the contrast of a mucous membrane and the blood vessel by performing image processing for the signal of white light which has a wide wavelength range and the signal of short-wavelength narrowband light which has a narrow wavelength range.

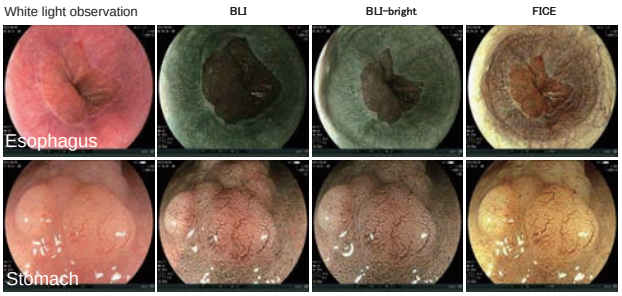

Fig. 4 Clinical images captured by LASEREO.
(supplied by Kyoto Prefectural University of Medicine Hospital)

BLI produces higher-contrast images of superficial mucosal structures and microvessels by increasing the intensity ratio of the BLI laser and white light mode laser. On the other hand, BLI-bright can create brighter images than BLI, even when viewing relatively distant targets, by slightly decreasing its ratio.

3.3 Difference between BLI and FICE

FICE generates several narrowband images by signal processing from a white light image, and reproduces RGB images from those narrowband images, then enhances them. In that way, it improves the contrast of mucous membranes and blood vessels (Fig. 5). On the other hand, BLI makes the same contrast improvement to irradiate strong short-wavelength narrowband light and enhance a image (Fig. 6).

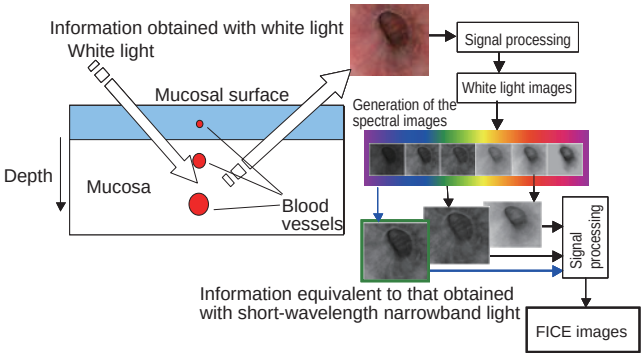

Fig. 5 Processing flow of FICE.

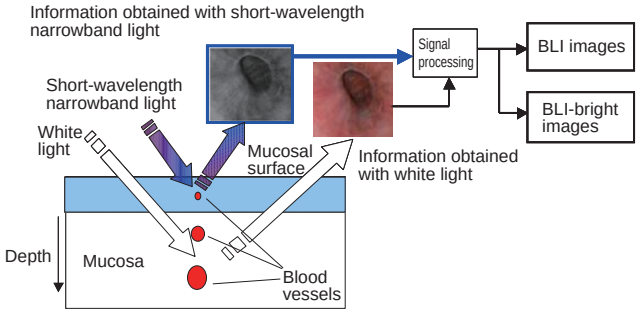

Fig. 6 Processing flow of BLI.

FICE, BLI and BLI-bright allow narrowband light observation. However, their image brightness and contrast intensity between mucous membranes and blood vessels are different as follows.

Brightness:
Darker ⟷ Brighter
BLI < BLI-bright < FICE ≅ White light observation
Contrast:
Higher ⟷ Lower
BLI > BLI-bright > FICE > White light observation

4. Development of BLI

4.1 Principle of BLI

BLI is an image-enhanced technology that distinguishes microvessels on the mucosal surface and deep blood vessels based on the light-absorption characteristics of hemoglobin (Fig. 7) and the scattering characteristics of mucous membranes.

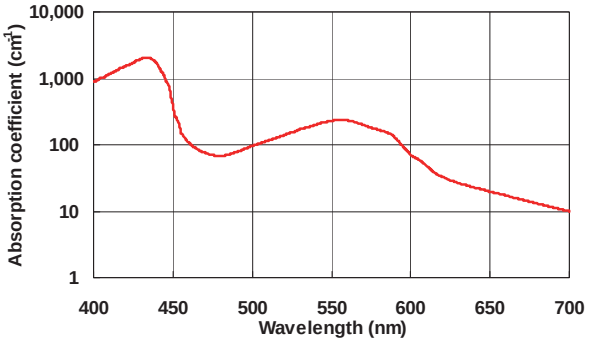

Fig. 7 Absorption spectrum of hemoglobin.

Figure 8 illustrates the basic principle of BLI. Short-wavelength light does not penetrate into deep layer of mucous membranes and can detect the superficial microvessels with high contrast (Fig. 8a). Conversely, long-wavelength light penetrates into deep layer of mucous membranes. Therefore, the light propagation process to deep layer makes the image of sperficial microvessels blurred and low-contrast by scattering, while the deep blood vessels are processed into a high-contrast image (Fig. 8b).

By using those two images, the superficial microvessels and deep blood vessels can be showed in different colors.

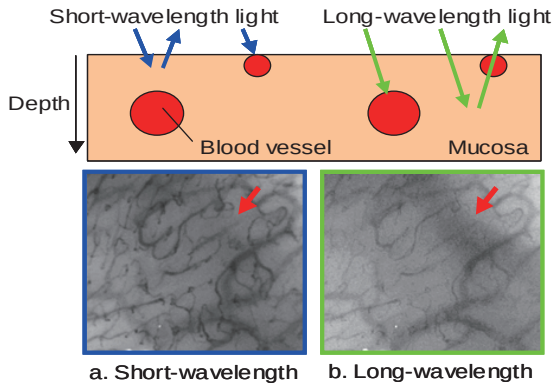

Fig. 8 Principle of BLI.

4.2 Conditions of the light source

In endoscopy the clear identification of superficial microvessels is required. It was known that illumination using short-wavelength narrowband light filters could improve the contrast of microvessels. However, this is limited to qualitative interpretation of the relationship between the contrast of microvessel and the wavelength.

In this paper, we firstly confirmed whether high-contrast superficial microvessel images can be obtained with short-wavelength narrowband laser light by conducting simulation. Then, we determined the specifications of the BLI light sources by experiments measuring oral mucosa.

4.2.1 Assessment using simulation

With the spectral distribution of illumination and mucosal model, image signal values can be calculated from the following equation.

$$S(c, m) = \int L(\lambda)\, M(m, \lambda)\, C(c, \lambda)\, d\lambda \quad \cdots (1)$$

$S(c, m)$: Image signal value
$L(\lambda)$: Spectral distribution of illumination
$M(m, \lambda)$: Mucosal spectral reflectance
$C(c, \lambda)$: CCD spectral sensitivity
c: R, G, B
m: Mucosa, superficial microvessels, deep blood vessels

The spectra used for $L(\lambda)$, the spectral distribution of illumination, were those of several short-wavelength lasers and also the white light mode laser in conjunction with its phosphor material.

The unknown mucosal spectral reflectance, $M(m, \lambda)$, was calculated with the data of the gastric mucosa and blood by the simulation of light propagation. Figure 9 exemplifies the reflection spectra of the mucosa and superficial microvessels thus calculated by the simulation of light propagation.

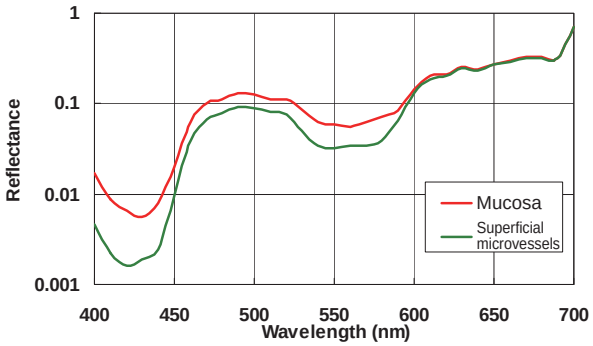

Fig. 9 Reflection spectra obtained by simulation.

The contrasts of the blood vessels by simulation with illumination of several intensity ratios of short-wavelength lasers and a white light mode laser, illumination of a xeon lamp and illumination of a xeon lamp with a narrowband light filter were compared (Fig. 10).

As a result, the following findings were obtained: the selection of lasers with appropriate wavelengths enables to realize high-contrast images; increasing the intensity of short-wavelength lasers against white light mode laser creates a high-contrast effect. In conclusion, a BLI laser with a wavelength of 410 nm was found to be suitable for observing superficial microvessels.

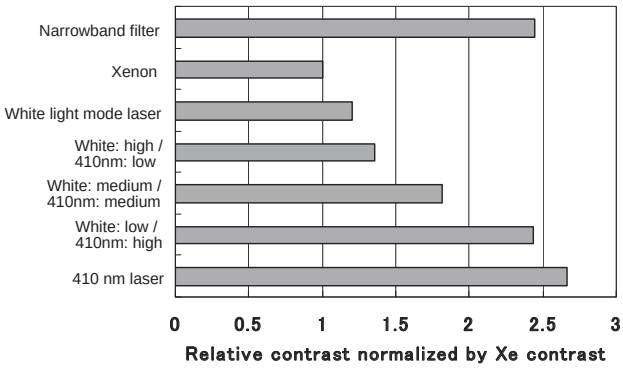

Fig. 10 Contrasts in microvessel images obtained by simulation.

4.2.2 Experiment with the oral mucosa

Based on the results obtained by simulation, the conditions under which high-contrast blood vessel images can be created were verified with the oral mucosa while changing the intensity ratio of the BLI laser and white light mode laser.

The contrast between the oral mucosa and superficial microvessels (ratio of the signal values of the mucosa and the superficial microvessels) under each light source condition is shown in Fig. 11 and the respective images in Fig. 12.

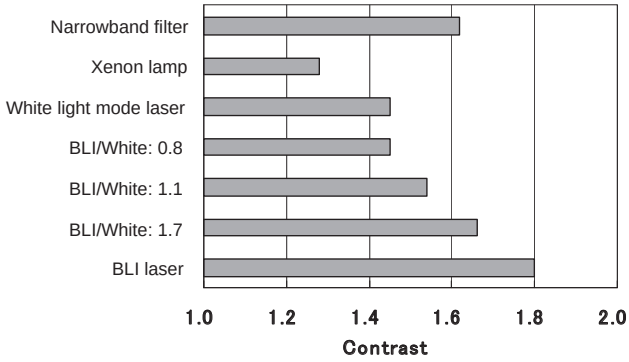

Fig. 11 Contrasts in microvessel images obtained in an experiment.

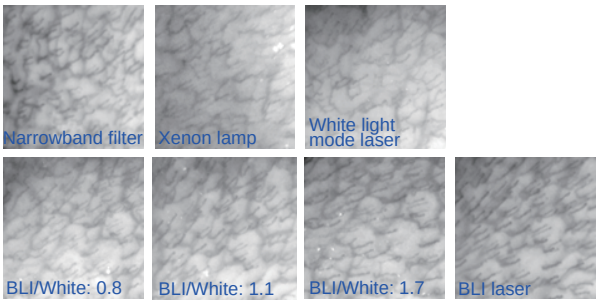

Fig. 12 Experimental results using oral mucosa.

Figure 11 shows that the setting of a proper light intensity ratio of the BLI laser and white light mode laser can create high-contrast microvessel images and there are equivalent to microvessel images with narrowband light filter whose center wavelength is 420 nm.

Figure 12 confirms that various levels of microvessel contrasts can be obtained by changing the intensity ratio of those two lasers. It indicates the possibility for the realization of illumination suitable for each purpose and observation target.

The microvessel contrasts to the oral mucosa obtained by experiment correspond respectively to the light source conditions for blood vessel contrasts obtained by simulation. Thus, the validity of the selection of light source conditions by simulation was proved.

4.2.3 Setting of two narrowband light observational modes

Taking into consideration the individual strengths of the BLI laser and white light mode laser, we have set up the following two narrowband light observational modes in LASEREO.

•BLI mode:

In this mode, the ratio of the BLI laser is increased to enhance the contrast of the microvessels on the mucosal surface. The main intended usage is the observation of targets at a short distance and magnifying endoscopy.

•BLI-bright mode:

In this mode, the BLI laser and white light mode laser are included in illumination in due ratio to improve the contrast of blood vessels while brightness is maintained. The main intended usage is the observation of targets at a middle to short distance.

These two modes achieved bright, non-magnifying endoscopy as well as high-contrast blood vessel magnifying endoscopy in LASEREO's narrowband light observation.

4.3 Structure enhancement

The targets of endoscopy are diverse, such as lesions with a diameter of a few centimeters from a relatively distant viewpoint and microvessels with a diameter of about 10 μm in a magnified view as shown in Fig. 13 (Observation distance of 2 mm). Moreover, in magnifying endoscopy, not only 10-μm microvessels but also a target like the marginal crypt epithelium bordered white in Fig. 13 (Observation distance of 5 mm) can be observed to determine future treatment plans. To cover an extensive range of observational conditions, two enhancement modes with different frequency bandwidths are incorporated in the BLI. A-mode, which is suitable for the enhancement of low-frequency regions, is suitable for the enhancement of areas and structures. B-mode is designed to enhance only thin lines. This is suitable for observing microvessels.

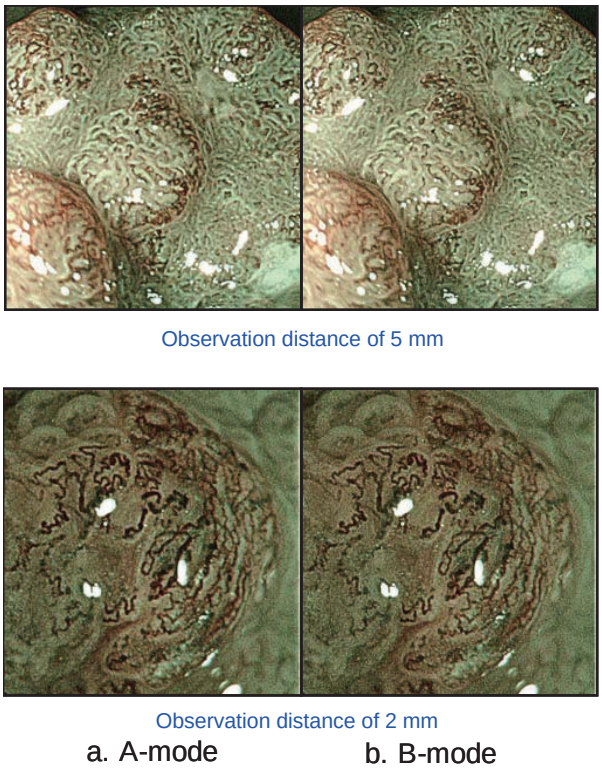

Fig. 13 Two modes of structure enhancement.

4.4 Color enhancement

The mucosal epithelium and the blood vessel density of the gastrointestinal tract vary depending on the region. Therefore, the reproduced color tones can be diverse. In BLI, color enhancement modes (i.e., C1, C2 and C3) are provided to make lesions stand out in each region of a pharynx, esophagus, stomach and large intestine. In BLI-bright, the "No color enhancement" tone, which is similar in color to the one in white light observation, is provided additionally (Fig. 14).

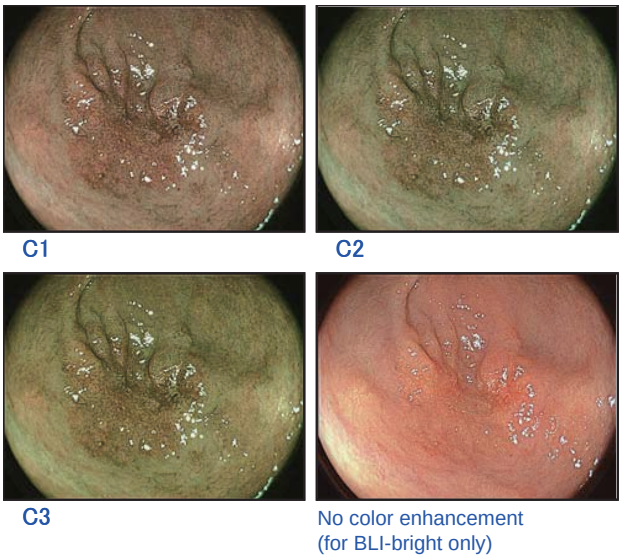

Fig. 14 Color enhancement by BLI and BLI-bright.

5. Conclusion

The gastroenterological endoscope system LASEREO employs a laser light source for its illumination. By utilizing the characteristics of the high brightness and narrow bandwidth particular to laser light sources, we have succeeded in the incorporation of the narrowband light observation BLI function into the system, which enables the display of the mucosa and blood vessels with high contrast. In addition, we have realized BLI-bright in which bright narrowband light observation at a relatively distant viewpoint is possible by changing the intensity of the BLI laser and white light mode laser.

To establish endoscopy systems useful for the detection of early cancerous lesions and the determination of treatment strategies, it is necessary to develop technologies that can visualize a great variety of biological and functional changes in cancer.

LASEREO has the potential for the development of new diagnostic technologies that enable the visualization of *biological and functional changes in cancer* by using laser light sources with different light wavelengths.

We have already engaged, in cooperation with National Cancer Center Hospital East, in the development of a technology with a laser light source that visualizes a type of biological and functional change in cancer: the hypoxia of cancerous lesions. In the future, we will keep striving to further develop LASEREO as an endoscopy system that promotes the early discovery of cancerous lesions and the determination of treatment strategies.

6. Acknowledgement

We express our special thanks to Satoshi Ozawa who had been involved in the concept making of the system from the beginning of its development and Jun Matsunaga, Masayuki Takahira and Azuchi Endo who played central roles respectively in developing the scope, processor and light source of LASEREO.

Development of “FUJIFILM DR D-EVO plus C24i/s”

Kouichi KITANO*, Keita WATANABE*, and Akihito BETTOUYASHIKI*

Abstract

We have newly developed the small and light CsI DR cassette, “FDR D-EVO plus C24i/s”, which features better image quality with low dose exposure, improved durability and prolonged battery life. The details of the FDR D-EVO plus C24i/s are described in this paper.

1. Introduction

In recent years, the introduction of cassette-type digital radiography (DR) systems has been more and more promoted. In particular, in the domains of orthopedics and otolaryngology where various physical positioning is required in capturing images, DR systems using a smaller cassette instead of the conventional 14-inch × 17-inch cassette models are useful. Moreover, there is a need for cassettes being compatible with the trays dedicated to small-size incubators. In those cases, a streamlined workflow can be realized by using a small-cassette DR system (Fig. 1).

To meet these circumstances, we developed a small, 24-cm × 30-cm cesium iodide (CsI) DR cassette. In this paper, we introduce the new cassette named “FDR D-EVO plus C24i/s”. Its small size offers increased flexibility in use, which is suited to the diverse positioning requirements for imaging in the field of orthopedics. In addition, as it can be mounted onto the trays dedicated to incubators without alteration, it can be introduced as an imaging solution for diagnosis for newborn babies.

2. Features

The FDR D-EVO plus C24i/s, which is a small and light DR cassette, has achieved a higher resolution and a lower level of X-ray exposure by enhancing the DR functions and capabilities of the conventional D-EVO series DR cassettes that employ Fujifilm’s original technology, Irradiation Side Sampling (ISS) system. The following are the features of the FDR D-EVO plus C24i/s (Fig. 2).

Fig. 1 The 24cm × 30cm DR cassette: FDR D-EVO plus C24 i/s, well suited for small patients and anatomy.

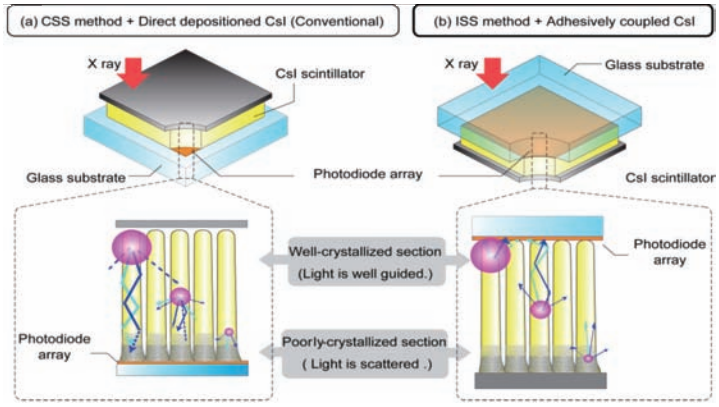

Fig. 2 Unlike Conventional Side Sampling (CSS) methods (a), FUJIFILM Irradiated Side Sampling (b) avoids the poorly-crystallized section of the CsI scintillator.

Original paper (Received December 3, 2012)

* Medical System Research & Development Center
Research & Development Management Headquarters
FUJIFILM Corporation
Miyanodai, Kaisei-machi, Ashigarakami-gun, Kanagawa
258-8538, Japan

2.1 Reduction of the exposure dose

Images are obtained by reading out X-ray signals with which the CsI scintillator is irradiated using an analog electrical circuit and outputting the data via analog/digital conversion. The FDR D-EVO plus C24i/s employs a newly developed high-sensitivity, low-noise analog electrical circuit and achieves high-performance digital image processing. By using those technologies in combination with our original ISS system (Fig. 2), we succeeded in obtaining high DQE with reduced X-rays and in lessening the graininess of images as a consequence of the low-level noise. RQA5-standard DQE (for FDR D-EVO plus C24i/s and FDR D-EVO plus C35i/s) with each exposure dose and MTF are shown respectively in Fig. 3 and Fig. 4.

2.2 Improvement of robustness

We have developed four models of DR cassettes. Based on expertise accumulated via those activities, we newly developed a solid simulation technology and created a high-strength DR cassette by effectively deploying reinforcements inside. It sustains a 310-kg load against the full imaging surface (double that of our other products) and a 160-kg load on any ϕ 40-mm spot of the imaging surface (1.5 times the load of our other products) in spite of its light weight of 1.9 kg including the battery. The spot load dispersion design model is shown in Fig. 5. This robustness has enabled the provision of safe and comfortable imaging environments to radiologists in any situation including in the field of orthopedics where the weight of patients is applied to the equipment.

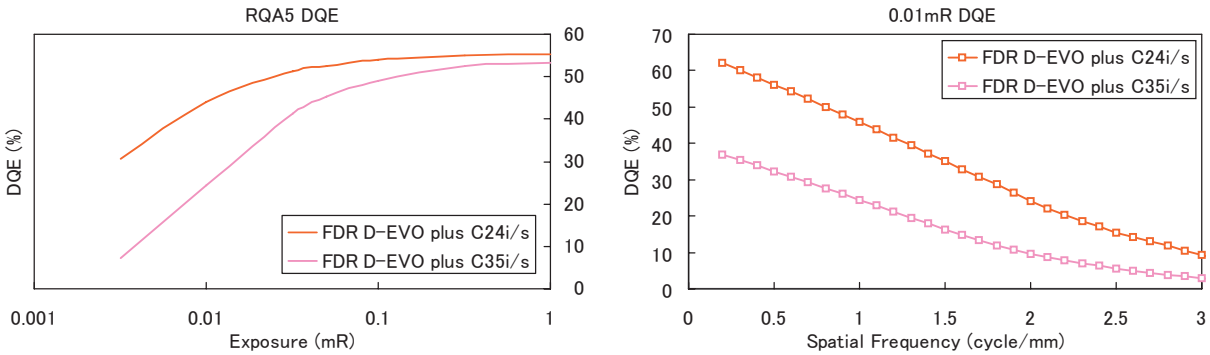

Fig. 3 Comparison of Detective Quantum Efficiency (DQE) between FDR D-EVO plus C24 i/s and FDR D-EVO plus C35i/s.

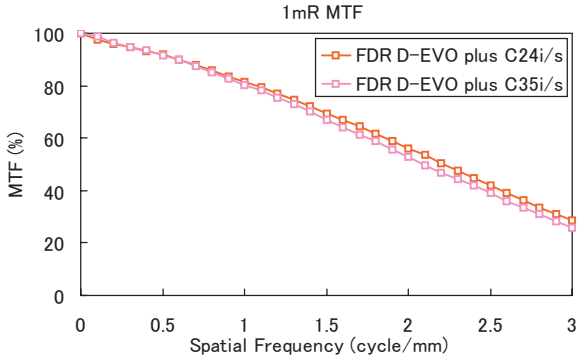

Fig. 4 Comparison of Modular Transfer Function (MTF) between FDR D-EVO plus C24i/s and FDR D-EVO plus C35i/s.

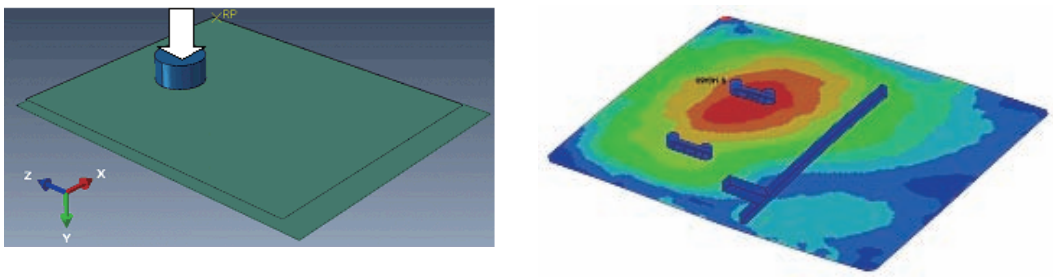

Fig. 5 Spot load dispersion design of FDR D-EVO plus C24i/s.

2.3 Long-duration operation with a battery

Following a complete review of the electrical drive and control circuits inside the flat panel sensor and thorough reduction in the size (space) and the power consumption, long operation for about 7.5 hours per battery charge (double that of our other products) has been realized. In addition, continuous imaging of 800 captures is possible. Fig. 6 shows the power consumption reduction effect of the FDR D-EVO plus C24i/s and FDR D-EVO plus C35i/s while they are waiting or reading out images, standardized by letting the maximum power consumption be 1. This effect helps improve the imaging workflow and usability inside hospitals considerably.

Moreover, the FDR D-EVO plus C24i/s has been made compatible with conventional systems by using the same battery as that used in the other FDR D-EVO series cassettes.

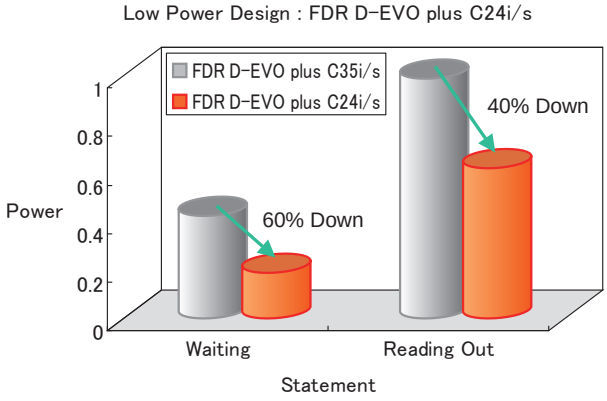

Fig. 6 Power Consumption comparison between FDR D-EVO plus C24i/s and FDR D-EVO plus C35i/s.

2.4 Features of the D-EVO series that have been retained

The FDR D-EVO plus C24i/s can be used in parallel with the other D-EVO series DR cassettes. Speedy image display (Fig. 7) and auto trimming of irradiation fields, which are the features of the D-EVO series DR cassettes, are retained by the FDR D-EVO plus C24i/s, realizing a streamlined imaging workflow. Also, it has incorporated the SmartSwitch function (X-ray Auto Detection Mode, Fig. 8). This enables more flexible imaging, utilizing the advantage of its small size.

3. Conclusion

The FDR D-EVO plus C24i/s has enabled high-flexibility imaging while reducing the required exposure dose. With this, the potential of DR cassettes in various domains, such as orthopedics and otolaryngology, can be increased.

(“FUJIFILM”, “FDR D-EVO” and “SmartSwitch” referred to in this paper are registered trademarks of FUJIFILM Corporation.)

Fig. 7 FDR D-EVO plus C24i/s exposure cycle time.

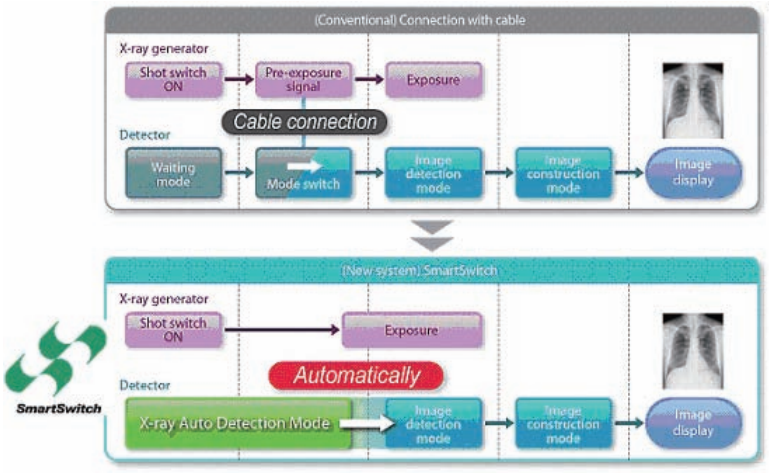

Fig. 8 FUJIFILM SmartSwitch technology enables X-ray auto detection, eliminating the need for electrical interfacing with the X-ray generator.

Development of Functional Cosmetics Brand “Lunamer”

Taichi MURAGUCHI*, Tomomi TATEISHI*, Ikuko OOGARU*, Karin KUROIWA***, Takeharu TANI***, Naoko YOSHIDA**, Hideyasu ISHIBASHI**, and Takuji KOSUGI*

Abstract

Skin dullness is one of the major problems for women of a certain age. Although some hypotheses for the causes were postulated, for examples the structure of the skin surface or pigmentation of proteins, they have not been proven completely. As a result of our optical analyses including measurement using polarized images and OCT, it turned out that a key for a clear skin is a healthy epidermal layer which does not affect light. Thus, we have developed an active vitamin E (tocotrienol) emulsion, named Clear-nano Vitamin E, which is effective to prevent damage on the epidermal layer caused by environmental factors. We have created the “Lunamer” series containing Clear-nano Vitamin E and the other selected active ingredients based on Fujifilm’s original “Clear & Charge” concept in an effective formula, for the purpose of improving the healthiness of the epidermal layer.

1. Introduction

Fujifilm has engaged in the development of functional cosmetics, applying its technology for reproducing clear images on films to the field of creating clear skin. In July 2012, as a new functional cosmetics brand, it launched the “Lunamer” range onto the market.

First, targeting the skin dullness that women start to feel in their 20s or 30s, we clarified its mechanism by conducting optical analyses. Then, based on our original Clear & Charge concept, which is the best approach to solve that problem, we have produced the Lunamer range containing five selected ingredients, including Clear-nano Vitamin E, that take care of sensitive skin gently but thoroughly, aiming to realize clear and brilliant skin from inside to outside (Fig. 1).

Fig. 1 New cosmetic brand “Lunamer”.

2. Factors that cause skin dullness

It is advocated that the following four factors are the main causes of skin dullness (Fig. 2).

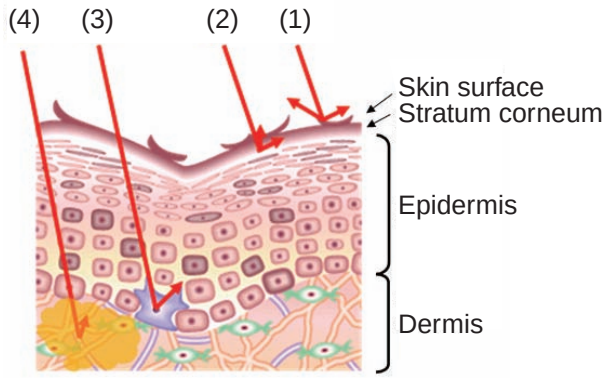

Fig. 2 Presumed causes of dull skin.

(1) Bumps on the skin surface
(2) Disordered stratum corneum
(3) Epidermal pigmentation (melanin)
(4) Dermal pigmentation (saccharification, carbonylation)

However, the detailed mechanism was not yet understood. Then, we tackled this issue and discovered the following by applying optical analysis methods that we have developed in the field of photographic technology.

Original paper (Received December 4, 2012)
* Pharmaceutical & Healthcare Research Laboratories
Research & Development Management Headquarters
FUJIFILM Corporation
Ushijima, Kaisei-machi, Ashigarakami-gun, Kanagawa 258-8577, Japan
** Imaging Technology Center
Research & Development Management Headquarters
FUJIFILM Corporation
Miyanodai, Kaisei-machi, Ashigarakami-gun, Kanagawa 258-8538, Japan
*** Frontier Core-Technology Laboratories
Research & Development Management Headquarters
FUJIFILM Corporation
Ushijima, Kaisei-machi, Ashigarakami-gun, Kanagawa 258-8577, Japan

3. Findings from our original optical analysis technology

3.1 Analysis of skin dullness by image measurement

Light that falls on the skin surface is reflected and scattered. Some goes inside the skin, where it is scattered and absorbed. The light not absorbed returns to the skin surface. Normally, we see that returned light (Fig. 3).

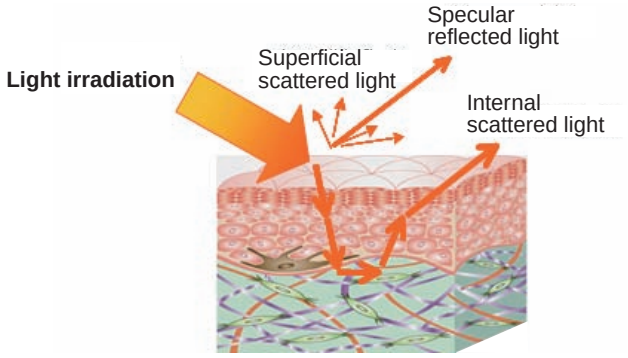

Fig. 3 Light reflection of human skin.

As described above, it is supposed that multiple causes are involved in skin dullness but the detailed mechanism is yet to be explained. We built a new hypothesis that it may be caused by the disordered propagation of light inside the skin, more specifically, in the epidermis. To verify this hypothesis, we conducted a visualization of the light conditions on the surface of or inside the skin with polarized image measurement technology that allows separation measurement of light.

Polarized image measurement technology utilizes the polarization property of light (difference in the vibration direction). Light that returns to the surface after being scattered inside the skin will be reflected irregularly because of the material properties and unevenness inside the skin. Therefore, such light is different from the one reflected on the skin surface in its polarization property. By measuring and imaging this change of polarization property, light that takes those two different paths can be separated.

We conducted the polarized image measurement with test volunteers aged from their 20s to 50s, with dull skin and clear skin. Light that returned to the skin surface after being scattered inside was measured and image processing, such as tone adjustment, was applied; then the light quantity distribution was analyzed (Fig. 4).

The image comparison of dull skin with clear skin revealed that, in the former, the quantity of light that returned from inside the skin was small overall and its distribution was uneven.

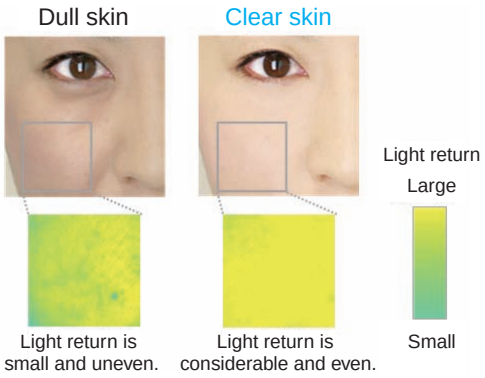

Fig. 4 Result of dull skin analysis using polarized images.

3.2 Tomographic analysis of the skin layer by OCT

By applying optical coherence tomography (OCT) as used for medical imaging diagnosis, we then visualized from what depth the light that went into the skin returned to the surface[1]. Irradiating the cheek with near infrared (1.3 μm) laser beams, we measured the time taken until light returned and assessed from what location more light returned. Fig. 5 shows the results of the comparison between dull skin and clear skin. Locations marked in blue in the figure return light. As shown, in dull skin, the overall light return was small. In contrast, in clear skin, much more light returned through the epidermis from the deep skin (dermis).

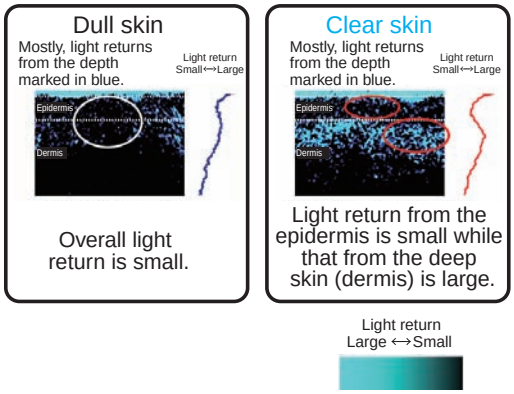

Fig. 5 OCT (Optical Coherence Tomography) images of dull skin and clear skin.

3.3 Simulation of light propagation

Furthermore, we analyzed, via simulation, light propagation inside the skin to elucidate the difference between dull and clear skin. Light scattering and absorption inside the skin are caused by the cellular-level microstructure. Therefore, to precisely reproduce light propagation in the microstructure, we employed an electromagnetic wave analysis technique, the finite-difference time-domain method (FDTD); then, measured and visualized the time elapsed

from light entering to leaving the skin via scattering (Fig. 6). In dull skin, light was scattered on the epidermis and attenuated rapidly. In contrast, in clear skin, light passed through the epidermis and was scattered in the deep skin after reaching the dermis, from where more homogeneous light was reflected. This reveals that it is important to remove the cause of light scattering and absorption on the epidermis.

That is, clear skin allows homogeneous light to return from the inside of skin and, to establish this condition, it is essential to keep the epidermis healthy, free of the factors that disturb light.

4. Clear & Charge approach

To allow light to scatter evenly from the epidermis, it is necessary to eliminate not only the roughness of the skin surface but also the optical diffuseness inside the skin. To maintain internal skin health, a care method must be established that helps create healthy skin as well as increases skin resistance against everyday environmental stresses (such as UV-rays, cigarette smoke and exhaust gas). To meet that need, we developed the functional cosmetics Lunamer, which is based on our original *Clear & Charge* concept for gentle and thorough skin care to grow healthy skin (Fig. 7). It contains five ingredients in due proportion, that keeps epidermal cells healthy and enables light to return evenly from the deep skin.

4.1 What is active vitamin E (tocotrienol)?

There are two kinds in vitamin E: tocopherol (ordinary type) and tocotrienol (active type) whose structure is partly different from the former (Fig. 8).

Active vitamin E is a scarce substance. In the natural world, palm oil contains the highest proportion but the amount is merely 0.8 g per kg (800 ppm). This rarity has prevented the promotion of its research. Nevertheless, in basic research, it has been reported that active vitamin E has a greater neuroprotective effect and antioxidant capability inside cells than ordinary vitamin E[2)]. In our research, active vitamin E exhibited 70 times greater performance in the prevention of UVB-induced inflammatory substance generation than the oil-soluble vitamin C derivatives (VCIP) approved as a main whitening agent. The effect was also greater than ordinary vitamin E (Fig. 9). In addition, it was confirmed that active vitamin E had a concentration-dependent effect on the detoxification (deoxidization) of harmful substances such as active oxygen and radical organic matter.

4.2 Development of Clear-nano Vitamin E

Active vitamin E is very effective but it is nearly insoluble in water. This prevents effective application to the skin and blending into cosmetics without affecting their functionality and usability. In addition, its stability in formulation is low because of its high antioxidant property.

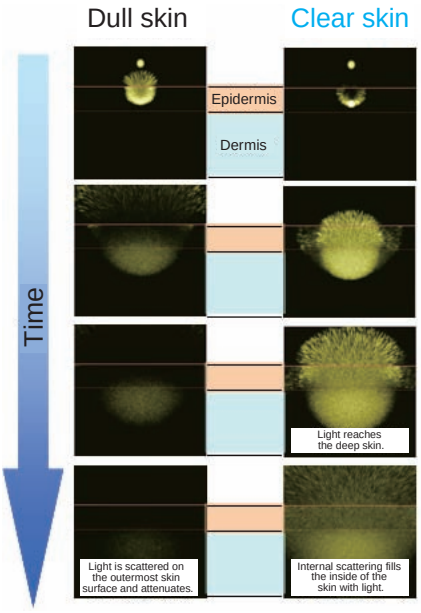

Fig. 6 Cross-sectional images of simulated light propagation in dull skin and clear skin.

Fig. 7 "Clear & Charge" concept.

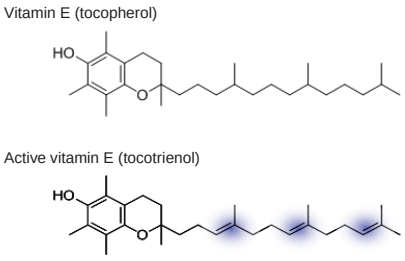

Fig. 8 Molecular structures of tocopherol (widely used) and tocotrienol.

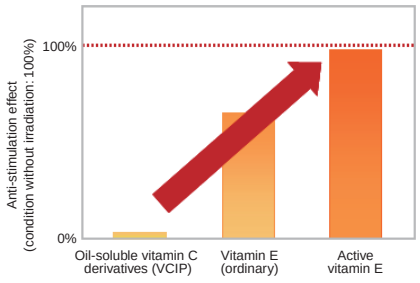

Fig. 9 Inhibition of UVB-induced inflammation by antioxidant properties.

To solve those problems, we created the world's smallest-class, water-soluble nano-particles (60 nm) by fully utilizing our original nano technology. Nanonization increases the surface area of those particles, which makes them unstable. To respond to this, we developed the new *nano-protect* design, which has improved the stability of active vitamin E greatly by the appropriate use of oils with different polarities. We thus succeeded in the development of Clear-nano Vitamin E expected to be useful in skin care (Fig. 10).

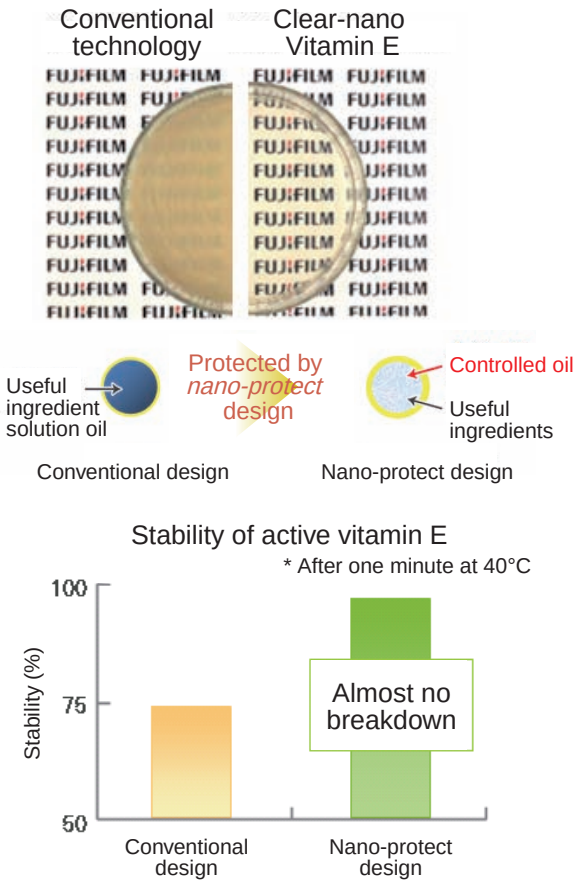

Fig. 10 Stability of Clear-nano Vitamin E.

To check the permeability of Clear-nano Vitamin E to the stratum corneum, we performed the following procedures: occluded application of Clear-nano Vitamin E to the inside of the upper arm and wash; collection of the skin tissue from the stratum corneum by tape stripping; quantity determination of the specimens; and comparison. As a result, its permeability was found to be up to eight times greater than that of non nano-particles.

4.3 Other useful ingredients

Other than Clear-nano Vitamin E, the Lunamer range includes two *Clear* ingredients and two *Charge* ingredients. One of the former-type ingredients is named Crown Sugar. It is a kind of oligosaccharide and catches harmful substances with its inclusion effect. The other is an extract of the Japanese medical herb, scutellaria baicalensis, which keeps the skin away from harmful substances and UV damage that accelerate early-stage aging[3), 4)]. As *Charge* ingredients, the Japanese medical herb, curcumin, increases the production of detoxification enzymes in the skin cells; and nano vitamin A, which is nanonized stable-type vitamin A oil, affects epidermal cells and promotes their reproduction.

Each item of the Lunamer range contains all those five ingredients, each designed for its particular properties.

5. Empirical verification of the effect on the skin

To confirm the effectiveness of the Lunamer range, a two-week continuous use experiment was conducted. Six test subjects in their 20s and 30s used the cleansing foam (every morning and night) and the wipe-off essence Lunamer Brightener (only at night) and their skin conditions before and after the experiment were compared.

Table 1 shows the increase of the brightness (L* value) of pores and over the cheek after the two weeks of use. For three out of the six, both L* values increased by at least 0.5 after the experiment and their skin conditions were improved.

Table 1 Increase in the brightness of pores and cheeks after two weeks continuous use.

Increase of the L* value	Less than 0.5	0.5 to 1.0	More than 1.0
L* value of pores	3	2	1
L* value over the cheek	3	2	1[*1]

In addition, before and after the continuous use experiment, the spectral reflectance curves for the cheek were measured with the Topcon SR-3 spectroradiometer. As an example, the curves for one test subject ([*1] of Table 1) are given in Fig. 11. The skin dullness reduced because of the decreased yellow reflected light around 580 nm and the skin tone was improved because of the increased red reflected light at 600 nm and over.

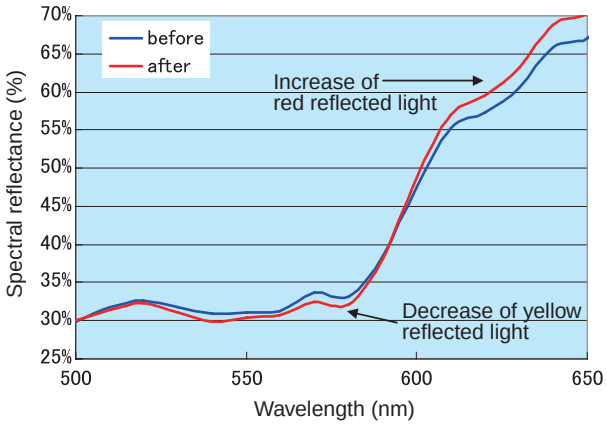

Fig. 11 Color change on cheeks after two weeks continuous use.

6. Conclusion

The new functional cosmetics brand, Lunamer, described in this paper was created from discoveries brought about by our original optical analysis technology to solve discovered problems with our unique nano technology. These functional cosmetics can be provided only by Fujifilm.

To solve skin problems, we will keep utilizing our analysis technology cultivated via experience in the photography industry. Through product development from new points of view and based on science, which is only possible by Fujifilm, we will strive to contribute to the further improvement of the quality of people's lives.

References

1) Schmitt, Joseph M. IEEE J. Sel. Top. Quantum Electron. **5** (4), 1205-1215 (1992).
2) Aggarwal, B.B.; Sundaram, C.; Prasad, S.; Kannappan, R. Biochem. Pharmacol. **80** (11), 1613-1631 (2010).
3) Morita, A.; Torii, K.; Maeda, A.; Yamaguchi, Y. J. Investig. Dermatol. Symp. Proc. **14** (1), 53-55 (2009).
4) Kai, Y.; Kishimoto, T.; Structural Chemistry of the Cyclodextrin Inclusion Complexes of Environmental Load Substances - X-ray Structural Studies on 1,4-dioxane-α-cyclodextrin Complex. Memoirs of Fukui University of Technology No. 45, 395-402 (2012)

Development of ASTALIFT Renewal Products

Eriko INUI*, Taichi MURAGUCHI*, Hiroyuki KITAOKA*, Mikinaga MORI*,
Toshihiko SAWADA**, Tadao SHIBAMOTO**, Atsushi ORIKASA***, and Kouzou NAGATA*

Abstract

The ASTALIFT series is a comprehensive anti-aging skincare brand, developed by applying Fujifilm's photo technology. After five years of success in the market, we renewed the ASTALIFT series having enhanced anti-aging capabilities realized by adding lycopene and an analog of resveratrol in appropriate form. We discovered novel benefits of lycopene, such as its ability to promote antioxidant production in human skin cells and boost astaxanthin's antioxidant capacity. We stabilized the lycopene in nano size, further enhancing the total antioxidant capacity. This nano lycopene is added to all products of this new series. Moreover, we also discovered that mesh collagen (type IV collagen) plays an important role in increasing the thickness of the epidermal layer; and thus, added high permeable resveratrol, which exerts a protective effect on mesh collagen, into one of the new series products, "ASTALIFT ESSENCE DESTINY".

1. Introduction

In September 2007, we released the "ASTALIFT" skincare range of cosmetics that impregnates skin with moisture to restore its freshness and resilience. It is the fruit of our experience in collagen research, anti-oxidization technology, nanotechnology, and photoreaction analysis/control technology cultivated in the photography domain. Containing a high antioxidant ingredient, astaxanthin, and a moisturizing ingredient, collagen, ASTALIFT has been promoted as an anti-aging functional cosmetic.

In September 2012, five years after its first launch onto the market, we updated the range by further enhancing its anti-aging functionality and released it as "Advanced cosmetics moving ahead". In the new range, nano-lycopene is included in all the items to increase their comprehensive antioxidant capacity. In addition, "ASTALIFT Essence Destiny" has joined the lineup as a feature item containing high-permeability resveratrol that we discovered while delving into our unique collagen research.

In this paper, we will report the details of the novel function of lycopene that we discovered in the research of anti-oxidization technology, nanotechnology, and the research of the usefulness of mesh collagen.

2. Advances in research on anti-oxidization

2.1 Research on lycopene's functionality

Lycopene is a kind of carotenoid and a red pigment present abundantly in tomatoes, watermelons and persimmons. It is known to have high antioxidant capacity among the antioxidant ingredients that eliminate active oxygen caused by UV-rays and environmental damage. In addition, it has been reported to have anticancer effects and to be able to relieve diabetes[1]. Focusing on these high capabilities of lycopene, we promoted research and discovered two new functions of lycopene: improving skin's self antioxidant capacity and improving astaxanthin's antioxidant capacity.

2.1.1 The effect of lycopene on improving skin's self antioxidant capacity

Human skin suffers oxidative damage by aging and being exposed to strong UV-rays, which is known to be the cause of wrinkles and blemishes. To protect skin from such oxidative damage, humans have a function to produce antioxidants *in vivo*. However, it has been reported that this function weakens with aging[2]. To combat this, we put Nrf2 protein that controls the production of various *in vivo* antioxidants on the target. Normally, Nrf2 protein exists in the cytoplasm but, when damaged by oxidation,

Original paper (Received December 4, 2012)
* Pharmaceutical & Healthcare Research Laboratories
Research & Development Management Headquarters
FUJIFILM Corporation
Ushijima, Kaisei-machi, Ashigarakami-gun, Kanagawa 258-8577, Japan
** Analysis Technology Center
Research & Development Management Headquarters
FUJIFILM Corporation
Nakanuma, Minamiashigara, Kanagawa 250-0193, Japan
*** Product Marketing Group
Life Science Products Division
FUJIFILM Corporation
Akasaka, Minato-ku, Tokyo 107-0052, Japan

it moves to the nucleus and induces the expression of a group of antioxidant genes. Thus, the production of various antioxidants is promoted there (Fig. 1-a).

We newly discovered that lycopene increases Nrf2 protein inside the nucleus of a human skin cell and induces the expression of the glutathione synthetase (GSS) gene as an *in vivo* antioxidant; and that it increases intracellular glutathione abundance (Figs. 1-b1, 1-b2 and 1-b3). It was also confirmed that the increase of intracellular glutathione abundance by lycopene inhibits cell injury by oxidative damage (Fig. 1-b4).

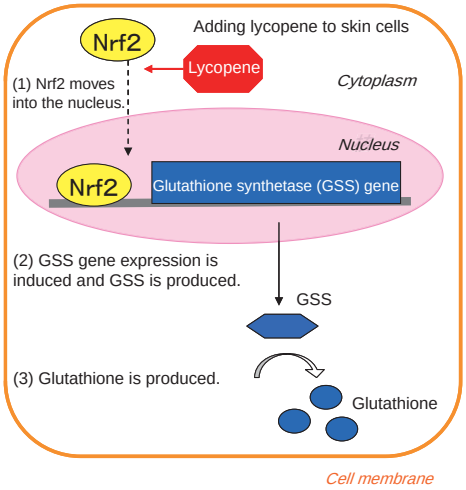

Fig. 1-a Glutathione synthesis mechanism.

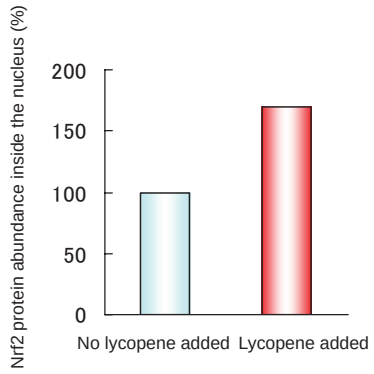

Fig. 1-b1 Effect of lycopene on Nrf2 protein in nucleus.

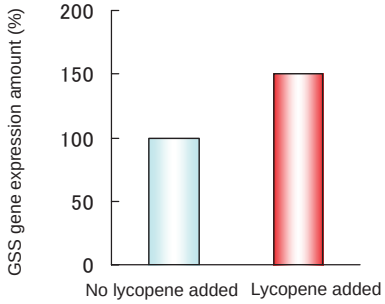

Fig. 1-b2 Effect of lycopene on gene expression of glutathione synthesis enzymes.

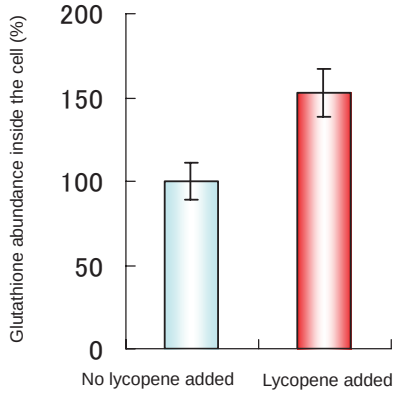

Fig. 1-b3 Effect of lycopene on intracellular glutathione production.

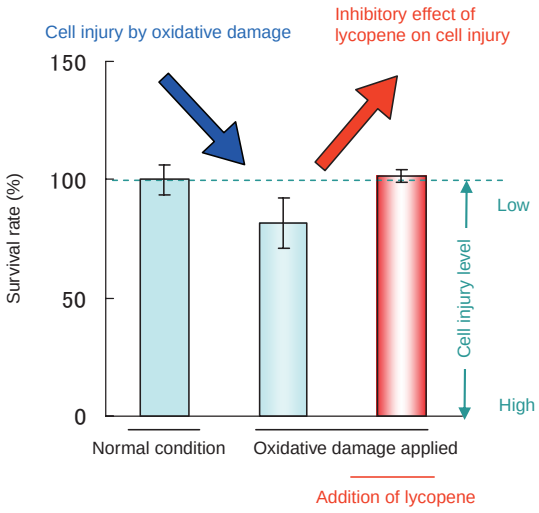

Fig. 1-b4 Effect of lycopene on inhibiting cell injury.

2.1.2 The effect of lycopene on improving astaxanthin's antioxidant capacity

Like lycopene, astaxanthin is known for its high antioxidant capacity. The addition of lycopene resulted in astaxanthin's antioxidant effects lasting to about three times their previous value (Fig. 2).

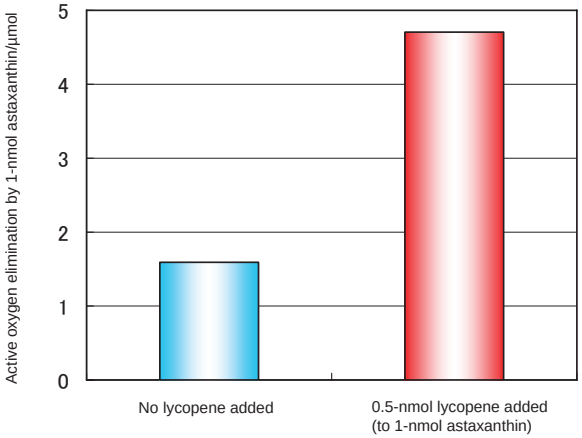

Fig. 2 Synergistic effect of astaxanthin and lycopene.

2.1.3 Mechanism of improving antioxidant capacity

One of the possible reasons for astaxanthin's antioxidant effects lasting longer with lycopene was the intermolecular one-electron transfer hypothesis. It was thought that lycopene provides its own π-electron to astaxanthin oxidants generated by astaxanthin's antioxidant reaction and is turned into lycopene oxidants. We verified this hypothesis by estimating the energy level relationship between astaxanthin and lycopene based on experiment and theoretical calculation and obtained results that support the hypothesis (Fig. 3).

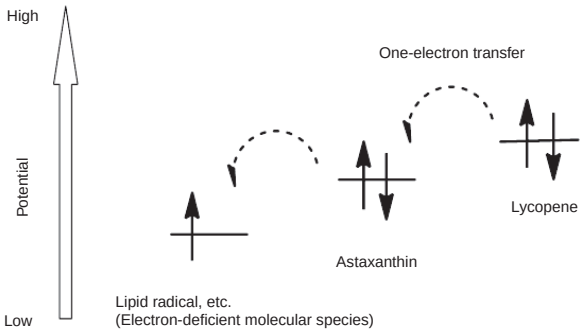

Fig. 3 Hypothesis of intermolecular electron transfer reaction.

2.2 Nanotechnology for lycopene

As described above, lycopene is expected to exhibit high functionality in cosmetics such as face lotion. For that purpose, it is preferable that lycopen be nanonized from the aspect of quality (transparency and stickiness), because of its oil-solubility. However, as it is an unstable substance that decomposes easily, with high crystallizability (Fig. 4), solid nanonization is difficult and had not been realized.

To solve those problems, we developed a new original technology to nanonize lycopene that is subject to crystallization to an extra small size (70 nm) and complexly increase its stability by combining several ingredients. With this technology, it has become possible to create optimal-size original nano-lycopene, transparent and expected to permeate the stratum corneum of skin without losing its usefulness such as high antioxidant capacity (Fig. 5). Thus, we succeeded in including nano-lycopene in all the items of the ASTALIFT range.

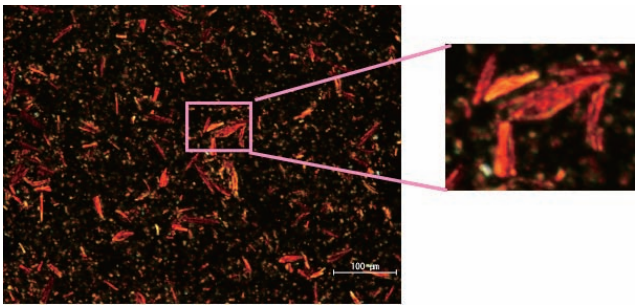

Fig. 4 Optical microscopic image of lycopene (at approx. 100× magnification).

Fig. 5 Transparency comparison between lycopene nano-sized by conventional technology (left) and nano-lycopene developed by Fujifilm (right).

3. Deepening of research on collagen

3.1 Mesh collagen care

In conventional research, the cause of skin resilience being lost with aging was believed to be the change of the dermis as the skin base. However, we built a hypothesis that one of those causes might be the thinning of the skin (epidermis) with aging and conducted close functional observation, focusing on type-IV collagen, or mesh collagen, that has a unique mesh-like structure and exists in abundance in the basal lamina (Fig. 6).

To investigate the effect of mesh collagen on skin, we created a reconstructed skin model in collaboration with Professor Nishiyama of the Tokyo University of Agriculture and Technology. A histological analysis revealed that the reconstructed skin model with mesh collagen can have an epidermis at least twice as thick as the conventional one after

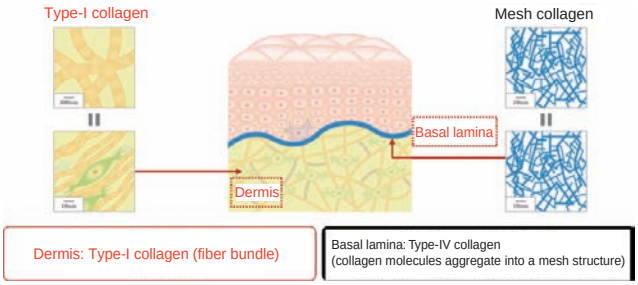

Fig. 6 Localization of Type I collagen and Type IV collagen (mesh collagen).

fourteen days of culture (Fig 7). This result suggests that *in vivo* mesh collagen of normal quality and quantity is a key element for the prevention of the thinning of the epidermis.

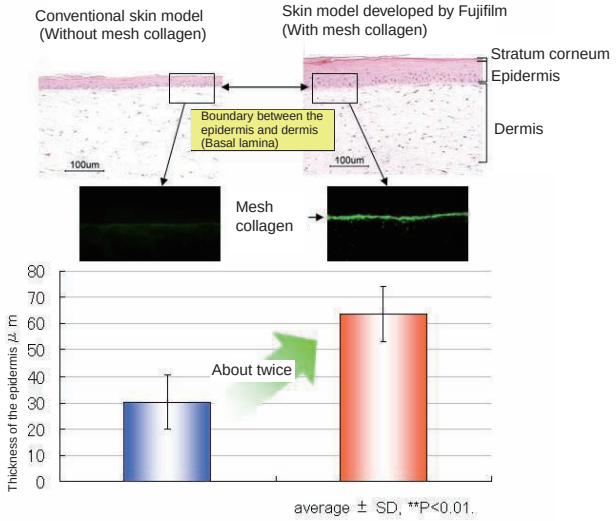

Fig. 7 Effect of mesh collagen on the thickness of the epidermis layer (Comparison of epidermis thickness after 14 days of culture).

3.2 High-permeability resveratrol that protects mesh collagen

Based on our above-described original findings, we started to search for compounds that can protect mesh collagen that is subject to decomposition by external factors such as aging and exposure to UV-rays. By screening of Fujifilm's compound library, we found a powerful type-IV collagen decomposition suppressant capability in a kind of polyphenol, resveratrol. However, resveratrol is weak in stability over time and in permeability. Therefore, we searched through its derivatives and discovered that a methoxy derivative, pterostilbene, has the same level of protective capability as resveratrol (Fig. 8). This compound is a natural ingredient contained in plants such as blueberries.

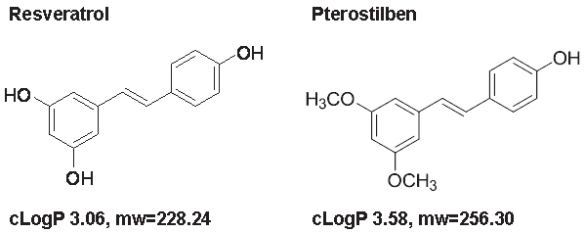

Fig. 8 The molecular structures of resveratrol and pterostilbene.

We then carried out an experiment to test pterostilbene's skin permeability with a 3D skin model and found that it had about thirty times larger permeability than ordinary resveratrol (Fig. 9). According to the calculation of the permeation speed, it can sufficiently permeate the stratum corneum into the basal lamina where mesh collagen exists. Because its stability in water-based dosage forms is high, it is possible to include pterostilbene in cosmetics while maintaining all its benefits (Fig. 10).

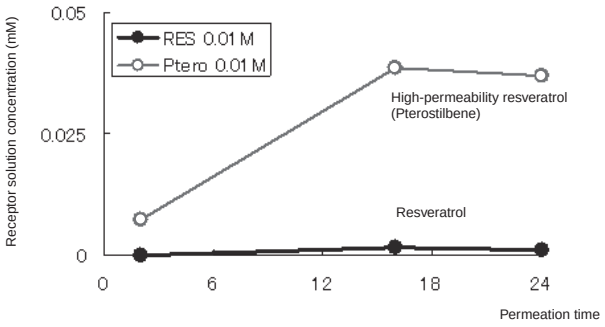

Fig. 9 Permeability of resveratrol in epidermis model.

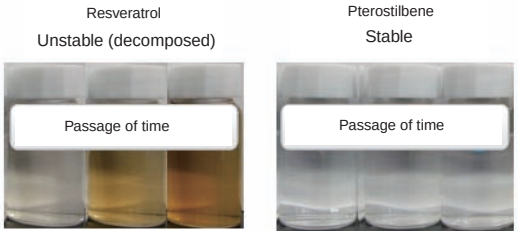

Fig. 10 The stability of resveratrol and pterostilbene under room temperature.

4. Conclusion

In the recent update of the ASTALIFT range, we have succeeded in improving its comprehensive antioxidant capacity by including nano-lycopene in all the items as the power-up ingredient. Moreover, ASTALIFT Essence Destiny, which employs high-permeability resveratrol newly found from the discovery of mesh collagen's involvement in the reproduction of the epidermis, has enabled the care of mesh collagen located deeper than the stratum corneum. It has been confirmed via experiments in accordance with the Guidelines for Evaluation of Anti-wrinkle Products that ASTALIFT Essence Destiny has the effect to make fine wrinkles caused by dryness less visible.

In this way, the ASTALIFT range can be regarded as a highly promising cosmetics brand that helps reproduce bright and resilient *photogenic skin*. Under the product concept of "Advanced cosmetics moving ahead", we will keep introducing valuable products to customers by leveraging our unique technologies.

References

1) Giovannucci, E. et al. J. Natl. Cancer Inst. **94** (5), 391-398 (2002).
2) Jung, Suh.H. et al. Proc. Natl. Acad. Sci. **101** (10), 3381-3386 (2004).

Development of Self-emulsifying DHA Formulation

Hiroyuki SAKAGUCHI*, Nobuyuki HARAGUCHI**, Yuriko ODA*, and Fumitaka UEDA*

Abstract

Various physiological functions as essential fatty acids are reported regarding docosahexaenoic acid (DHA) and eicosapentaenoic acid (EPA). The two acids are polyunsaturated fatty acid (PUFAs). Absorption of DHA is often influenced by meal consumption. We prepared a self-emulsifying DHA formulation which achieved stable and high absorption ability without depending on bile acid. Absorption evaluation on rats revealed that bioavailability of this self-emulsifying DHA formulation was three times higher than that of general DHA fish oil. The evaluation also proved that the formulation has high absorption ability without being affected by food consumption. In conclusion, this formulation technology improved DHA absorption by oral intake, leading to more convenient DHA ingestion.

1. Introduction

In 2006, under the new corporate philosophy, "contributing to the advancement of culture, science, technology and industry, as well as improved health and environmental protection in society and thus helping to enhance the quality of life of people worldwide," Fujifilm stepped into a new domain of preventive medicine, launching functional cosmetics and supplements onto the market.

Those healthcare products have been established based on our various technologies and know-how acquired in the field of photography. For example, the main ingredient of photo films is the same collagen as that of the skin, and skin blemishes and aging share the same cause, oxidation, as photograph color fading. Our collagen handling technology and antioxidant technology can thus be applied to healthcare products directly. In addition, to differentiate our products from those of others, we have been developing new technologies to introduce valuable healthcare products only made available by Fujifilm, placing emphasis on an advanced nanotechnology (FTD technology) that allows precise and effective *in vivo* permeation/absorption of functionally combined ingredients and materials.

With the foregoing background, we succeeded in the development of self-emulsifying formulation technology and released "DHA, EPA & Astaxanthin" onto the market in January 2012 (Fig. 1).

Fig. 1 DHA, EPA and Astaxanthin.

2. Development of DHA, EPA & Astaxanthin

2.1 What is DHA?

Among functional materials used for supplements are vitamin C and B groups that are water-soluble; and vitamin E, docosahexaenoic acid (DHA), coenzyme Q10 and astaxanthin that are oil-soluble. The former are tabletized or encapsulated (hard-type) and the latter are formulated into soft capsules.

Similarly to eicosapentaenoic acid (EPA), DHA (Fig. 2) is a kind of n-3 (ω-3) polyunsaturated fatty acid (PUFA) and blueback fish are rich in it. It also exists abundantly in the retina, heart, and central nervous system of mammals and has been reported to have, as an essential fatty acid, various physiological functions such as blood lipid lowering and antithrombotic effects[1].

Fig. 2 Docosahexaenoic acid.

Since the target intake of DHA and EPA (at least 1 g/day) was specified in Dietary Reference Intakes for Japanese

Original paper (Received December 4, 2012)

* Pharmaceutical & Healthcare Research Laboratories
Research & Development Management Headquarters
FUJIFILM Corporation
Ushijima, Kaisei-machi, Ashigarakami-gun, Kanagawa 258-8577, Japan

** Production & Development Center
FUJIFILM KYOWA KIRIN BIOLOGICS Co., Ltd.
Hagiwara-cho, Takasaki-shi, Gunma 370-0013, Japan

(2010) as shown in Table 1, n-3 PUFAs including those two have been drawing more and more attention as health maintaining ingredients[2]. In this way, DHA and EPA have established their current popularity as supplements and become widely distributed in society.

Table 1 Recommended daily ingestion amount of EPA and DHA for Japanese.

(g/day)

Age	Male	Female
	Target (minimum)	Target (minimum)
18 to 29	1	1
30 to 49	1	1
50 to 69	1	1
70 or over	1	1

2.2 The effect of feeding and fasting on DHA absorption

As supplements can be taken casually and the timing being usually unspecified, the absorption of useful ingredients may vary depending on when they are taken. The raw ingredients of DHA generally used in supplements exist with other fatty acids in the form of triglyceride. After being micellized by bile and hydrolyzed by lipase within the small intestine, they are absorbed by the intestinal epithelium.

It is known that even in rats, which do not have a gallbladder, the secretion of bile is increased when feeding. DHA absorption may vary greatly, depending on the secretion amount of bile.

To verify the difference in DHA absorbability by intake timing (after feeding or fasting), we conducted experiments with rats. The results are shown in Fig. 3. With this time-blood plasma DHA concentration graph, the maximum blood concentration (Cmax), maximum blood concentration time (Tmax) and area under the blood concentration-time curve (AUC) were derived.

As shown in Table 2, DHA absorbability for fed rats did not differ from that for fasted rats in Tmax but Cmax is about 2.7 times and the AUC0-24 about 2.5 times higher than those fasted.

This reveals that DHA absorbability varies greatly depending on the intake timing.

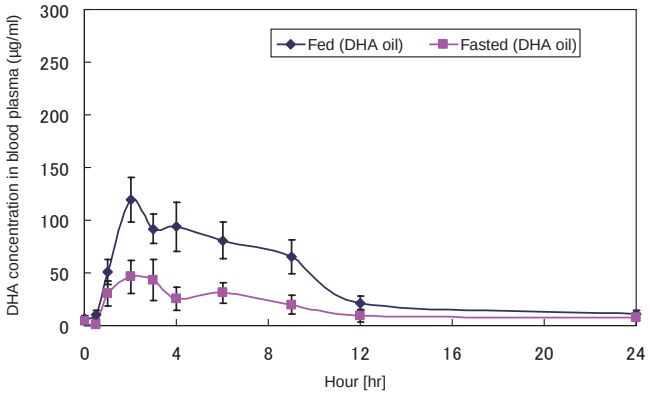

Fig. 3 Plasma concentration profile of DHA.

Table 2 Pharmacokinetic parameters of oral administration of DHA oil to fed rats and fasted rats.

		fed DHA OIL	fasted DHA OIL
C_{max}	μg/ml	119.2±21.2	44.5±15.7
T_{max}	hr	2	2
$AUC_{0\text{-}24h}$	μg・hr/ml	1018.9	405.8*

DHA OIL: Common edible fish oil
Cmax: maximum serum concentration
T_{max}: time to reach the C_{max}, AUC: area under the serum concentration-time curve
Values of C_{max} are the mean ± SEM, n=5 * P<0.1

3. Development of self-emulsifying DHA formulation technology

We increased the absorption of oil-soluble, low-absorbability materials, such as astaxanthin, by converting them into nano-emulsions[3]. This technology is effective for oil-soluble materials such as coenzyme Q10 and carotenoids such as astaxanthin whose necessary intake per day is no more than several dozens of milligrams. However, it was difficult to apply the technology to useful ingredients like DHA whose intake per day needs to be several hundreds of milligrams, because that increases the number of capsules to be taken.

Then, aiming to suppress the increase in the number of capsules while keeping high absorbability, we carried out the development of a self-emulsifying DHA formulation, which is expected to reduce the great effect that bile acid has on the absorption of oil-soluble materials while in a fed state and to thereby achieve high absorbability consistently, regardless of feeding or fasting. Fig. 4 shows the difference between nano-emulsions and the self-emulsifying DHA formulation.

Incidentally, a self-emulsifying formulation does not need the shear stress of homomixers, etc., but employs a surface chemistry technique to formulate fine emulsions (particles) spontaneously with water contact as a trigger and to increase the specific surface area, which improves its absorbability. Fig. 5 illustrates a general preparation method for self-emulsifying formulations and their emulsification mechanism[4].

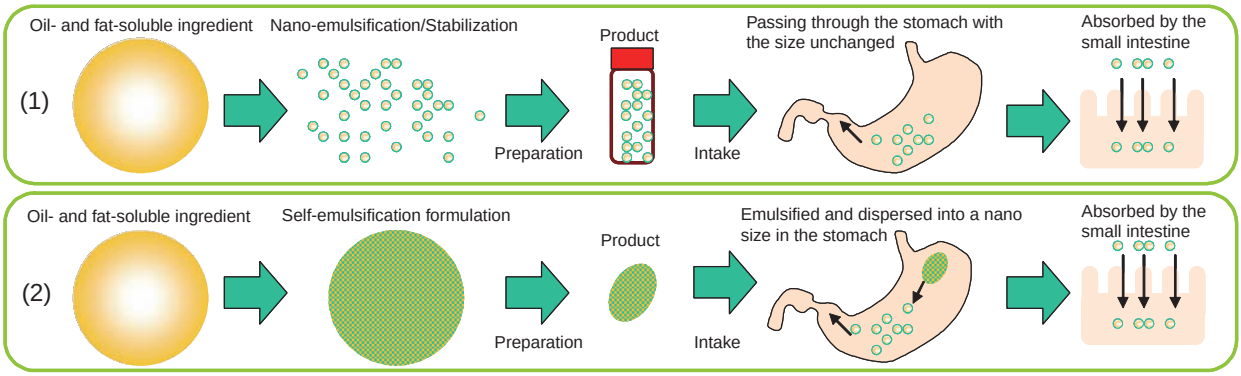

	Characteristics	Suitable materials	Suitable product formulation	Suitable dosage forms
(1) Nano-emulsification	Nanonized and prepared	Materials requiring only a small intake	Mixed with water-based or powder ingredients	Liquid, hard capsules
(2) Self-emulsification	Prepared so that it will be nanonized	Materials requiring a large intake	Mixed with oil-based ingredients	Soft capsules

Fig. 4 Difference in DHA absorption between nano-emulsion and self-emulsification formulations.

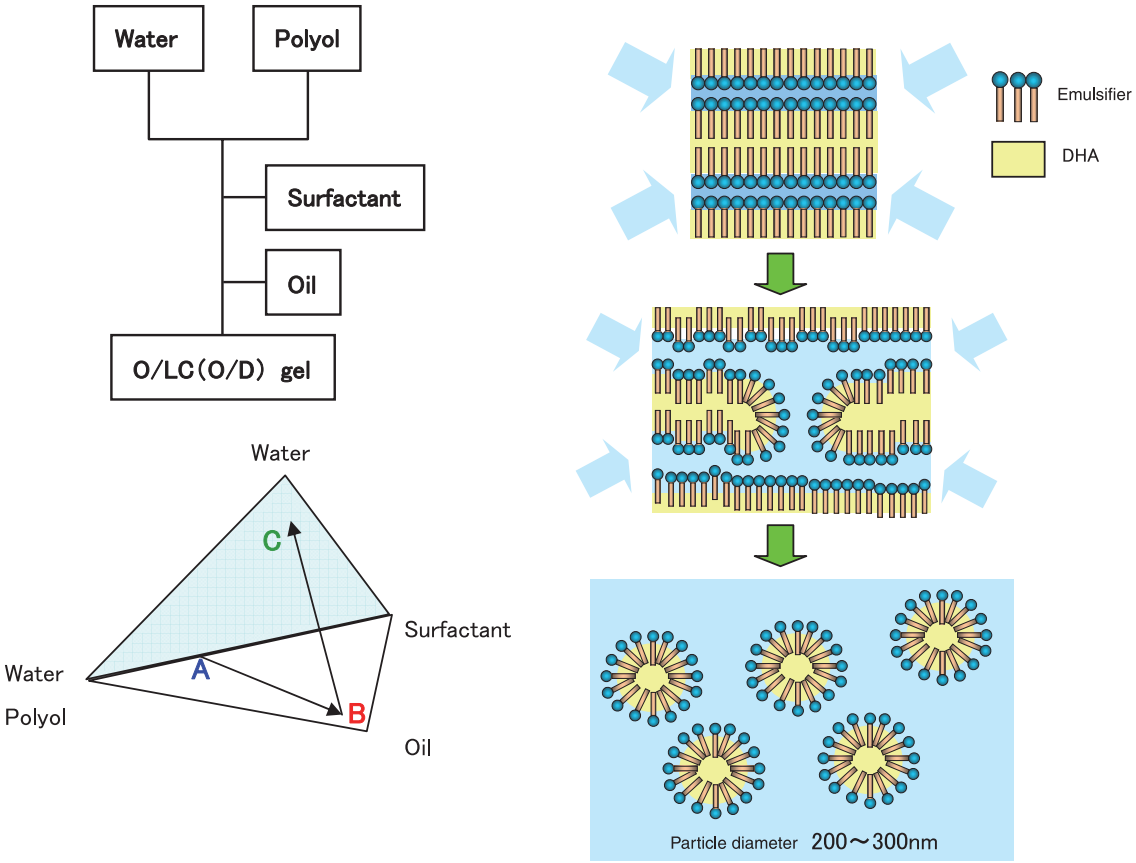

Fig. 5 General self-emulsification preparation and mechanis.

3.1 Assessment of the absorbability of a self-emulsifying DHA formulation (1)

To verify the absorbability of the newly developed self-emulsifying DHA formulation, we first conducted a comparative test with DHA oil commonly used in supplements and self-emulsifying DHA formulation using hungry rats. The results are shown in Fig. 6 and Table 3.

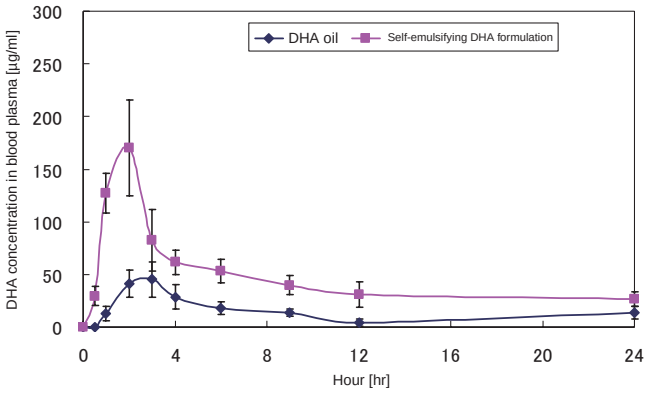

Fig. 6 Plasma concentration profile of DHA.

Table 3 Pharmacokinetic parameters of oral administration of DHA oil and SEDDS-DHA to fasted rats.

		DHA OIL	SEDDS-DHA
C_{max}	μg/ml	45.2±16.8	170.0±45.4
T_{max}	hr	3	2
$AUC_{0\text{-}24h}$	μg·hr/ml	341.3	1100.0**

DHA OIL: Common edible fish oil, SEDDS-DHA: Self-emulsifying DHA formulation
C_{max}: maximum serum concentration, T_{max}: time to reach the C_{max}
AUC: area under the serum concentration-time curve
Values of C_{max} are the mean ± SEM, n=3 ** P<0.05

As shown in the above results, the concentration of DHA in the blood plasma for the self-emulsifying DHA formulation reached its peak (Cmax) two hours after intake and then declined gradually. On the other hand, that for DHA oil commonly used in supplements reached Cmax three hours after intake and then declined gradually. In addition, the AUC for the former is about three times as large as that for the latter. This means that the self-emulsifying DHA formulation had higher absorbability than common DHA oil.

3.2 Assessment of the absorbability of a self-emulsifying DHA formulation (2)

As already described, the DHA absorbability of common DHA oil varies depending on the intake timing. Finally, to verify the DHA absorbability of the self-emulsifying DHA formulation by intake timing, we conducted a comparative test using fed and fasted rats. The test parameters and results are shown in Table 4 and Fig. 7.

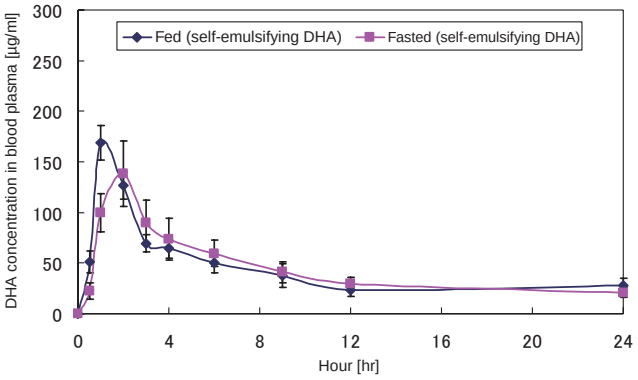

Fig. 7 Plasma concentration profile of DHA.

Table 4 Pharmacokinetic parameters of oral administration of SEDDS-DHA to fed rats and fasted rats.

		fed SEDDS-DHA	fasted SEDDS-DHA
C_{max}	μg/ml	169.1±17.0	138.1±32.2
T_{max}	hr	1	2
$AUC_{0\text{-}24h}$	μg·hr/ml	1028.9	1044.7

SEDDS-DHA: Self-emulsifying DHA formulation
Cmax: maximum serum concentration
T_{max}: time to reach the C_{max}, AUC: area under the serum concentration-time curve
Values of C_{max} are the mean ± SEM, n=5

As shown in the above results, in the case of the fasted group, the concentration of DHA in the blood plasma for the self-emulsifying DHA formulation reached its peak (Cmax) two hours after intake and then declined gradually in the same way as shown in 3.1. On the other hand, in the case of the fed group, the concentration reached Cmax one hour after intake and then declined gradually. No significant difference was observed between the two groups in the AUC. It was apparent that a self-emulsifying DHA formulation can exhibit high absorbability regardless of fasting or feeding.

The one-hour difference between the two groups in the time to reach Cmax is thought to be because the secretion of bile acid of the fed group was larger than that of the fasted group and, consequently, DHA was absorbed faster.

4. Conclusion

For the new product DHA, EPA & Astaxanthin, we developed Aqua-nanosizing DHA that reacts with the water taken together with the supplement and spontaneously nanonizes itself *in vivo*. It is hardly affected by intake timing, either feeding or fasting, and can exhibit high absorbability constantly. In the future, we will further utilize a characteristic technology of ours called FTD to develop valuable functional food products and thereby contribute widely to society, improving the quality of people's life.

References

1) Suzuki, H., et al. *Suisan Shokuhin Eiyo-gaku - Kiso kara Hito he* (Seafood Dietetics - From Basics to Man). Gihodo Shuppan (2004)
2) Dietary Reference Intakes for Japanese (2010). Ministry of Health, Labour and Welfare (2009)
3) Suzuki, K., et al. Development of Astaxanthin Nano-Emulsion with Improved Shelf Life and Enhanced Absorbability. Fujifilm Research & Development No. 52, 27-29 (2007)
4) Binks, B.P. ed. Modern Aspects of Emusion Science. Royal Society of Chemistry. Cambridge (1998).

Development of Higher Performance Tape Media for Enterprise Data Storage Systems by using Barium Ferrite Magnetic Particles

Hiroaki TAKANO*, Masahiko ASAI*, Masahito OYANAGI*,
Tadahiro OHISHI*, and Masayuki USUI*

Abstract

The magnetic tape using barium ferrite magnetic particles instead of traditional metal magnetic particles demonstrated much higher areal recording density of 6.7Gbit/in^2 in 2007 and 29.5Gbit/in^2 in 2010. We applied NANOCUBIC technology to the barium ferrite material through these demonstrations, and moved these technical achievements into the production phase while increasing the durability. For enterprise-class systems, we released in 2011 the reliable magnetic tape products that have an approximately three times larger storage capacity than LTO Generation 5 tape. This proves that Fujifilm's barium ferrite technology can contribute to an increase in the storage capacity of magnetic tape in response to the market needs for data storage systems having higher capacity.

1. Introduction

In the digital data storage market, demands for reliability and cost effectiveness have kept increasing. Magnetic tape is highly regarded in the market because of its low price per unit capacity and running cost as well as its high reliability for long-term storage. Since 1990s, a cartridge capacity of the linear tape system had kept increasing by 40% annually, that is, at a pace that nearly doubles the capacity every two years. However, in recent years, the uptrend of capacity increase has slowed down; for the micronization of metal magnetic particles is reaching its limit. As a breakthrough, magnetic particles with magneto-crystalline anisotropy such as barium ferrite (hereinafter "BaFe") had long been studied[1), 2)], but the potential of BaFe magnetic particles could not be fully realized for the following reasons: such fine particles as BaFe are difficult to synthesize and disperse evenly; and, because of their low magnetizability, low-sensitivity magnetic heads cannot achieve a satisfactory signal-to-noise ratio (SNR). Under such circumstances, we succeeded in deriving high performance from BaFe magnetic particles with NANOCUBIC technology [3) to 9)] and, in collaboration with system integrators, realized technology demonstrations[4), 8)] (hereinafter "tech demo") with areal recording densities of 6.7 Gbit/in^2 and 29.5 Gbit/in^2. Fig. 1 shows the trends of areal recording densities for hard disks and the linear tape system. The recording densities achieved by the two tech demos indicated that, by using BaFe magnetic particles, it is possible to re-establish the stalled upward progress of densities of linear tape products.

By applying the technology introduced to the 6.7 Gbit/in^2 tech demo, we developed an eminently practical, high-capacity magnetic tape and launched it onto the enterprise storage market where there is a requirement for high reliability.

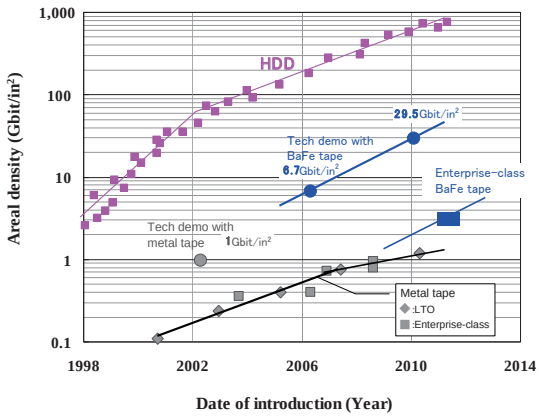

Fig. 1 Recording areal densities of general hard-disk drive and tape products, and the tape used in the demonstrations.

2. Design of high recording-density magnetic tape

Three key NANOCUBIC technologies are employed to increase the recording density of magnetic particle-coated tape: (a) nano particle utilization (nanonized magnetic particles); (b) nano dispersion (dispersion of nanonized magnetic particles); and (c) nano coating (even, thin magnetic layer coating). With those technologies, we enhanced the tape's recording density and succeeded in achieving a quality level that enables industrial mass production.

Original paper (Received December 28, 2012)

* Recording Media Research Laboratories
Research & Development Management Headquarters
FUJIFILM Corporation
Ohgi-cho, Odawara, Kanagawa 250-0001, Japan

2.1 Nano particle utilization (nanonized magnetic particles)

The magnetic anisotropy of conventionally-used metal magnetic particles is derived from shape anisotropy. Their major axis length has already been shortened and nanonized to a level previously regarded as impossible to achieve but further micronization cannot be expected because it is difficult to maintain coercivity provided by the acicular particle shape and to retain a film of oxide. In contrast, nanonization and high coercivity are compatible in BaFe magnetic particles because their magnetic anisotropy is derived mainly from magneto-crystalline anisotropy. They are hexagonal plate-like particles and the easy axis of magnetization is perpendicular to the plate face. In addition, as an oxide, they are more stable in the air than metal magnetic particles. Table 1 and Fig. 2 show the properties of the BaFe magnetic particles developed for the 6.7 Gbit/in^2 tech demo and the metal magnetic particles used for LTO-5. In the tape media for enterprise systems, we employed the former nano particles with a plate diameter of 21 nm whose volume is 26% smaller than that of the latter particles.

Table 1 Comparison between a metal particle and BaFe particle.

	Metal particle (LTO5)	BaFe particle
Size [nm]	37	21
Volume [nm^3]	2850	2100
Hc [Oe]	2380	2280
σs [emu/g]	105	50

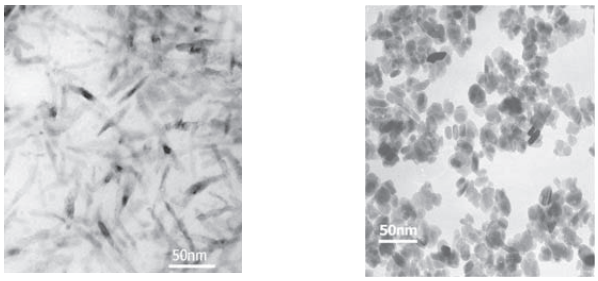

(a) Metal particles (b) BaFe particles

Fig. 2 TEM images of magnetic material: (a) Metal particles and (b) BaFe particles.

2.2 Nano dispersion (dispersion of nanonized magnetic particles)

In magnetic tape, to suppress the generation of noise signal, it is important to form an uniform coating of magnetic particles without causing their aggregation. In this industry, sand mill disperser is commonly used with ceramic or glass beads. To disperse the employed BaFe nano magnetic particles uniformly, a high-dispersion mass production line has been installed on which the efficiency is improved dramatically over conventional lines. BaFe magnetic particles can readily become stacked because their axis of easy magnetization is perpendicular to the plate face, which can easily cause the re-aggregation of particles after dispersion. To prevent this problem, we introduced a technology to make organic materials such as binders adhere between magnetic particles as a steric hindrance. The more binders that exist between magnetic particles, the more easily the steric hindrance can be formed. However, it decreases the recording performance of magnetic tape because the packing density of the magnetic particles declines. Having studied dispersion agents and the polar groups of polymers optimal for BaFe magnetic particles, we then succeeded in making the minimum necessary amount of binders adhere uniformly to the magnetic particle surface with a high adhesion rate, thereby preventing re-aggregation caused by stacking.

Fig. 3 provides SEM images of the surface of the magnetic layer applied to the base material after dispersion. As shown in Fig. 3 (b), magnetic particles are separated evenly with our new dispersion technology, compared with the conventional dispersion conditions in Fig. 3 (a).

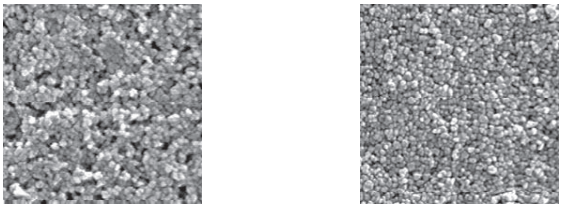

(a) Conventional dispersion conditions (b) New dispersion conditions

Fig. 3 SEM images of magnetic layer surfaces under (a) conventional dispersion conditions and (b) new dispersion conditions using nano-dispersion technology.

2.3 Nano coating (uniform, thin magnetic layer coating)

To increase recording densities, it is important to improve the resolution of recording signals by obtaining sharp, inverted solitary waves, which requires the thinning of the magnetic layer. We have introduced onto the market an extensive range of products including the consumer-use video tape Hi8 in the 1990s and data storage DLT or LTO, with a technology to enable the thinning of the magnetic layer by coating it simultaneously on the non-magnetic underlayer (i.e., ATOMM technology). However, with the progress of the shortening of recording wavelengths, the required thickness of the magnetic layer has become 100 nm or even less, which has brought us a new problem. The irregular interface between the two layers resulting from the upper layer thinning causes noise, which affects the electromagnetic conversion characteristics. Mixing of the upper and under layer coatings is the cause of the fluctuations of the interface. Therefore, we reviewed the thixotropy and application method of the coating solutions and realized a

coating method that can form a thin magnetic layer while keeping the fluctuations to a minimum. Fig. 4 provides cross-sectional TEM images of the interfaces observed between the magnetic layer and the non-magnetic underlayer. As shown in Fig. 4 (b), the interface formed with the newly introduced thin coating technology is far flatter than that formed with a conventional coating method in Fig. 4 (a).

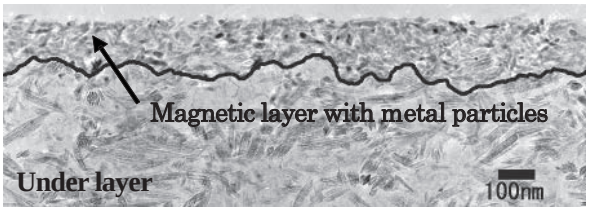

(a) Conventional coating conditions

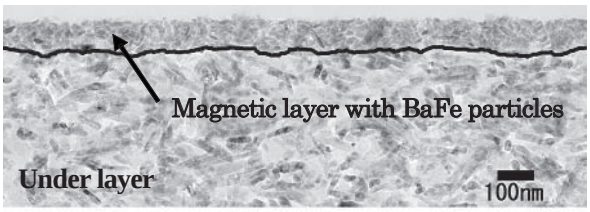

(b) New coating conditions

Fig. 4 Cross-sectional TEM images of interfaces between magnetic and non-magnetic-layer under (a) conventional coating conditions and (b) new coating conditions using nano-coating technology.

3. Design of durability

3.1 Compatibility of slidability and electromagnetic conversion characteristics

The spacing between the magnetic head and tape surface results in a decrease of read/write performance. Decreasing this spacing can greatly improve the SNR, particularly in the short wavelength area. However, at the same time, the consequent widened real contact area increases friction. Table 2 shows the surface roughness of the magnetic layers and the coefficients of friction of the newly developed tape for enterprise use, the 6.7 Gbit/in^2 tech demo, and an LTO-5 product using metal magnetic particles. The surface roughness profiles of those three media are shown in Fig. 5. The surface roughness was measured with an optical interferometric profiler (OIP). Ra and Rz values represent mean surface roughness and ten-point mean roughness, respectively. The coefficients of friction were measured at a tape tension of 0.98 (N) and at a low tape speed of 14 mm/s against an AlTiC bar whose surface roughness is equivalent to that of the magnetic head.

Table 2 Surface roughness measured with optical interferometric profiler (OIP) and friction with AlTiC bar.

	LTOG5	6.7 Gbit/in2 tech demo tape	Enterprise-class tape
Ra [nm]	1.7	1.3	1.4
Rz [nm]	35	23	20
Number of 20 nm-high protrusions (ratio)	12	1	5
Coefficient of friction	0.30	＞0.5	0.28

The 6.7 Gbit/in^2 tech demo tape had a very smooth magnetic layer surface. This achieved a small spacing between the tape surface and the magnetic head, as a result the SNR was improved. However, the friction against the magnetic head became higher. Therefore, in the development of the enterprise-class tape, to solve that problem, we controlled the particle distribution of fillers which were added to magnetic layer to ensure slidability and durability. By doing so, it became possible to maintain the Ra and Rz values of the enterprise-class tape to the same level as those of the 6.7 Gbit/in^2 tech demo tape while the number of small protrusions increased a little. In this way, a narrow spacing between the magnetic head and tape surface and high slidability have been achieved.

Fig. 6 shows reproduced signal spectra at a track recording density of 275 kfci with a GMR head whose track width is 0.5 μm. It indicates that the enterprise-class tape achieves a high SNR, obtaining a very sharp signal spectrum, while keeping a noise level as low as that of the 6.7 Gbit/in^2 tech demo tape.

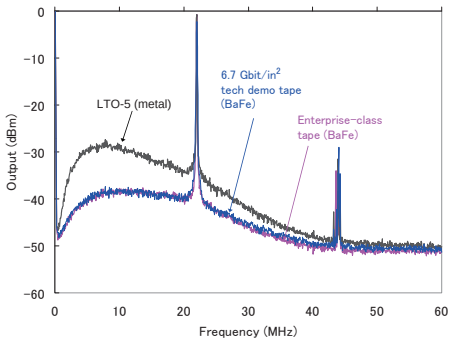

Fig. 6 Signal and modulation noise spectra.

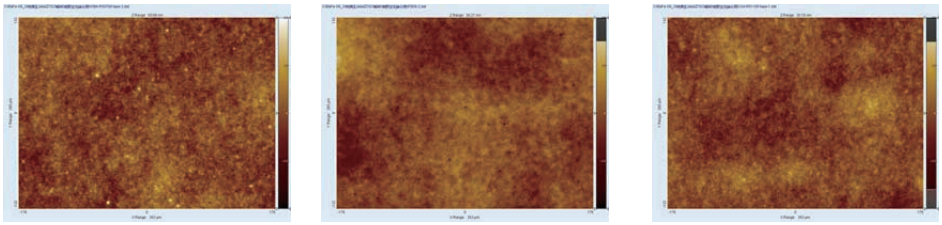

(a) LTO-5 (b) 6.7 Gbit/in^2 tech demo tape (c) Enterprise-class tape

Fig. 5 Surface profiles measured with optical interferometric profiler.

3.2 Long-term storage

The test method widely used in the magnetic tape industry as an index for the storage performance of magnetic tape is the aging test carried out under an accelerated environment with corrosive gas, the Battelle Class II[10] environment, developed by Battelle Memorial Institute[11), 12)].

The Battelle Class II environmental conditions of the test that we conducted are as shown in Table 3. The duration was fourteen days accelerated by approximately 400 to 1000 times[13)], which is equivalent to fifteen to thirty-eight years. The tape using BaFe magnetic particles was left with its surface exposed in the environment. For the tape using metal magnetic particles, we prepared two test pieces: one was left with its surface exposed in the environment and the other was left in a cartridge. After fourteen days, we investigated the changes in the tape surface conditions and in the products of residual magnetization and magnetic layer thickness[9)]. Normally, magnetic tape is reeled inside a cartridge and makes hardly any contact with the external air. Therefore, the condition in which the surface is exposed is quite a harsh environment for it. The metal magnetic particle tape, including the portion just after the leader, left inside the cartridge was not corroded at all and no change occurred in its magnetization. However, the one with its surface exposed to the environment was corroded and its magnetization level decreased greatly. In contrast, any changes were hardly observed on the surface of the tape using BaFe magnetic particles and its magnetization level was kept unchanged as shown in Table 4. These results indicate the extremely high chemical stability of BaFe magnetic particles. Further nanonization of magnetic particles will become essential in the future. Under such circumstances, BaFe magnetic particles are promising compared with conventional metal ones in the light of stability for long-term data storage.

Table 3 Conditions for gas environmental test.

Cl_2 concentration	10ppb
NO_2 concentration	200ppb
H_2S concentration	10ppb
Relative humidity	70%
Temperature	30℃

Table 4 Change in Mrt (remanent magnetization X thickness) value in Battelle Class Ⅱ test.

	Before [mA]	After [mA]	Ratio
BeFe tape	3.1	3.1	1.00
Metal tape (LTO4)	19.5	12.5	0.64
Metal tape (in cartridge)	21.4	21.7	1.01

4. Conclusion

In 2011, five years after the 6.7 Gbit/in^2 tech demo in 2006, we launched onto the market a highly reliable, high-capacity magnetic tape for enterprise data storage systems. The product is the fruit of our original BaFe magnetic particle technology cultivated in the development of the tech demo and NANOCUBIC technology with durability improved. The recording capacity is about three times as large as that of LTO-5 released in the previous year. It revitalized the declining rate of recording capacity expansion of tape systems more than expected by the industry. In recent years, information terminals have been becoming more and more diverse, and it is expected that needs for high-capacity data storage will keep increasing in the future. As the recording capacity and density requested from customers have already reached a level that cannot be achieved with conventional metal magnetic particles, expectations for magnetic tapes using BaFe magnetic particles are high. We will keep developing higher-capacity magnetic tape by improving the performance of BaFe magnetic particles, introducing more advanced uniformly coating techniques and improving the interfacing of the magnetic head and tape surface.

References

1) Fujiwara, T.; Isshiki, M.; Koike, Y.; Oguchi, T. Recording performances of Ba-ferrite coated perpendicular magnetic tapes. IEEE Trans. Magn. **18** (6), 1200-1202 (1982).
2) Kubo, O.; Ido, T.; Yokoyama, H. Properties of Ba ferraite particles for perpendicular magnetic recording media. IEEE Trans. Magn. **18** (6), 1122-1124 (1982).
3) Nagata, T.; Harasawa, T.; Oyanagi, M.; Abe, N.; Saito, S. A Recording Density Study of Advanced Barium-Ferrite Particulate Tape. IEEE Trans. Magn. **42** (10), 2312-2314 (2006).
4) Berman, D.; Biskeborn, R.; Bui, N.; Childers, E.; Cideciyan, R.D; Dyer, W.; Eleftheriou, E.; Hellman, D.; Hutchins, R.; Imaino, W.; Jaquette, G.; Jelitto, J.; Jubert, P.-O.; Lo, C.; McClelland, G.; Narayan, S.; Ölçer, S.; Topuria, T.; Harasawa, T.; Hashimoto, A.; Nagata, T.; Ohtsu, H.; Saito, S. 6.7 Gb/in^2 Recording Areal Density on Barium Ferrite Tape. IEEE Trans. Magn. **43** (8), 3502-3508 (2007).
5) Ölçer, S.; Eleftheriou, E.; Hutchins, R.A.; Noguchi, H.; Asai, M.; Takano, H. Performance of Advanced Data-Detection Schemes on Barium-Ferrite Particulate Media. IEEE Trans. Magn. **45** (10), 3765-3768 (2009).
6) Matsumoto, A.; Murata, Y.; Musha, A.; Matsubaguchi, S.; Shimizu, O. High Recording Density Tape Using Fine Barium-Ferrite Particles With Improved Thermal Stability. IEEE Trans. Magn. **46** (5), 1208-1211 (2010).

7) Harasawa, T.; Suzuki, R.; Shimizu, O.; Ölçer, S.; Eleftheriou, E. Barium-Ferrite Particulate Media for High-Recording-Density Tape Storage Systems. IEEE Trans. Magn. **46** (6), 1894-1897 (2010).
8) Cherubini, G.; Cideciyan, R.D.; Dellmann, L.; Eleftheriou, E.; Haeberle, W.; Jelitto, J.; Kartik, V.; Lantz, M.A.; Ölçer, S.; Pantazi, A.; Rothuizen, H.E; Berman, D.; Imaino, W.; Jubert, P.-O.; McClelland, G.; Koeppe, P.V; Tsuruta, K.; Harasawa, T.; Murata, Y.; Musha, A.; Noguchi, H.; Ohtsu, H.; Shimizu, O.; Suzuki, R. 29.5 Gb/in^2 Recording Areal Density on Barium Ferrite Tape. IEEE Trans. Magn. **47** (1), 137-147, (2011).
9) Shimizu, O. et al. Ba-ferrite Particulate Media for Linear Tape System. J. Magn. Soc. Jpn. **35**, 27-33 (2011).
10) Abbott, W.H. The development and performance characteristics of mixed flowing gas test environments. IEEE Trans. Components, Hybrids, Manuf. Technol. **11** (1), 22-35 (1988).
11) Sides, P.J; Spratt, G.; Kampf, J.P. An investigation of the archivability of metal particle tape. IEEE Trans. Magn, **30** (6), 4059-4064 (1994).
12) Iwano, T.; Kobayashi, K. Improving the corrosion resistance of metal-evaporated tape using dicarboxy acid as a lubricant. IEEE Trans. Magn. **41** (10), 3010-3012 (2005).
13) Abbott, D.C.; Frechette, R.A.; Haynes, G.; Romm, D.W. Shelf-Life Evaluation of Nickel/Palladium Lead Finish for Integrated Circuits. Texas Instruments Application Note (1998).
http://www.ti.com/lit/an/szza002/szza002.pdf, (accessed 2012-12-26).

Long Run Length Positive Thermal CTP System “XL-T”

Norio AOSHIMA*, Noriaki WATANABE*, Shigekatsu FUJII**, Takashi ARIDOMI***, Yoichiro ARA*, Mamoru KURAMOTO*, Yoshinori TAGUCHI****, and Yuichi YASUHARA*****

Abstract

We have developed a positive thermal CTP (Computer To Plate) plate “XL-T”, which employs high durability urethane resin for the photo sensitive layer. XL-T is suitable for long run length jobs, for example, printing of forms, ledgers, magazines, and so on. We have also formulated special developer “XL-D” and replenisher “XL-DR” for XL-T, which can be used in a highly concentrated state. Together with the apparatuses for reducing waste developer/rinse water “XR-2000/5000”, the XL-T system realizes reduction of waste solutions equal to that with the XP-series, which are standard positive thermal CTP systems.

1. Introduction

In the printing industries, various approaches have been taken for the reduction of environmental burden. Among them is the Green Printing accreditation and certification scheme which was established by the Japan Federation of Printing Industries to promote the introduction of low environmental burden printing systems.

As a printing plate manufacturer, Fujifilm has engaged in the reduction of industrial waste by designing *computer-to-plate* (CTP) systems to discharge a smaller amount of waste developer and the PLATE to PLATE system to enable closed-loop recycling of the aluminum used as the base material for CTP plates. Also, it has reduced the use of packing materials such as cardboard boxes for external packing and paper and cardboards for inner packing.

In those activities, our main focus has been on eco-friendly CTP systems and we have extended the lineup[1)] to include the process-less CTP system “*Eco & Free System XZ-R*” that produces no waste developer and the positive thermal CTP plate “*XP-Series*” that produces much less waste developer by incorporating the waste developer reduction equipment “*XR-2000/5000*”.

This paper introduces the positive thermal CTP plate “*XL-T*” (Photo 1, Fig. 1) which has been developed after those efforts to meet the tough requirements of long print runs of forms, ledgers and magazines.

Photo 1 Positive thermal CTP plate XL-T.

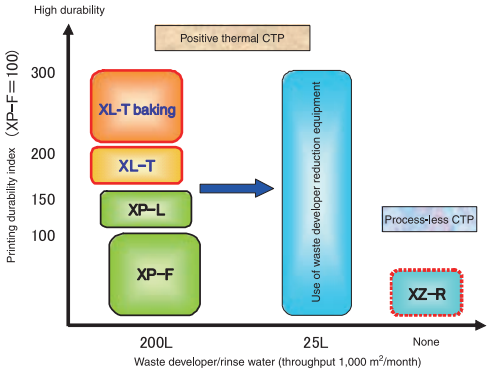

Fig. 1 Quality target for XL-T.

Original paper (Received November 19, 2012)

* Research & Development Center
Yoshida-Minami Factory
FUJIFILM Corporation
Kawashiri, Yoshida-cho, Haibara-gun, Shizuoka 421-0396, Japan

** Technical Support & Product Development Division #1
FUJIFILM GLOBAL GRAPHIC SYSTEMS Co., Ltd.
Fujifilm Nishiazabu Bldg.
Nishiazabu, Minato-ku, Tokyo 106-0031, Japan

*** Flat Panel Display Materials Research Laboratories
Research & Development Management Headquarters
FUJIFILM Corporation
Ohnakazato, Fujinomiya-shi, Shizuoka 418-8666, Japan

**** Electronic Materials Research Laboratories
Research & Development Management Headquarters
FUJIFILM Corporation
Kawashiri, Yoshida-cho, Haibara-gun, Shizuoka 421-0396, Japan

***** Synthetic Organic Chemistry Laboratories
Research & Development Management Headquarters
FUJIFILM Corporation
Kawashiri, Yoshida-cho, Haibara-gun, Shizuoka 421-0396, Japan

2. Issues in improving the printing durability of the positive thermal CTP plate

The positive thermal CTP plate "*XP-F*" with standard printing durability has a stratified photosensitive layer. It forms images by breaking the hydrogen bonds of novolac resin using heat generated during image exposure and thereby improving its solubility in alkaline developers. However, the temperature attained by the photosensitive layer near the aluminum base is low because of thermal diffusion to the base during exposure. This prevents sufficient breaking of the hydrogen bonds and, consequently, causes low sensitivity of the layer. Therefore, while the upper layer, which reaches a high temperature, achieves image formation, the underlayer uses acrylic resin to have high developability even in the absence of strong exposure. In addition, it is necessary for the upper layer to be thin and made from novolac resin, excellent in image formation, to create high-sensitivity images[2]. Because novolac resin is inferior to acrylic resin in printing durability, the contribution of the upper layer to printing durability is kept to merely one-fourth that of the underlayer.

As described above, image formation is left to the upper layer and there is little room for changing its design because of many restrictions on materials and the application quantity. Therefore, we sought a way to improve the underlayer as it contributes greatly to printing durability and allows more flexible design, having few restrictions on image formation.

The simplest way to enhance the printing durability of the underlayer is to increase the amount of the applied acrylic resin. In fact, XP-L achieves about 1.5 times the printing durability of XP-F by doing so. However, it is not without its problems. Within twelve seconds of the underlayer being soaked in the developer, the exposed area needs to be removed as a result of the development process, while the unexposed area should remain unaffected by the developer that penetrates from the imaging area. Therefore, the increased application of acrylic resin to the underlayer requires a larger *discrimination*, a difference in the speed of development between the exposed and unexposed areas. Otherwise, the exposed area cannot be removed completely during the development and the photosensitive layer will remain as a resist film. That causes printing stains or the so-called side-etching in which the surroundings of the unexposed area are affected by the developer and the image area becomes smaller[2] (Fig. 2).

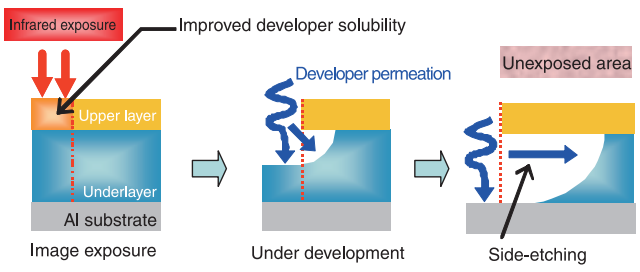

Fig. 2 Mechanism of side-etching.

The target printing durability of XL-T was about twice that of XP-F. That cannot be achieved solely by increasing the amount of the applied acrylic resin because its capacity is insufficient in both printing durability and discrimination. It was necessary to use a durability-enhanced resin for the underlayer without increasing the application amount.

This paper describes the details of the design of the CTP plate XL-T, the developer "XL-D" and the replenisher "XL-DR" which together achieve an optimum printing durability-discrimination balance.

2.1 CTP plate XL-T

High printing-durability resin needs damage-resistant properties to withstand, during printing, the stress applied to the photosensitive layer of the image area by ink rollers and blankets. For example, it may be necessary to increase hardness to suppress deformation and wear or to reduce the stress by utilizing viscoelasticity. We employed urethane resin in XL-T because it exhibits higher printing durability with the same level of developability as acrylic resin and, among the possible alternatives, is excellent in balance with developability. Its high stress-relaxation capability allows easy permeation of developers compared with other hard, high-density resins and this works advantageously on developability. In addition, it has already been used on photopolymer-type CTP plates. We thus selected urethane resin as the replacement for acrylic resin.

There are two improvements to be made when using urethane resin instead of acrylic resin for the underlayer: discrimination and printing durability with UV-ink. The upper novolac layer and the urethane resin underlayer are close in polarity and solvents that do not dissolve the underlayer cannot be used for the coating of the upper layer, which results in the mixture of the layers. In addition, the underlayer does not have a property to inhibit dissolution. Those features are the cause of insufficient discrimination. In a similar way, the cause of insufficient printing durability with UV-ink is the closeness of polarities between UV-ink and urethane resin. This makes urethane resin subject to damage by UV-ink. To solve those two problems, it was essential to design urethane resin so that its polarity is as high as that of acrylic resin used in XP-F and thereby to achieve a polarity far enough from that of novolac resin and UV-ink (Fig. 3).

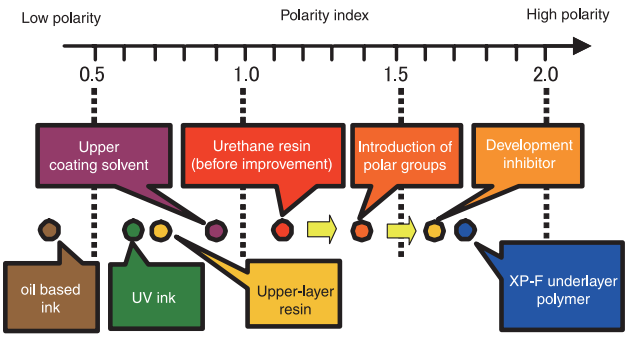

Fig. 3 Process of enhancing dipole moment.

To achieve high polarity in urethane resin, two approaches were taken.

The first approach was to introduce to urethane resin a structure that had already been employed in the acrylic resin underlayer of XP-F to achieve a higher polarity. This structure can also increase solubility in alkaline developers without impairing developability and allows application with few quantitative restrictions. As a result, we achieved the target UV-ink printing durability. However, the mixing of layers during the application of the upper layer could not be prevented with this structure and discrimination was yet to be improved.

The second approach was to establish ionic interactions with the acid group of urethane resin. This led to a further increase in the polarity of urethane resin and, finally, solved the problem of mixing layers.

As those interactions protect the acid group, the dissolution of urethane resin in developers can also be inhibited, that is, a development inhibition effect appears. This effect is cancelled by heat generated during image exposure at the same time as it happens in the upper novolac layer and thereby provides the required discrimination to the underlayer.

The optimization of the polarity, molecule size and hydrophilic/hydrophobic property of this development inhibitor enabled the maximization of discrimination and, by using it in combination with the special developer described below, achieved the design of a CTP plate with high sensitivity equivalent to that of XP-F without forming a resist film or side-etching.

Fig. 4 shows the enhanced discrimination when the development inhibitor was added to the underlayer. The more dosage of the inhibitor, the longer it took before the photosensitive layer of the unexposed area was permeated by the developer.

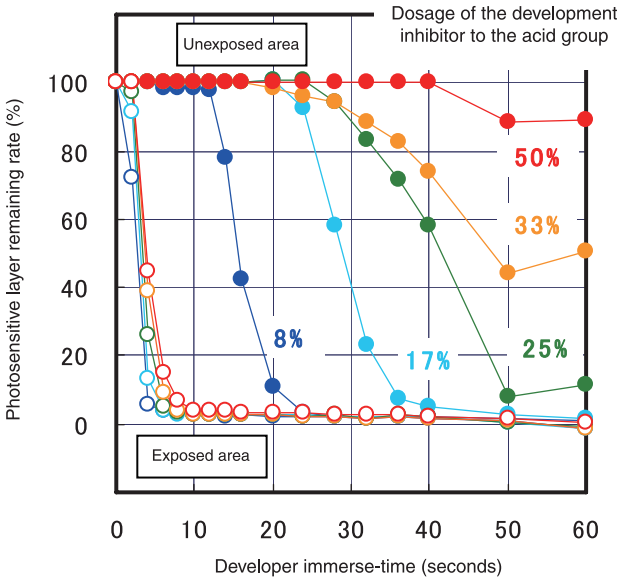

Fig. 4 Effect of development inhibitor.

Photo 2 provides two electron micrograph images of a 50% halftone-dot amplitude modulation screen. Before improvement, the halftone dot size was small because of side-etching and the peaks of the upper layer left at the edges of the image area bent to be deposited as residuals. In the XL-T product, they were eliminated.

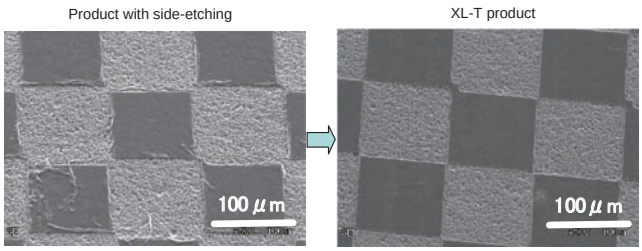

Photo 2 Effect of side-etching control.

Moreover, the structure of the urethane resin is designed to exhibit a thermosetting property at the range of temperatures of the heating process (baking) after development. This property further increases printing durability by at least 1.5 times and greatly enhances durability against UV-ink and its cleansing agent. The applicability of the baking process to some tasks is one of the biggest features of XL-T (Fig. 1).

2.2 Developer XL-D and replenisher XL-DR

Even after the introduction of the above-described technology, urethane resin with high printing durability is still inferior in discrimination and dispersibility into developers, compared with the acrylic resin used in XP-F. Therefore, with the developer XP-D used for XP-F, development is delayed, which results in the formation of a resist film of residuals on the photosensitive layer. If urethane resin is designed to have higher developability in the exposed area to inhibit the formation of the resist film, the endurance of the unexposed area against the developer becomes insufficient, which causes dissolution (Fig. 5).

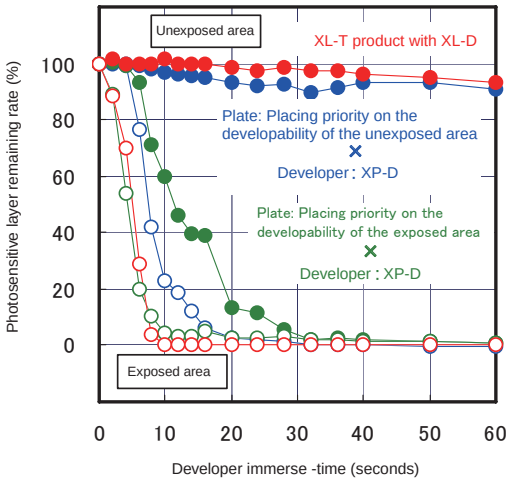

Fig. 5 Discrimination of developed and undeveloped areas.

As a breakthrough for this interrelation, we decided to increase discrimination by improving the developer.

To that end, it was necessary to provide the developer with properties that inhibit the development of the unexposed area while promoting the development of the exposed area. We achieved those properties by using a development activation regulator. The regulator inhibits the permeation of the developer in the unexposed area by interacting with the surface of the upper novolac layer. On the other hand, in the exposed area, the dissolution of novolac resin, whose developability is increased, becomes dominant and the development of the upper layer thus advances. Furthermore, when permeating the underlayer, the developer interacts with the urethane resin and promotes the dissolution and dispersion of that layer. By controlling the interaction of the resins used in the upper and under layers properly, the two antithetic properties of inhibiting and promoting development have become compatible (Fig. 5, Fig. 6).

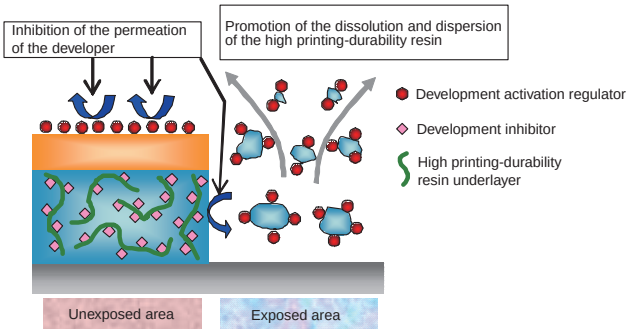

Fig. 6 Development mechanism of XL-T.

Fig. 7 shows the results for a simulation of the dissolution and dispersion of the photosensitive layer of XL-T soaked in the developers, XP-D and XL-D. The former could not achieve sufficient developability and, thus, development advanced while the photosensitive layer was dispersing in a lump. In contrast, the latter dissolved the layer completely.

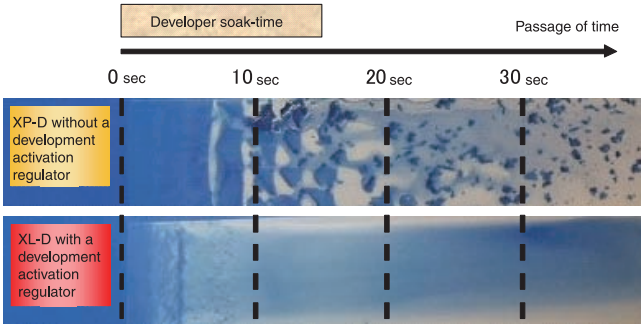

Fig. 7 Dispersion promoting effect of XL-D.

As the developed photosensitive layer is stable in XL-D, the inside of automatic developing equipment is less prone to contamination. Photo 3 shows the states of the developing bath of automatic developing equipment before and after a long-term continuous use test. There are no residuals of the photosensitive layer observed after the test. Cleaning requires only rising with water. The developer is thus excellent in maintenance for replacement.

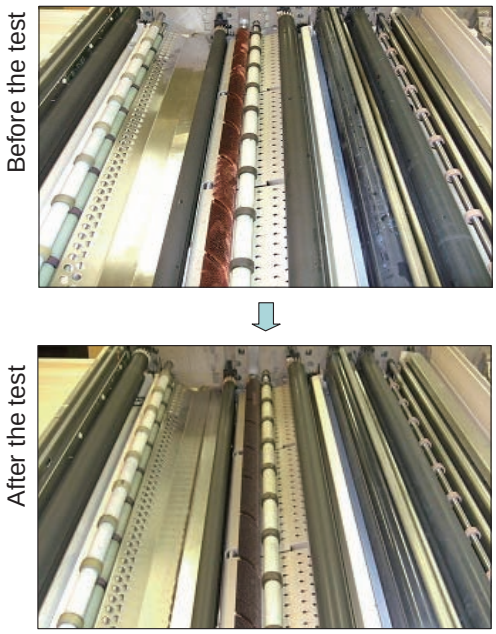

Photo 3 XL-D keeping developer bath clean.

To achieve a developer that had a similar low waste generation to the XP-series, we selected a development activation regulator with a high pH so that salting-out would not occur even at a high ion concentration. This property realizes the high-concentration replenisher XL-DR and, consequently, enables the reduction of waste solution overflow. In the vacuum-distillation waste developer reduction equipment XR-2000/5000, it has become possible to concentrate waste developer together with rinse water to about one-eighth (Fig. 8).

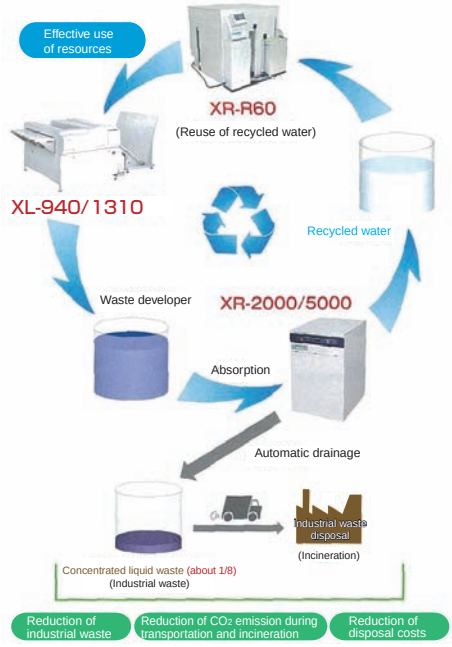

Fig. 8 Systematic view of reducing waste developer/rinse water.

3. Conclusion

As described, XL-T improved printing durability dramatically while generating a low level of industrial waste (i.e., waste developer) equivalent to that of conventional products. This is a CTP plate optimal for long run-length jobs such as the printing of forms, ledgers and magazines and, with it, baking is also possible.

Our lineup of eco-friendly, positive thermal CTPs, covering the commercial printing market overall, has thus been completed. With these products, we expect to contribute to the reduction of the environmental burden of the printing industries.

References

1) Aoshima, N.; Watanabe, T. Development of Environmentally Friendly Thermal CTP System "ECONEX". Fujifilm Research & Development No. 56, 16-19 (2011).
2) Kawauchi, I.; Nakamura, I. Function Enhancement of Double-coated Positive Thermal CTP Plate. Fujifilm Research & Development No. 51, 48-51 (2006).

Controlling a Software Development Process by Predicting the Effect of Improvements

Hachiro HONDA*, Masashi AISO**, and Keiichi SUZUKI*

Abstract

We have established a continuous quality improvement process by applying the Capability Maturity Model Integration (CMMI) method to our software development activities. The process consists of the following steps: (1) analyzing the key performance indicators of each development phase, (2) predicting the effect of improvements based on the analysis, and (3) monitoring and controlling the quality and cost. In upgrading from the CMMI level 4 to level 5, we focused on improvement of quality in the early development phases and achieved three times better quality in system tests.

1. Introduction

Fujifilm has been providing high-functionality, high-performance products in diverse fields including medical services with software playing an enabling role in these activities. In recent years, with the progress of IT innovation and the trend for larger and more complex software systems, software development capabilities have become even more important, requiring the improvement of software development management and quality control techniques.

Under such circumstances, to achieve an improvement of quality, cost and delivery (QCD), the Software Research & Development Center of FUJIFILM Corporation and FUJIFILM Software Co., Ltd. (hereinafter "we") have jointly been conducting software development process improvement activities based on the Capability Maturity Model Integration (CMMI) model[1] accepted worldwide.

In March, 2010, as an imaging unit development organization for X-ray image diagnosis systems (hereinafter the "medical console development organization"), we reached the CMMI Level 4 rating (hereinafter "L4") and published our achievement in a research and development report, *Introduction and Practice of Statistical Project Management Technique in Software Development*[2]. Now, we are announcing that we have reached the highest CMMI Level 5 rating (hereinafter "L5") by further improving our process management techniques.

Activities to improve our development processes from L4 to L5 included the following: data analysis of the organization; prediction of the effects of improvements; and the establishment of quality and cost monitoring/control techniques. In this paper, we will describe those activities in the light of improvement targets and the aim of improvement activities; our approach to process improvement activities; the confirmation of the effects of improvements; and the results of the acquired control techniques.

2. The improvement targets and the aim of improvement activities

We first clarified our improvement targets and the aim of improvement activities from business-oriented viewpoints and shared them within the organization.

(1) Process improvement targets from the viewpoint of business

In the past process improvement activities that brought us L4, we already reduced our development cost by more than 50%. In the latest improvement to acquire L5, focusing on making continuous process improvement take root throughout the organization, we set our target as the raising of productivity by 5% while improving work quality from L4.

(2) Our thought to cost reduction and the aim of improvement activities

Quality improvement and cost (workload) reduction are often regarded as contrary goals. However, the result of the statistical, organizational baseline analysis that we established to achieve L4 revealed that, by improving the quality of upper processes, corrective action workload can be reduced and this decreases overall cost. Therefore, in our improvement activities for L5, we targeted the improvement of the quality of upper processes.

Original paper (Received November 28, 2012)

* Software Research & Development Center
Research & Development Management Headquarters
FUJIFILM Corporation
Shin-yokohama, Kouhoku-ku, Yokohama, Kanagawa 222-0033, Japan

** Software Corporate Engineering Division
FUJIFILM Software Co., Ltd.
Shin-yokohama, Kouhoku-ku, Yokohama, Kanagawa 222-0033, Japan

3. Our approach to process improvement activities

To achieve our new target, *improving productivity by 5%*, we set our control target values for each process based on the organizational result data analysis and improvement prediction, and took action to improve all processes up to monitoring.

(1) Predicted values for improvements

i) Data analysis of the organization and extraction of improvements

All the projects of the medical console development organization involved in the current improvement activities were of product upgrades. Therefore, as the reference values for improvement analysis, we consulted the defects of the previous versions detected during system tests at the final test phase and those discovered on the market.

a) We created a fishbone diagram (i.e., Ishikawa diagram) for each project for the major factors of the above described defects and analyzed their root causes (Fig. 1).

b) We then created a tree chart from the root causes identified in a) and developed improvement plans. After assessing their effects and feasibility by giving them points, we selected several improvements to be executed from those having the highest scores (Fig. 2).

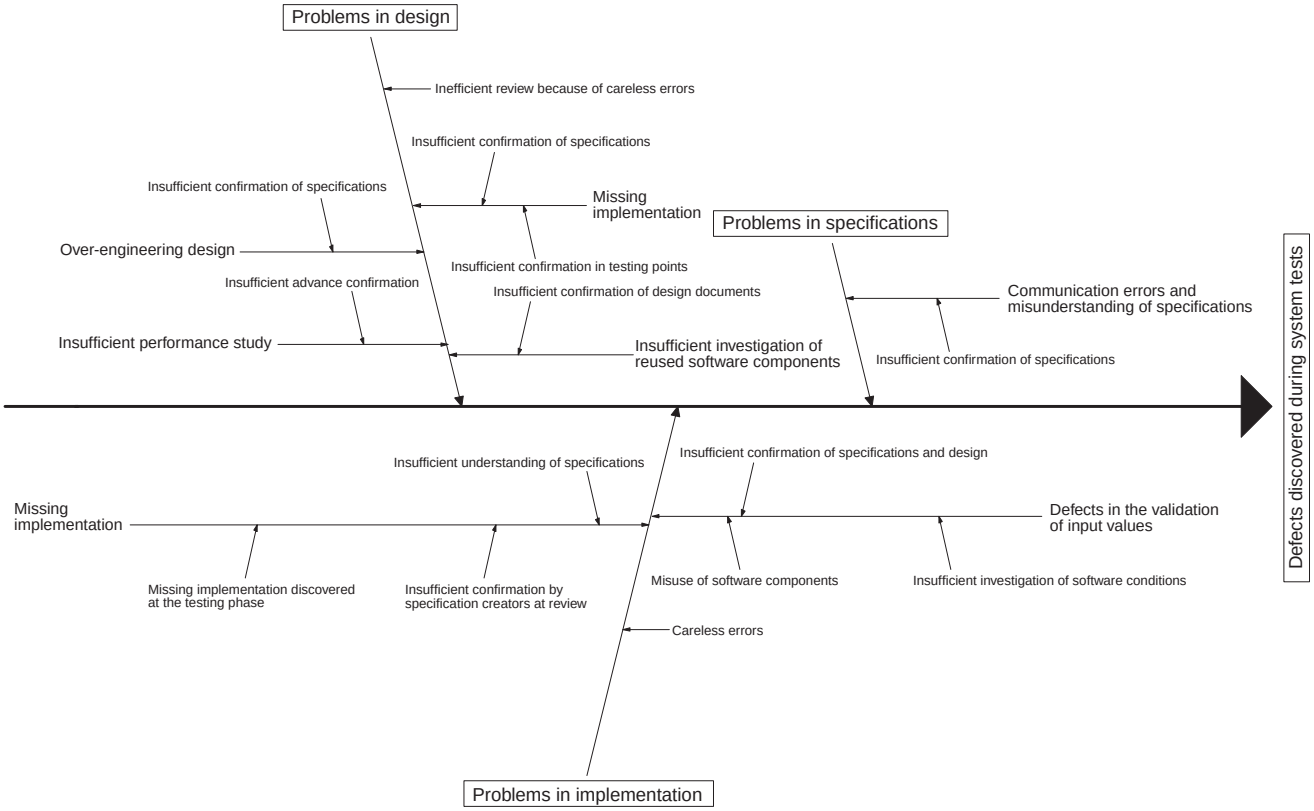

Fig. 1 Cause and effect diagram (fishbone diagram).

(◎ : 3 points, ○ : 2 points, △ : 1 point, × : 0 points)

Primary cause	Secondary cause	Tertiary cause	Effect	Feasibility	Score	Improvement No.	Why	What	Who	Where	When	Reference	Remark
Defects discovered during system tests	Problems in implementation	Defects in the validation of input values	Misuse of software components	○	△	3							
			Insufficient confirmation of specifications and design	△	△	2							
			Insufficient investigation of software conditions	△	△	2							
		Missing implementation	Insufficient confirmation by specification creators at review	○	△	3							
			Insufficient understanding of specifications	△	△	2							
			Missing implementation discovered at the testing phase	○	◎	5	1	Testing point incorporation	Test planner	In the test plan	At detailed design creation		Prevention of defects in system tests
		Careless errors		◎	○	5	2	Request of static analysis	Project leader	In the analysis division	In the middle and at the end of coding		Prevention of defects in system tests
	Problems in design	Insufficient investigation of reused software components	Insufficient confirmation of design documents	○	△	3							
		Insufficient performance study	Insufficient advance confirmation	○	○	4							
		Missing implementation	Insufficient confirmation of specifications	◎	△	4							
			Insufficient confirmation in testing points	○	◎	5	3	System testing points	Test planner	In the test plan	At system design creation		Prevention of defects in system tests
		Over-engineering design	Insufficient confirmation of specifications	△	△	2							
		Inefficient review because of careless errors		○	◎	5	4	Self review	All	At detailed design and coding	Before the team review		Self review
	Problems in specifications	Communication errors and misunderstanding of specifications	Insufficient confirmation of specifications	◎	○	5	5		Reviewer				Interactive document quality improvement

Fig. 2 Causes and countermeasures.

ii) Combination of improvements

The impact of each independent improvement may not be large. However, after summing up the individual effects of multiple improvements weighted in accordance with their scale, the total impact can be significant. According to that idea, we developed a tool to visualize the total impact of overall improvements for each process via an estimation based on the past statistical data (Table 1). The results given in the *Total %* row of the table revealed that, as we intended, defects in lower processes can be reduced by prior correction of those in upper processes.

Table 1 Degree of quality improvements.

Process	Process 1	Process 2	Process 3	Process 4	Process 5	Process 6
Improvement A	11%	11%	11%	-17%	-17%	-17%
Improvement B						-16%
Improvement C		6%			-6%	
Improvement D					-5%	-7%
Improvement E	-4%	-2%	-15%			
Total (%)	6%	15%	-4%	-17%	-28%	-39%

iii) Simplified prediction of impact achieved by improvements

Normally, a *t-test* is used to assess a mean difference. However, following its regular procedures every time requires a considerable length of time for verification. Therefore, we created another tool that enables the simple confirmation of the results of improvements (Table 2). With this tool, it is possible to predict instantaneously whether the results of the executed improvement are statistically significant.

Table 2 Simplified version of t-Test.

1. Mean difference(*t-test*)	
Significance level α	5%
Degrees of freedom φ	23
Pooled variance V	146.17
Statistic |t0|	2.77
t (φ, α)	2.07
|t0| $\geqq$ t (φ, α) ?	Yes (significantly different)

iv) Predicted values employed

To verify, in advance, whether the overall results of multiple improvements can reach the targets of the organizational process improvement activities and whether the impact is significantly different, we repeated steps ii) and iii) above and employed the final improvement plans. Table 3 shows, as an index for the improvement of the quality of software, the target defect density (the number of defects per thousand lines of code [i.e., kloc]) in system tests for L5 set based on the results for L4.

Table 3 Estimation of expected improvements in quality.

Target process	System test
Improvement target for defect density	-48% from L4

Similarly, Table 4 shows the target total corrective action workload (hours per kloc) from system design to system test.

Table 4 Estimation of expected improvements in performance.

	Total corrective action workload from system design to system test
Improvement target for total corrective action workload	-46% from L4

(2) Monitoring of the impact of improvements

Results data were monitored as described in i) to iii) below to check whether they would remain within the predicted control range. Methods i) and ii) were developed for L4 and iii) was newly added for L5.

i) In-process quality monitoring in each project

In each project, defect verification was conducted for all processes from system design respectively by subsystem (Fig. 3). In monitoring, if any results deviate from the predicted control range, the cause was identified and corrective measures were taken. In the current development by the medical console development organization, however, monitoring results were stable without any deviation other than falling below the lower limit observed in some components reused from existing software. Therefore, no corrective measures or resetting of the target values was necessary.

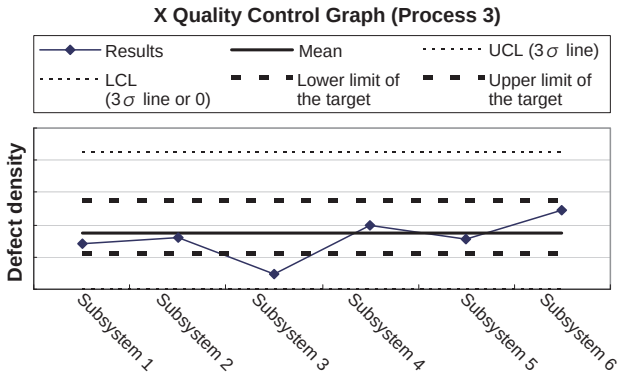

Fig. 3 Quality control graph in a process.

ii) Monitoring of total quality with a prediction model

In all processes of each project, cumulative defects were monitored with the dedicated prediction model to check whether they would remain within the control range (Table 5). By doing so, the quality targets can be reviewed when deviation is predicted. In the current development, monitoring results were stable with no deviation from the control range. Therefore, no resetting of the prediction model was necessary.

Table 5 Quality monitoring by our prediction model.

Applied model to processes	Process of the prediction model	Constant term	Process 1	Process 2	Process 3	Process 4	Process 5	Process 6	Total (number of defects/ kloc)	Upper limit of the prediction interval (70%)	Lower limit of the prediction interval (70%)
Process 2	Final										
Process 3	Final										
Process 4	Final										
Process 5	Final										

iii) Monitoring of results data for organizational improvement impact

We verified, weekly, the changes in result data for the quality and productivity (total corrective action workload) of the overall medical console development organization. With a tool developed for this monitoring, by entering the quality data of each subsystem of the involved multiple projects, it is possible to confirm whether the organizational target values remain within the control range (Fig. 4).

4. Verification of the impact of improvements

After completing development in all projects, we verified the results of activities described in *3. Our approach to process improvement activities.*

(1) Verification of the impact of quality improvements

Table 6 shows the actual results for the prediction of quality improvement. In the system test process that requires more workload for correction than others, defect density decreased by 69% on average from that of L4 and it was confirmed that quality was significantly improved. The standard deviation for L5 was 0.35 of the value for L4 and the stability was thus improved. This is because the number of defects detected in system tests greatly decreased as a result of various improvement activities.

In addition, we conducted a *t-test* to assess defect density in system tests for both L4 and L5 and found the significance level was 5%. Improved quality was thus proved statistically, too (Fig. 5).

(2) Confirmation of the impact of improvements on total corrective action workload

Table 7 shows the actual results for the prediction of total corrective action workload. The quality of upper processes was increased and corrective action workload in system tests was decreased by reforming the software structure as one of those improvements. As a result, the total corrective action workload (i.e., the summation of the products of defect density and the number of hours required for correction in all processes from system design) was reduced from L4 by 62% on average and the impact of improvements was confirmed. Because the predicted values were an estimation of the minimum possible impact, the actual results turned out to be better than expected. The standard deviation for L5 was 0.84 of the value for L4 and the stability was thus improved. This is because, as a result of improvement activities, the time spent on analysis became shorter and more stable.

In addition, we conducted a *t-test* to assess total corrective action workload and found the significance level was 5%. Improved productivity (corrective action workload) was thus proved statistically, too (Fig. 6).

(3) Impact on business

The results of those improvement and monitoring activities reveal that development workload was reduced by

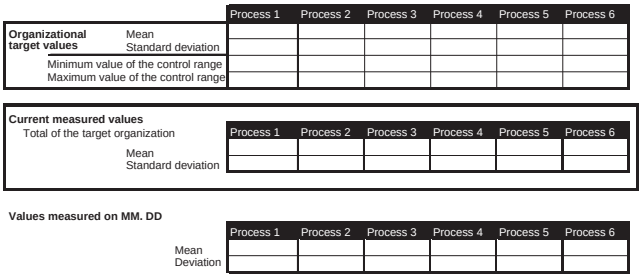

Fig. 4 Weekly monitoring of the organization's target.

Table 6 Results of quality improvements.

Target process	System test	Reference
Improvement target for defect density	-48% from L4	Standard deviation ratio 1 → 0.35
Results of improvement achieved in defect density	-69% from L4	

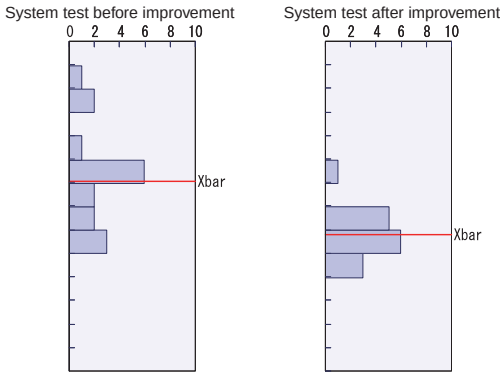

Fig. 5 t-test for quality improvements.

Table 7 Results of performance improvements.

	Total corrective action workload from system design to system test	Reference
Improvement target for total corrective action workload	-46% from L4	Standard deviation ratio 1 → 0.84
Results of improvement achieved in total corrective action workload	-62% from L4	

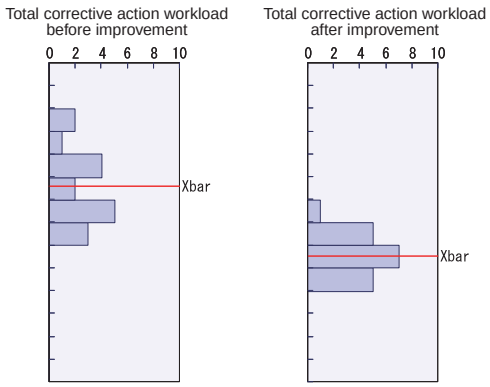

Fig. 6 t-test for performance improvements.

6% on average (Fig. 7), which exceeded the 5% set as the improvement target for productivity. Thus, the activities contributed to the reduction of development cost.

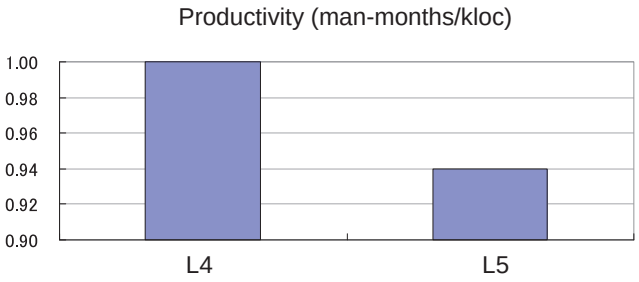

Fig. 7 Productivity improvements from CMMI-L4 to L5.

In defect density, quality at system test for L5 increased to three times that for L4 (Fig. 8).

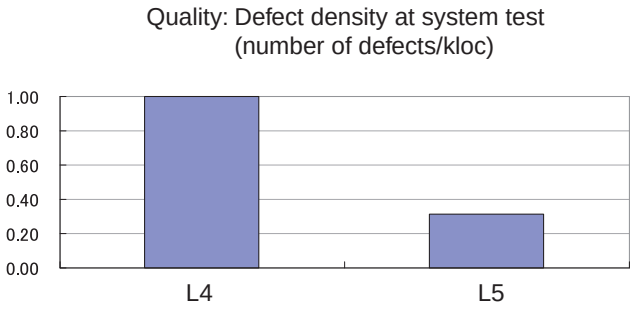

Fig. 8 Quality improvements from CMMI-L4 to L5.

5. Control techniques acquired via improvement activities

Via process improvement activities after receiving L4, we have established the following new control techniques covering prediction to monitoring.

- ○ Techniques for the prediction of the impact of improvements
  - • A technique for the prediction of the total impact of multiple improvements was established.
  - • A technique for the advance prediction of statistical impact on quality and productivity was established.
- ○ A control technique that allows the control of activities from the setting of overall organizational targets to their monitoring.

6. Conclusion

Since 2002, based on the CMMI models, we have been carrying out software development process improvement activities. On this occasion, we further introduced the high maturity models to the medical console development organization, via which we have established a control technique that enables a sequence of activities including organizational data analysis, comprehensive prediction of the total impact of multiple improvements and monitoring of quality and cost.

In official CMMI appraisal in December, 2011, we reached the highest Level 5 rating (optimizing stage) of its Version 1.3. In the meantime, we were also able to contribute to the reduction of development cost by achieving the target set for the improvement of productivity.

Our improvement activities are still in progress. In the future, we will apply the know-how and systems that brought L5 to the medical console development organization to improve software development processes company-wide and thereby increase the level of all our development organizations.

References

1) Software Engineering Institute of Carnegie Mellon University. CMMI for Development, Version 1.3 (2010).
2) Aiso, M.; et al. Introduction and Practice of Statistical Project Management Technique in Software Development. Fujifilm Research & Development No. 56, 31-34 (2011).

("CMMI" referred to in this paper is a registered trademark of Carnegie Mellon University, U.S.A. That is an index developed by the Software Engineering Institute of the university to rate the process maturity of development organizations into five levels.)

Development of Image Processing Technologies Used for Creation of Digital Comics and Their Application

Shunichiro NONAKA*, Hajime TERAYOKO*, Tetsuya SAWANO*, and Norihisa HANEDA*

Abstract

We have developed image processing technologies for digital comics (e-comic) creation and distribution. In this paper, we introduce "GT-Smartone" (moiré-less image resizing technology), "GT-ComicEncoder" (highly efficient comic image compression technology), "GT-Balloon" (automatic speech balloon detection technology) and "GT-Translate" (automatic digital comic translation technology).

1. Introduction

In recent years, electronic books have been attracting much attention. Under such circumstances, by fully utilizing its accumulated image processing technology, Fujifilm has developed new technologies for comic e-books, or e-comics, in which images are particularly important, and promoted business in that domain, providing products and services including software incorporating those technologies to enable the effective production and browsing of e-comic contents.

As shown in Fig. 1, image processing technology for e-comics is classified into two fields: component technologies and applied technologies that utilize the former. Component technologies consist of an image analysis function such as "GT-Scan" [1] to enable automatic frame detection and an image conversion function to create high-quality image data from originals used for electronic books.

This paper describes component technologies in section 2 and, in section 3, applied technologies, which are an advanced version of the former. Finally, section 4 provides a conclusion and discussion of future issues.

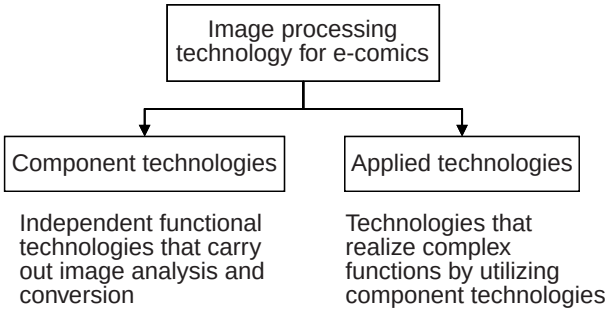

Fig. 1 Image processing technologies used for e-comics.

2. Development of component technologies for e-comics

As shown in Fig. 2, component technologies for image processing in e-comics are divided into two pillars: an image analysis function and image conversion function. As a former technology, Fujifilm developed GT-Scan for automatic frame detection[1]. It has been incorporated into one of our products, "GT-EpubAuthor for Fixed Layout" [2] and utilized on various occasions in the production and distribution of electronic books.

This section first describes two image conversion functions: GT-Smartone for moiré-less image resizing in section 2.1 and GT-ComicEncoder for highly efficient comic image compression in section 2.2. Finally, an image analysis function, GT-Balloon for automatic balloon detection is described in section 2.3.

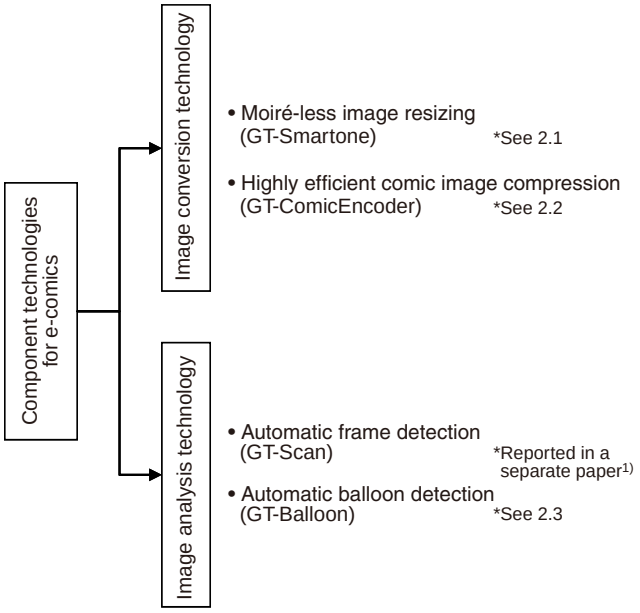

Fig. 2 Component technologies for e-comics.

Original paper (Received December 25, 2012)
* Internet Business Development Division
FUJIFILM Corporation
Akasaka, Minato-ku, Tokyo 107-0052, Japan

2.1 Development of moiré-less image resizing technology, GT-Smartone

To shade comic images, a halftone technique such as screentone is often used. However, in the production and provision of e-comics, some of the image processing processes, such as digitizing, authoring and display, require resizing, which causes an image degradation effect called moiré to the area where halftone is applied (Fig. 3).

There are various printing technologies to reduce the occurrence of moiré[3]. However, in the case of e-comics, a number of difficulties prevented the establishment of optimal solutions for it:

- Variation in the resolution of input originals, in-process images and final images presented for browsing is considerable.
- In the process of digitizing, images may undergo formatting so that they have different attributes, such as being changed from colored to monochrome or from binary to multi-tone.
- Normally, the resizing methods used for browsing devices are generic and cannot prevent the occurrence of moiré.
- In general, comic images which contain a large number of edges are expected to remain sharp. Reducing moiré while ensuring sharpness is naturally difficult.

In particular, reducing moiré that occurs in resizing is the most significant issue in the production of e-comics. With this background, we started the development of moiré-less image resizing technology for e-comics by utilizing our expertise accumulated in the field of image processing for over a long period of time. The new technology is expected to achieve the following:

- Robustness in various image processing stages including I/O
- Minimal computation requirements targeting the future incorporation into browsing devices
- Optimal balancing of the trade-off between moiré-less shading and the retention of sharpness

We first carried out a thorough analysis on the statistical properties of halftone used for e-comics, then reviewed the properties of browsing devices, and finally succeeded in the design and development of a resizing technology optimal for e-comics, GT-Smartone, that enables moiré-less shading and the retention of sharpness with minimal computation.

Fig. 4 shows the comparative images resized with GT-Smartone and with photo-retouching software most commonly used in the production process of electronic books. As shown, the image processed with GT-Smartone has a smoother texture with moiré reduced.

We are now planning to incorporate this technology into one of our e-comic image conversion system products, “GT-Quality” [4], and also considering its expansion to smartphone handsets, tablets and e-book readers.

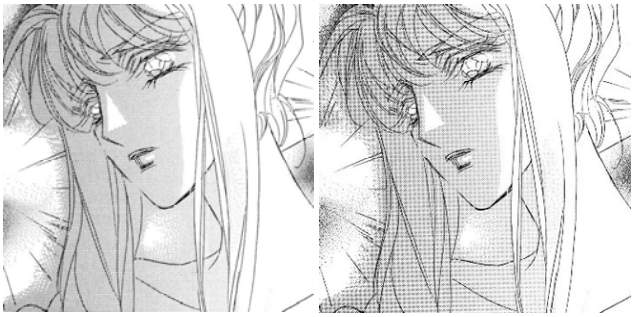

(a) Original image (b) Resulting image with moiré

Fig. 3 Sample of moiré.

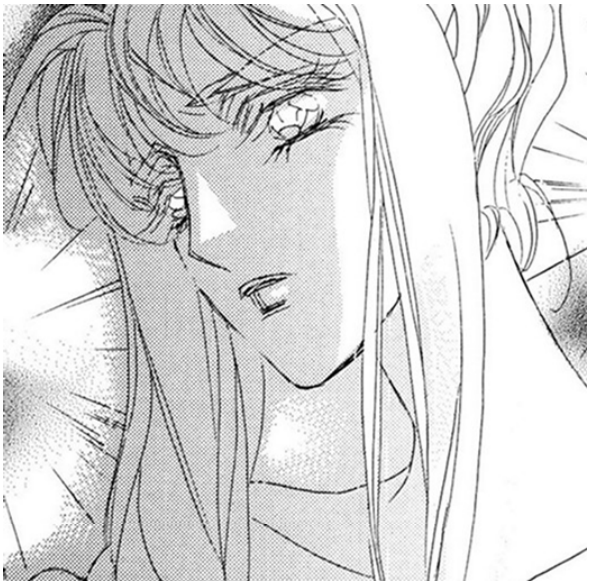

(a) Result with GT-Smartone

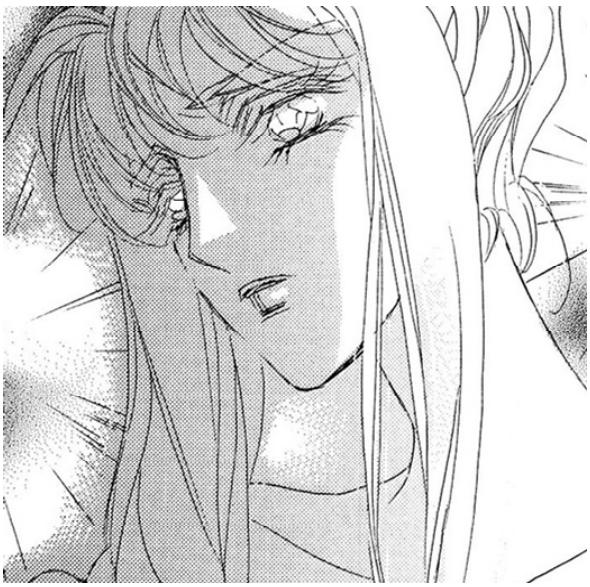

(b) Result with popular tool

Fig. 4 Effectiveness of GT-Smartone.

2.2 Development of highly efficient image compression technology, GT-ComicEncoder

Usually, e-comics are distributed via the Internet and stored in browsing devices. Therefore, it is required to achieve high resolution images with the minimum possible data size. In most cases, e-comics are provided as a collection of image data, compressed in the JPEG format[5]. However, the JPEG compression algorithm was originally designed for photos and cannot achieve sufficient performance for the compression of comic images whose data characteristics are so different from photos.

To respond to that issue, we analyzed the statistical and visual properties of a massive quantity of scanned comic images and, based on the results, developed GT-ComicEncoder, an encoder to generate compressed JPEG data, which can be decompressed with general JPEG viewers, while optimizing comic images.

Fig. 5 shows the comparison of sizes and quality (mean square error) between image files compressed with GT-ComicEncoder and with common photo-retouching software. As shown, the former achieved a 5% to 15% size reduction compared with the latter when the quality level was the same.

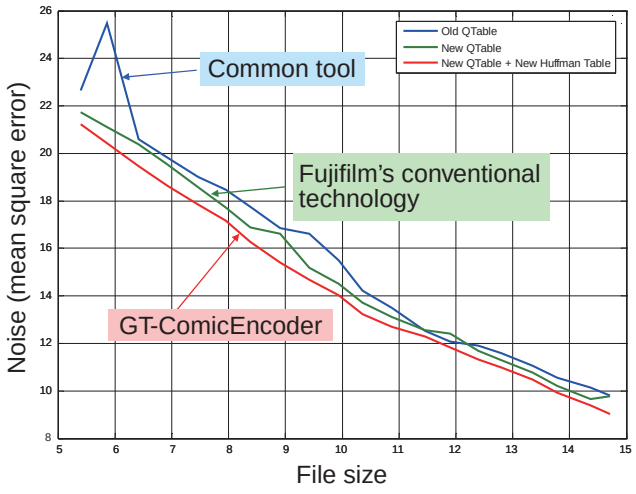

Fig. 5 Effectiveness of GT-ComicEncoder.

We have already incorporated this technology into our e-comic image conversion system, GT-Quality. The product has established high popularity among the users.

2.3 Development of automatic balloon detection technology, GT-Balloon

To dramatically reduce the manpower required for manual frame data allocation in the production of e-comics, we developed and made available to the public an automatic frame detection technology, GT-Scan[1].

Since then, we have received the following requests for new functions from many creators who utilize GT-Scan in various processes:

- A function to extract not only frames but also a variety of objects deployed in pages and frames via image analysis
- A function to extract balloon areas, in preference to anything, for the realization of processes in high demand such as translation, text information extraction and processing of text areas whose properties are different from image areas by applying different parameters

This encouraged us to develop GT-Balloon, an automatic balloon detection technology using image analysis.

Having sampled various balloon images from comics and classified their characteristics such as shapes and contents, we created trial algorithms to detect balloon areas automatically and, via optimization of those algorithms and parameters with a large quantity of sample data, completed the final version.

Fig. 6 shows the processing result with GT-Balloon. As shown, it performed automatic balloon detection precisely via image analysis.

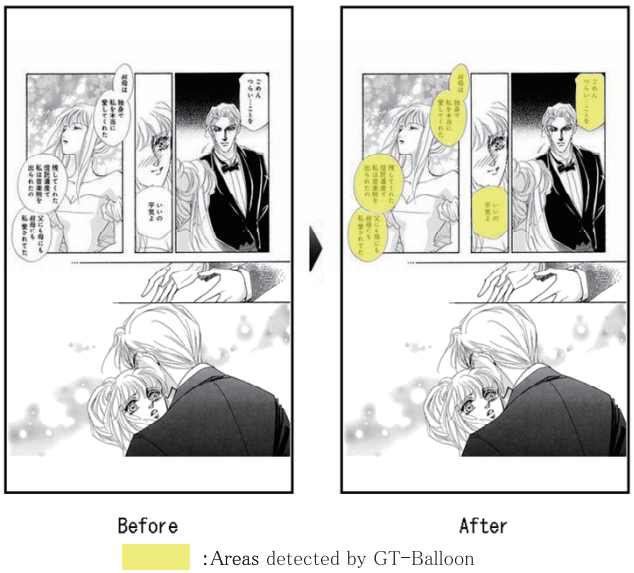

Fig. 6 Result of processing by GT-Balloon.

GT-Balloon is available for diverse uses such as translation, text data extraction and image quality improvement. In section 3, we will introduce its application to automatic translation.

3. Development of applied technology for e-comics

Automatic translation system GT-Translate

3.1 Background of the development

We intend to develop the component technologies described in the previous section into applied technology to

create new benefits by not only using them independently but also combining them dynamically.

For example, we considered the realization of a system to dynamically translate Japanese comics that are read worldwide into local languages based on the automatic balloon detection technology GT-Balloon.

3.2 Automatic translation system for e-comics, GT-Translate

We developed an automatic, real-time translation system for e-comics, GT-Translate, by using component technologies such as GT-Balloon in combination with other conventional technologies.

• User's operational sequence

The system operates upon the following actions by users.

(1) Original e-comic image display

To display original e-comics on the comic viewer of smartphones

(2) Translation request

To select a target language from among the language list and execute translation

(3) Response image display

To display text translated into the target language over the original text inside the balloons

• System configuration

GT-Translate is a client-server system consisting of two elements: the GT-Translate client for users to execute the translate request and display the translated results; and the GT-Translate server to perform the actual translation process (Fig. 7).

• Internal process flow

The system carries out the following processes internally.

(1) Translation request

Upon user action, the viewer of the GT-Translate client sends a translation request to the GT-Translate server, specifying the target language.

(2) Analysis-use image generation

The GT-Translate server receives comic images targeted for translation and converts them into analysis-use images. By combining multiple component technologies for image conversion, the server resizes the images to an optimal size that allows high-speed processing without reducing analysis accuracy.

(3) Balloon detection

The server then performs the detection of balloons contained in the analysis-use images with GT-Balloon. During this process, the positions of the rectangular text areas inside balloons are detected together with the positions of balloons.

(4) Balloon text extraction

With an OCR, the server extracts strings (balloon text) to be translated from inside the detected balloon images.

(5) Balloon text translation

The server executes the translation of balloon text into the specified target language while communicating with existing web translation services.

(6) Translated balloon image generation

The server generates, for each balloon, an image (translated balloon image) over which to display the translated text, controlling line feed and the text size based on the width of each balloon area.

(7) Translated page image composing

The server composes all the translated balloon images within a page and generates a translated page image that can directly overlay the original comic page image. After completing processes from (2) to (7), the server returns the result (translated page image) to the GT-Translate client.

(8) Translated page overlay display

The GT-Translate client receives the translated page image from the GT-Translate server and displays it so that it overlays the original comic page image. In that way, translated text overrides the original text inside the balloons.

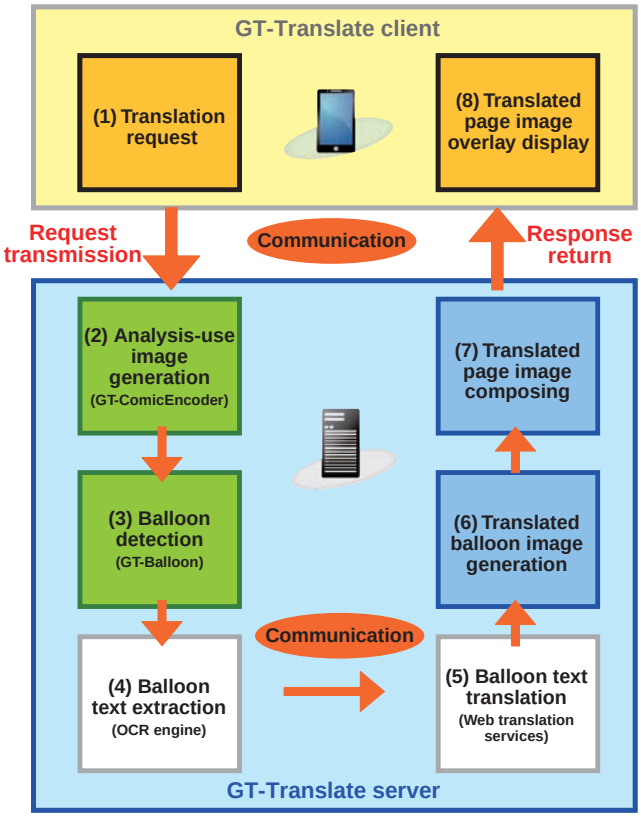

Fig. 7 GT-Translate system configuration diagram.

Via the above steps, the GT-Translate system achieves real-time, automatic translation for e-comics (Fig. 8).

Before: In Japanese

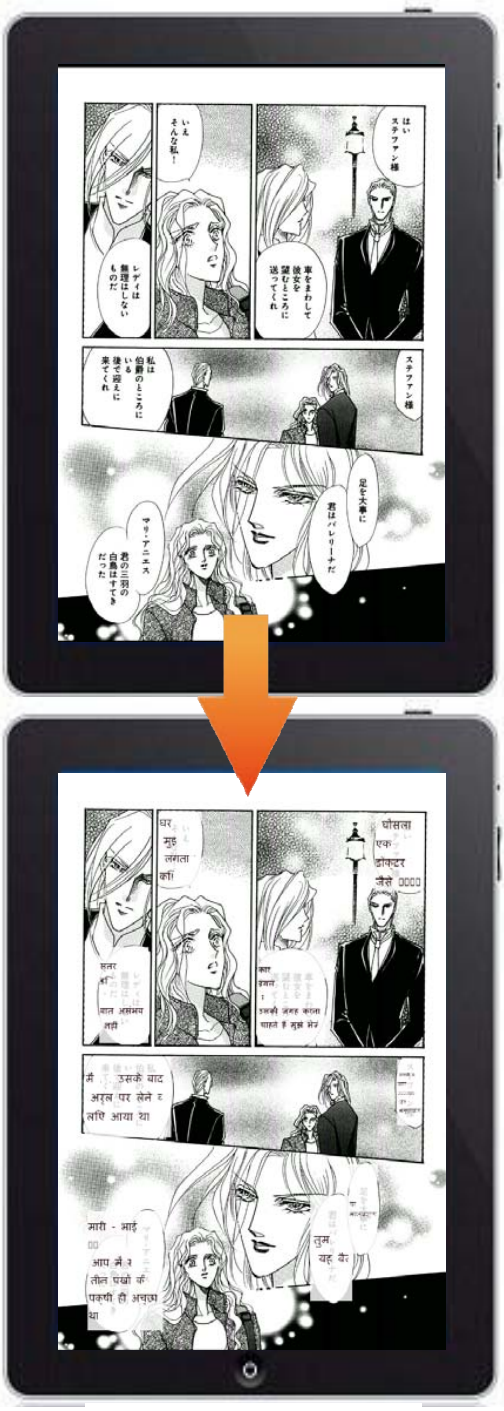

After: Translated into Hindi

Fig. 8 Result of processing by GT-Translate.

3.3 Achievements and issues

So far, GT-Translate has succeeded in providing the exciting user experience of reading balloon text that has been translated automatically into a selected language while browsing e-comics on a mobile device. The system realized it not by using ready-made translations but dynamically translated text via image processing technology. In that sense, it can be said that we have achieved some of the target results.

However, the current translation accuracy, which is the most important, is not at all satisfactory. The following practical issues are revealed.

- Balloon text mostly consists of colloquial speech. This is, by its nature, not suitable for machine translation.
- In many cases, the speech lacks context, instead relying for its meaning on information provided by the images. This also prevents accurate translation.

GT-Translate needs more time to solve the above described issues and thereby achieve a practical level of accuracy for a real-time, automatic translation system for e-comics.

On the other hand, it has reached a sufficient level for practical application in the following tasks not related to translation accuracy: detection of text areas inside balloons; the whitewash of the detected text areas; and re-deployment of translated text in text areas inside balloons.

With all those matters in mind, we shifted our initial target to the simplified creation of translated e-comics. For the time being, we will accumulate expertise in this domain while positioning the technology as a computer-assisted translation tool and improve it steadily for the future to achieve a genuine, real-time automatic translation system for e-comics.

4. Conclusion

To solve various issues observed in the production, distribution and browsing of e-comics, we have engaged in the development of two component technologies: an image analysis function to automatically detect the coordinates of image elements such as frames and balloons; and an image conversion function to generate images that keep the best balance between quality and data size.

We have then incorporated those technologies into a variety of software products such as electronic book authoring tools and e-comic image conversion systems. Now, they are all highly regarded in the market.

In addition, by combining component technologies, we developed an automatic translation system for e-comics as an applied technology that provides new benefits for users. While undertaking that activity, we investigated some of the technological issues that will need to be tackled for the anticipated worldwide expansion of e-comics.

In the future, in addition to further improving the two pillars of our component technologies, image analysis and image conversion, as well as combining them dynamically, we intend to continue the development of worthwhile applied technology. Those endeavors will enable us to introduce, onto the market, solutions that offer stress-free production, distribution and browsing environments for e-comic products.

We aim to contribute to the further development and promotion of electronic books by applying and extending our technologies widely to all fixed-layout electronic books that contain images, including e-comics. We will strive to bring technological benefits to the public by truly useful digital conversion of paper publications.

References

1) Nonaka, S.; et al. Development of “GT-Scan”, the Technology for Automatic Detection of Frames in Scanned Comic. Fujifilm Research & Development No. 57, 46-49 (2012).
2) Fujifilm News Release 2012-12-17. http://www.fujifilm.co.jp/corporate/news/articleffnr_0726.html
3) Inoue, Y. The Image Quality of the New Digital Screen Technology. Journal of the Japanese Society of Printing Science and Technology. **38** (6), 30-34 (2001).
4) Fujifilm News Release 2012-4-2. http://fujifilm.jp/information/articlead_0154.html
5) ISO/IEC 10918-1:1994. Information Technology - Digital compression and coding of continuous - tone still images: Requirement and guidelines.

* Prince ha Koi wo Utau (The Prince is Singing His Love.) ©HARUMO SANAZAKI 2009/ OHZORA PUBLISHING Co. (Fig. 3, Fig. 4, Fig. 6, Fig. 8)

Development of Thermoplastic Nanocomposite Optical Materials

Tatsuhiko OBAYASHI*, Ryo SUZUKI**, Hiroaki MOCHIZUKI*, and Yasuhiro AIKI*

Abstract

Thermoplastic nanocomposite optical materials that include ZrO_2 nanoparticles in high concentration have been developed. Even after undergoing the melt-molding processing, homogeneous dispersion of nanoparticles in the resin was maintained and the molded articles showed good transparency. The refractive index of the resin rose from 1.59 to 1.65 by the addition of 12.5 vol% ZrO_2 nanoparticles. It was found that the kinds and number of functional groups in polymer, the length of linkers between the functional groups and the main chain of the polymer were very important to achieve the homogeneous dispersion of particles and the moldability of the nanocomposite. This material was molded into convex and concave lenses.

1. Introduction

The refractive index is one of the most important fundamental properties of optical components such as lenses. Refractive index control is an essential technique for processing light by manipulating its speed and passage, and materials studies for pursuit of high/low refractive index, Abbe's number (wavelength dependence of the refractive index) control and birefringence (anisotropy of the refractive index) control, etc. have actively been continued.

Lenses made of materials with a high refractive index can refract the passage of light more significantly with a small curvature, which enables making thinner lenses with higher resolution.

Conventionally, the use of inorganic materials, such as glass and ceramics, has been dominant in optical components because they have a wider controllable refractive index range. In recent years, however, needs for lighter and less expensive materials have increased, so that replacement of inorganic materials with resins in various applications has been expedited. On the other hand, resins have a disadvantage of narrower controllable refractive index ranges when compared with inorganic materials, hindering their use in many applications.

To increase the refractive index of materials, it is necessary to increase polarizability or density. In that regard, resins have a critical weakness, as increasing their density is more difficult than that of inorganic materials.

A general way to increase the refractive index of a resin is to design molecules so that its polarizability is increased by introducing halogens (Cl, Br and I), sulfur, heavy metal atoms and aromatic rings[1), 2)]. However, applying such methods elongates absorption wavelength, which limits the design of transparent materials. In addition, it needs caution because there is correlation with other issues such as the decrease of resistance to stain by oxidative degradation and the increase of water absorbency.

Resins alone cannot achieve the intended refractive index. Therefore, another means has been investigated, in which inorganic materials with a high refractive index are compounded with resins[3) to 6)]. As shown in Table 1, compared with organic materials, inorganic materials are known to cover a wider range of refractive indexes. Some materials, such as ZrO_2 and TiO_2, are transparent in the visible range while achieving very high refractive indexes.

Table 1 Refractive index at 589nm of typical optical materials.

Typical optical resin materials	Refractive index	Transparent inorganic materials	Refractive index
Amorphous fluoropolymer	1.34	TiO_2 (Rutile)	2.72
PMMA	1.49	TiO_2 (Anatase)	2.52
COP	1.53	Diamond	2.42
Polystyrene	1.59	ZrO_2	2.10
Optical polycarbonate	1.59 to 1.63	Al_2O_3	1.62
Fluorene-based polyester	1.60 to 1.64	SiO_2	1.45
Polyethersulfone	1.64	MgF_2	1.37

It is easily predictable that the refractive index of composites can be controlled by the volume fraction of additional inorganic particles. Organic-inorganic composite technology has already been used widely for thin films such as anti-reflection coatings.

However, there is an issue when applying this technology into thick molded materials such as lenses. The difference in refractive index between resins and high-refractive index

Original paper (Received December 11, 2012)

* Synthetic Organic Chemistry Laboratories
Research & Development Management Headquarters
FUJIFILM Corporation
Nakanuma, Minamiashigara, Kanagawa 250-0193, Japan

** Flat Panel Display Materials Research Laboratories
Research & Development Management Headquarters
FUJIFILM Corporation
Nakanuma, Minamiashigara, Kanagawa 250-0193, Japan

inorganic particles is significant, and the consequent light scattering greatly affects the transparency of the lenses. It is difficult to realize a high refractive index compatible with high transparency.

To apply cost-effective molding methods, resins need to be melted, flowed and solidified without using solvents, which is also difficult because of the decrease in fluidity originating from particle interaction and because of particle aggregation during the melting process. To achieve the required refractive index while maintaining high transparency, it is necessary to disperse small particles homogeneously at a high concentration. However, when that is done, melt-moldability is generally impaired. There is a strong need for thermoplastic nanocomposite materials with a high refractive index but, as far as we know, such a highly demanding technology has not yet been realized at a practical level.

This paper describes thermoplastic nanocomposite optical materials that we have developed aiming at realization of a high refractive index compatible with melt-moldability by using organic-inorganic composites.

2. Thermoplastic nanocomposite optical materials

2.1 Simulation

If ZrO_2 nanoparticles (refractive index: 2.10) are dispersed homogeneously into a resin (refractive index: 1.60), the refractive index of the composite is expected to change with the volume fraction of the nanoparticles as shown in Fig. 1.

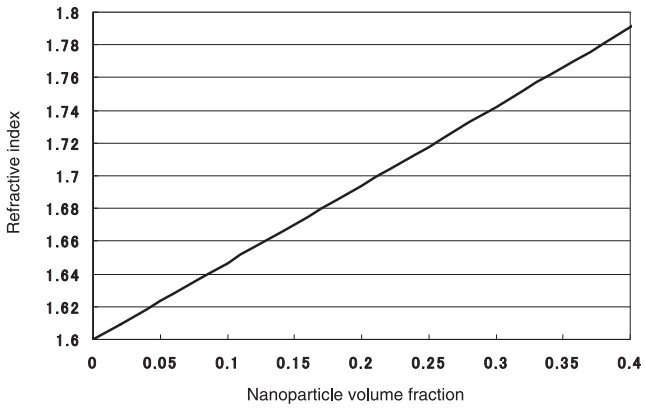

Fig. 1 Refractive index of the nanocomposite calculated according to the volume fraction of the nanoparticle.

According to the calculation, to achieve nanocomposites with a refractive index of 1.70, 21.2 vol% ZrO_2 nanoparticles need to be added. Fig. 2 shows the simulation results for the relationship between nanoparticle diameters and transparency when the thickness of the molded material is 1 mm.

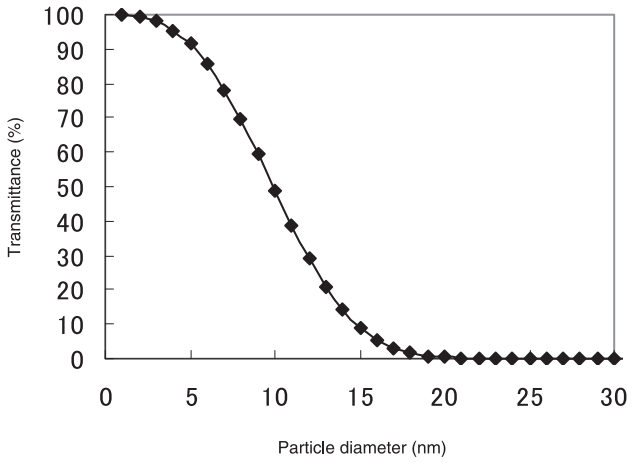

Fig. 2 Transparency of the nanocomposite calculated as a function of the particle diameter.

To achieve a high internal light transmittance of at least 90%, nanoparticles whose average diameter is not larger than 5 nm should be dispersed evenly without aggregation. It was predicted that, with increase in the diameter of particles, transparency would decline sharply.

If, in a nanocomposite, nanoparticles with a diameter of 5 nm are positioned at the vertices of the hexagonal closest packed structure and dispersed homogeneously in resin at a concentration of 10 vol% and 20 vol%, the distance between particles is expected to be 4.7 nm and 2.7 nm, respectively (Fig. 3). Nanoparticles can easily aggregate because their specific surface area is particularly large compared with bulk materials. Therefore, it is very difficult to achieve homogeneous dispersion at a high concentration.

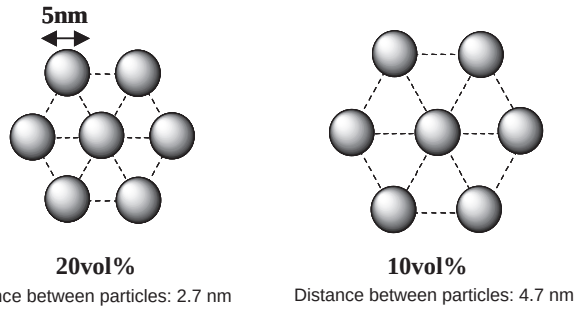

Fig. 3 Distance between particles expected in the nanocomposite : particle diameter, 5nm ; particle amount, 20vol% (left)/ 10vol% (right).

As a first step, aiming to develop a thermoplastic nanocomposite material in which zirconia nanoparticles of 5 nm in diameter are dispersed homogeneously at a concentration between 10 vol% and 20 vol%, we designed a nanoparticle dispersion resin.

2.2 Design of a nanoparticle dispersion resin

2.2.1 Nanoparticle dispersion into thermoplastic resin

We first considered a simple method of dispersing ZrO_2 nanoparticles throughout a thermoplastic resin such as PMMA or PS after modifying their surface with dispersants. However, with that method, homogeneous dispersion was difficult, and cloudiness by the aggregation of nanoparticles could not be prevented.

Fig. 4 shows the result of a trial for dispersion in which 10 vol% zirconia nanoparticles with a diameter of 5 nm were added to PMMA after their surface was treated with a phosphoric acid surface modifier. The composite became cloudy and the nanoparticles were found to have formed aggregates on the order of tens of micrometers. It is likely that insufficient interaction between the nanoparticles and resin has caused the aggregation of nanoparticles, their phase separation from the resin, and consequent cloudiness (Fig. 5).

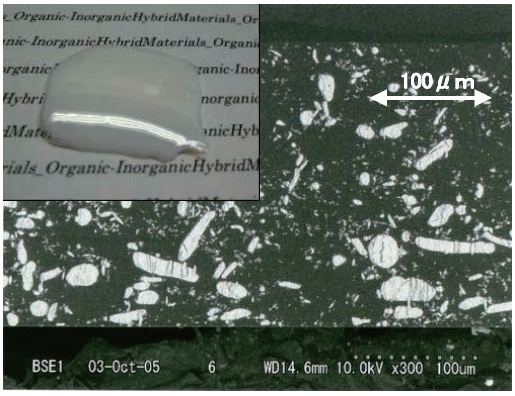

Fig. 4 TEM image (x300) of a cloudy nanocomposite section.

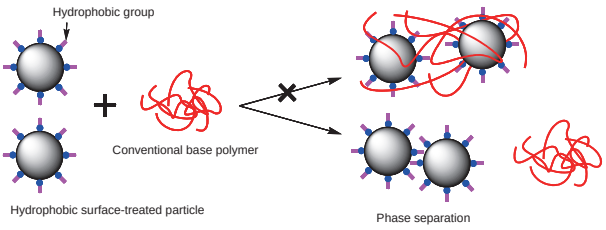

Fig. 5 Cohesion of particles in a cloudy nanocomposite.

To enable homogeneous dispersion, stronger interaction between matrix polymers and nanoparticles seems to be essential. However, it is easily predictable that random, multisite interaction between nanoparticles and resin may form physical gels that impair plasticity and fluidity.

2.2.2 Resin with single-ended anchoring groups

We believed the ideal system to be nanoparticle grafting with single-ended adsorptive resin as shown in Fig. 6. That is not a process of mixing nanoparticles and resin but of uniting them into one polymeric material. If this system is realized, the aggregation or phase separation of nanoparticles will be minimized because they are coated with resin. Also, the structure, having the anchoring group at only a single end, is expected to reduce the possibility of gelation caused by resin bridging multiple particles.

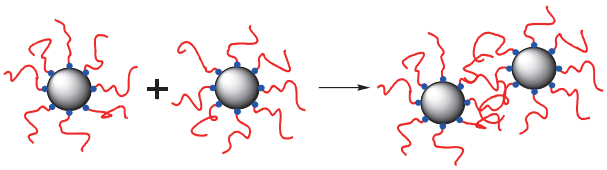

Fig. 6 Ideal thermoplastic nanocomposite.

According to this concept, we developed a dispersion resin with polystyrene (refractive index: 1.59) as its main backbone and explored the creation of a composite by using zirconia nanoparticles with a particle diameter of up to 5 nm.

For anchoring groups, we selected the phosphonic acid group and the carboxylic acid group that have strong interactions with metal oxides. By applying atom transfer radical polymerization (ATRP)[7), 8)], we synthesized (A) a block copolymer that has more than one anchoring group at the single end and (B) a resin that has only one, strong anchoring group introduced to a single end (Fig. 7).

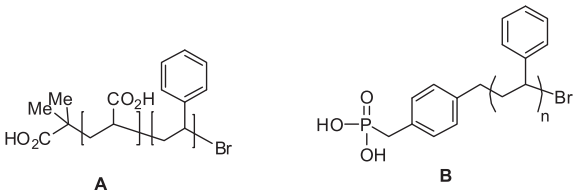

Fig. 7 Polymer design suitable for particle dispersion.

After adding an auxiliary dispersant, a plasticizer and the above described resins to the dimethylacetamide solution containing zirconia nanoparticles with a diameter of 5 nm and mixing them until they became homogeneous, we distilled the solvent and pressed the white composite powder thus gained (containing 41.7 wt% ZrO_2) at 180°C. As a result, we obtained transparent specimens with a thickness of about 1.5 mm. The observation of those specimens with a transmission electron microscope (TEM) revealed that both of them exhibited good nanoparticle dispersion. Fig. 8 shows the condition of a specimen created from Polymer A.

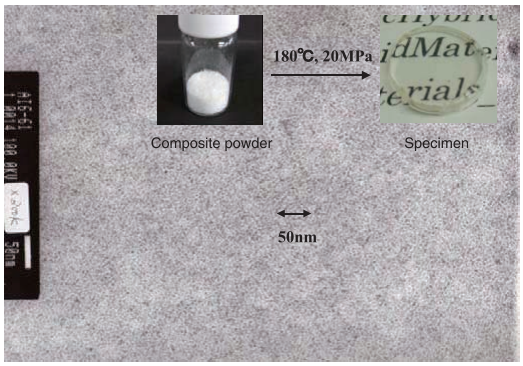

Fig. 8 TEM image (x300) of a section of the transparent nanocomposite using Polymer A.

2.2.3 Random copolymer

It became clear that gelation-free, homogeneously dispersed thermoplastic nanocomposite materials can be realized by introducing functional groups for adsorption to a single end of polymer using ATRP. However, in practice, it is more preferable to achieve it with less expensive random copolymers.

Therefore, we next investigated the detailed properties of random copolymers including the kinds of possible functional groups for adsorption, dosages, gelation behavior under multisite adsorption, nanoparticle dispersibility (transparency) and their relationships. As a result, it was confirmed that, by precise molecule design, random copolymers, too, can achieve homogeneous nanoparticle dispersion (high transparency) without causing gelation (insolubilization/infusibilization).

The optimal dosage of functional groups for adsorption depends on the strength of their adsorption power. Insufficient dosage causes the aggregation of nanoparticles, and excessive dosage leads to gelation. It is preferable and more usable if the functional groups have a wider range in the optimal number introduced per polymer. In the case of ZrO_2 nanoparticles, possible options are phosphoric acid (phosphonic acid), sulfonic acid and carboxylic acid in order of the strength of their adsorption power. A proper amount of each functional group can control transparency. However, the stronger the adsorption power, the more difficult control becomes because even a small dosage can cause gelation. The carboxylic acid has the widest range of dosages that can achieve homogeneous dispersion without causing gelation. In the dispersion of ZrO_2 nanoparticles with a diameter of 5 nm in styrene random copolymers, the best performance was achieved by keeping the number of carboxyl groups to between ten and fifteen per polymer.

2.2.4 Fluidity

In the above experiment conducted to confirm the principle, specimens were manufactured by pressing the powder with a thermal press machine. To create a more practical molded material, melt-fluidity needed further improvement.

We therefore considered various aspects of controlling fluidity and transparency and discovered that it is extremely important to control the length of the side chains connecting the main chain to the functional groups, and the number of functional groups per polymer (Fig. 9). The fluidity of nanocomposites is poor when using a polymer whose adsorption sites have an acrylic acid structure in which carboxyl groups are directly connected to the main chain. To some extent, the longer the distance between the main chain and functional groups, the better the fluidity becomes and melt extrusion becomes possible with a lower pressure. However, too long a distance will degrade the stability of particle dispersion. It is essential to keep the distance to an optimal value.

Via the above optimization of material technology, we developed a thermoplastic nanocomposite material from ZrO_2 nanoparticles dispersed homogeneously in resin at a concentration of 12.5 vol% and succeeded in the creation of a 1.2-mm-thick, transparent molded body shaped as a convex and concave lens with a d-line transmittance of 92% (Fig. 10).

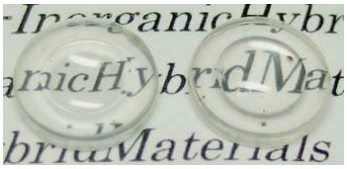

Fig. 10 Appearance of molded nanocomposite lenses.

3. Conclusion

It is no exaggeration to say that the expansion of the controllable refractive index range will always be one of the most challenging topics in the field of optical resin materials. Compared with inorganic materials, resin materials are lighter and excellent in moldability. On the other hand, their narrow range of controllable refractive indexes is a significant issue and effective organic-inorganic composite

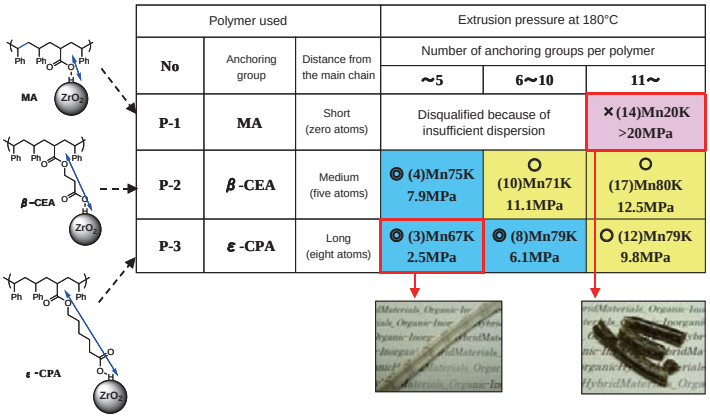

Polymer used			Extrusion pressure at 180°C		
No	Anchoring group	Distance from the main chain	Number of anchoring groups per polymer		
			~5	6~10	11~
P-1	MA	Short (zero atoms)	Disqualified because of insufficient dispersion		×(14)Mn20K >20MPa
P-2	β-CEA	Medium (five atoms)	◎(4)Mn75K 7.9MPa	○(10)Mn71K 11.1MPa	○(17)Mn80K 12.5MPa
P-3	ε-CPA	Long (eight atoms)	◎(3)Mn67K 2.5MPa	◎(8)Mn79K 6.1MPa	○(12)Mn79K 9.8MPa

Fig. 9 Relation between the polymer design and melt-molding processability.

technology has been sought after. However, the application of such technology to thick optical components like lenses was still difficult not only in regard to transparency but also mass producibility. Under such circumstances, focusing on its improvement in mass producibility, we tackled the development of melt-moldable, thermoplastic nanocomposite materials and succeeded in the creation of a transparent molded body. Although there are still several outstanding issues for practical implementation, we hope for its further evolution in the future.

References

1) Yukawa, H. Kikan Kagaku Sosetsu 39, *Tomei Polymer no Kussetsu-ritsu Seigyo* (Control of the Refractive Index of Transparent Polymers), The Chemical Society of Japan. Gakkai Shuppan Center. 174-182 (1998).
2) Oyaizu, Y.; Oshikiri, T.; Tanigawa, H.; Uno, K. *Kino Zairyo* (Functional Materials). **18** (7), 33-40 (1998).
3) Fukui, T. *Tomei Plastic no Saizensen* (The Front Line of Transparent Plastics), The Society of Polymer Science, Japan. NTS, Inc., 195-228 (2006).
4) Imai, Y.; Terahara, A.; Hakuta, Y.; Matsui, K.; Hayashi, H.; Ueno, N. Euro. Polym. J. **45** (3), 630-638 (2009).
5) Hatakeyama, F.; Uchida, S.; Ishizu, K.; Ozawa, M. Polymer Preprints, Japan, **59** (1), 973 (2010).
6) Okada, Y.; Murata, A.; Ando, T.; Suenaga, T.; Korenaga, T.; Suzuki, M. *Kobunshi Ronbunshu* (Japanese Journal of Polymer Science and Technology). **67** (7), 390-396 (2010).
7) Yamada, T.; Iida, K.; Yamago, S. *Kobunshi Ronbunshu* (Japanese Journal of Polymer Science and Technology). **64** (6), 329-342 (2007).
8) Matyjaszeski, K.; Paik, H.; Zhou, P.; Diamanti, S.J. Macromolecules, **34**, 5125-5131 (2001).

Development of a Near-infrared Reflective Film Using Disk-shaped Silver Nanoparticles

Naoharu KIYOTO*, Shinya HAKUTA*, Takeharu TANI*,
Masayuki NAYA*, and Kou KAMADA*

Abstract

FUJIFILM Corporation has developed a novel near-infrared reflective film using disk-shaped silver nanoparticles. We estimated the best shape and arrangement of the silver nanodisks to reflect near-infrared rays by simulation. In order to form an optimum structure, we applied the technology which has been used to form silver halide tabular grains in photographic film. Moreover, we have developed the coating technology to make a uniform layer of silver nanodisks that reflect near-infrared rays effectively.

1. Introduction

With the recent increase in demand for energy savings, heat barrier films have been attracting more attention. Affixed to windows, they block infrared light and thereby decrease cooling load. We developed a new, near-infrared reflective material, using disk-shaped silver nanoparticles, or silver nanodisks[1) to 4)], that can be applied to those films (Fig. 1).

Among such films, the most desired on the market lately are the ones that can block as much infrared light as possible while having a high visible-light transmittance. Fig. 2 shows the solar energy spectrum. Nearly half of solar energy is from infrared light. In particular, energy from the near-infrared region (wavelength of 800 nm to 1,100 nm) is considerable. Therefore, materials that can block near-infrared light are highly demanded. Of the infrared light-blocking materials, reflection types are preferable because absorption types are not very effective, allowing some heat to radiate into rooms.

There are already some heat barrier film products made of near-infrared reflective materials on the market. However, they have some issues in conforming to curved surfaces and in radio-wave transparency. Therefore, we developed a new, near-infrared reflective material to solve those two problems together.

This paper describes the ideal near-infrared reflective structure determined via simulation, a novel technology developed to achieve that structure and the performance of heat barrier films using the material realized based on them.

2. Design of the near-infrared reflective structure using a metamaterial with a silver nanodisk arrangement

To realize a structure that achieves the desired properties, we turned our attention to metamaterials based on the principle of localized plasmon resonance (LPR). LPR is collective motion of free electrons inside metals in resonance with the vibration of the electric field of light. Light is absorbed and scattered intensely near the resonant frequency.

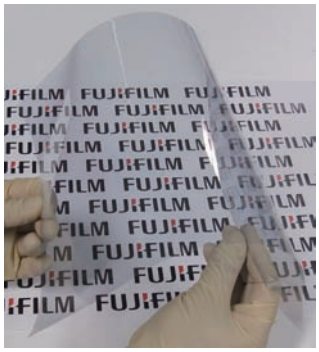

Fig. 1 Near-infrared reflective film using silver nanodisks.

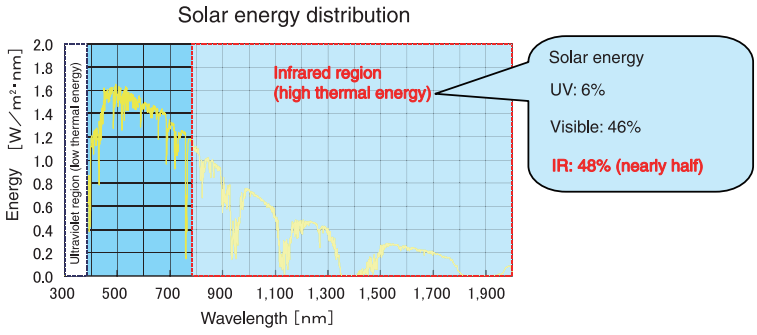

Fig. 2 Solar energy distribution.

Original paper (Received December 13, 2012)
* Frontier Core-Technology Laboratories
Research & Development Management Headquarters
FUJIFILM Corporation
Nakanuma, Minamiashigara, Kanagawa 250-0193, Japan

It is possible to control the frequency of LPR and the tendencies of the scattered light by the size and shape of the metallic nanostructure and its arrangement. Therefore, LPR technology has played a central role in the field of metamaterials to realize unique light properties artificially with nanostructures. LPR occurs most readily in low electrical-resistance precious metals. Among those metals, silver is known to cause the strongest LPR. Based on the above fact, we used a silver nanostructure with the aim of realizing a metamaterial that reflects only near-infrared light while achieving transparency to visible light and radio waves.

To accurately predict properties such as light scattering decided by the shape and arrangement of nanoparticles, we employed a computational electromagnetics technique, the finite-difference time-domain (FDTD) method. Via simulation, we investigated the ideal structure and discovered that, if silver nanodisks can be arranged like a stone pavement as shown in Fig. 3, the intended properties could be realized. The following are the details of that structure.

The shape of the silver nanodisks is an important parameter to control resonance wavelengths. Round silver particles are resonant with visible light. However, if they are shaped into flat disks, by adjusting the aspect ratio (division of the equivalent circle diameter by thickness), silver nanoparticles can be resonant with a wider range of wavelengths from visible light to infrared light[5]. Fig. 4 shows examples of the extinction cross section calculated with different aspect ratios of silver nanodisks. The results indicate that nanodisks with an aspect ratio of about 10 or larger can be resonant in the infrared region.

The key parameter to control reflectance is the distribution of silver nanodisks. Fig. 5 shows the comparative results of simulations for the optical properties of the single-particle system and the silver monolayer dispersion system. In the

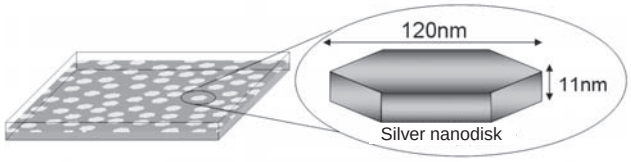

Fig. 3 Best formation and arrangement of silver nanodisks estimated by simulation.

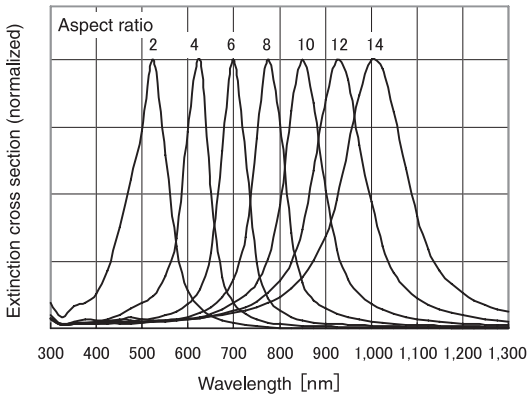

Fig. 4 Resonance wavelength variation according to the aspect ratio of silver nanodisks.

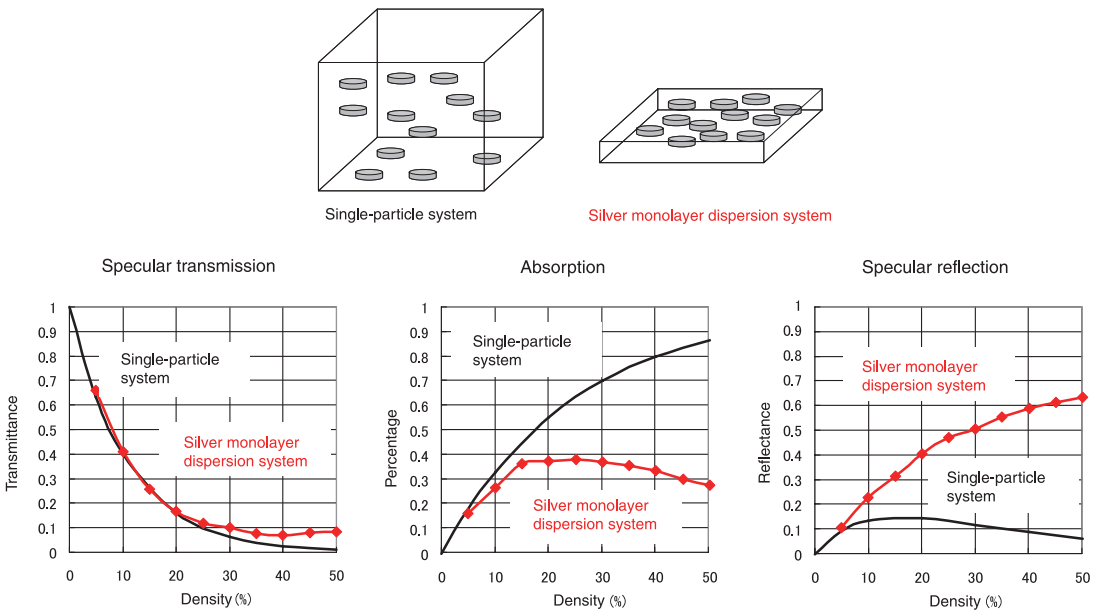

Fig. 5 Spectra of isolated dispersion and monolayer dispersion.

former, silver nanodisks are distributed widely throughout the layer thickness while, in the latter, they are aligned on the same plane. The properties shown in the figure were gained under an infrared radiation of 900 nm set as the central value for plasmon resonance. The results reveal that, in the resonant state of the former, energy is lost mainly by absorption after being scattered but, in the resonant state of the latter, reflection is dominant over energy loss via scattering. That could occur because the dense arrangement of silver nanodisks on the same plane allows plasmon resonance to grow into an electromagnetic field vibration over a larger region across multiple nanoparticles, which facilitates the release of the electromagnetic waves of light to the outside.

The results of the above simulation conducted based on nanophotonic knowledge brought us to the conclusion that, to achieve high visible-light transparency and high near-infrared reflection together, a structure with the following characteristics is optimal.

(1) A film in which silver nanodisks are aligned on the same plane with the proper density.
(2) The thickness of nanodisks being 11 nm with an equivalent circle diameter of 120 nm.
(3) The area packing ratio of the silver being 35%.

3. Manufacture of near-infrared reflective materials

Initially, it was considered to be highly difficult to manufacture the optimum structure derived from the simulation, in particular, on a mass-production scale. However, by applying photographic film technology, we succeeded in the creation of the desired film.

There already exists a photographic film technology to form disk-shaped, silver halide particles and apply them orientated in a plane. We considered a way to create a structural film by utilizing such technology to shape silver nanodisks and arrange them with an appropriate density orientated in a plane.

It was possible to form silver nanodisks in a similar way to silver halide particles, because silver halides and silver belong to the same crystallization system. Fig. 6 shows the manufacturing flow.

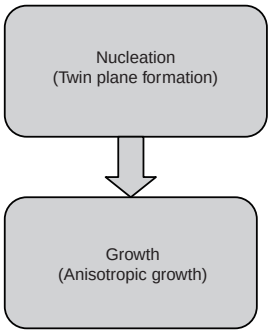

Fig. 6 Flow of silver nanodisk formation.

After establishing the environment for the nucleation process, we first formed twin plane of silver. Because of their natural tendency of growing anisotropically, they could easily grow into disk-shaped particles. In the growing process, too, while growing them under conditions that enhance that tendency, we then manufactured silver nanodisks. By adjusting the growing conditions, we finally succeeded in the creation of the intended silver nanodisks with a thickness of 11 nm and an equivalent circle diameter of 120 nm.

The silver nanodisks thus created cannot form a high-reflectance film by simply applying them, as the nanodisks will be facing in different directions within the coated layer as shown in Fig. 7. It is likely that this occurs because the nanodisks were distributed widely throughout the layer thickness as seen in single-particle system. By applying them under specified conditions, silver nanodisks was able to be arranged like a stone pavement without overlapping one another (Fig. 8).

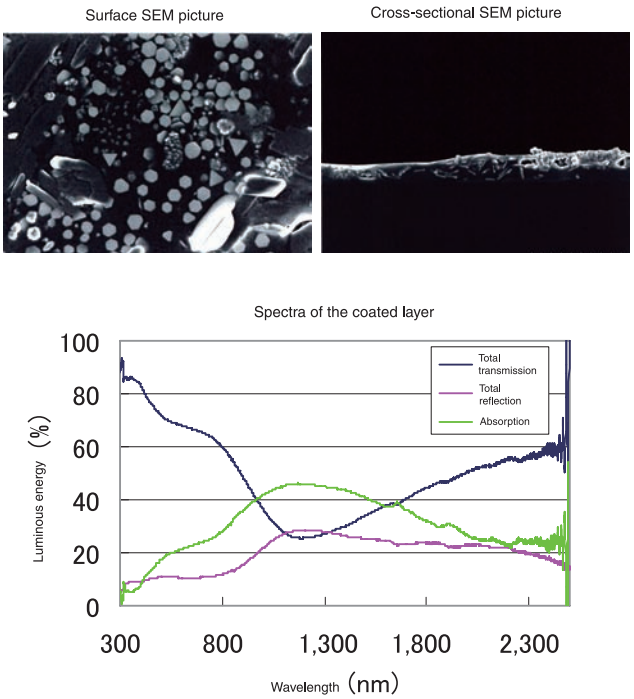

Fig. 7 SEM pictures and spectrum of coating film (before using coating technology).

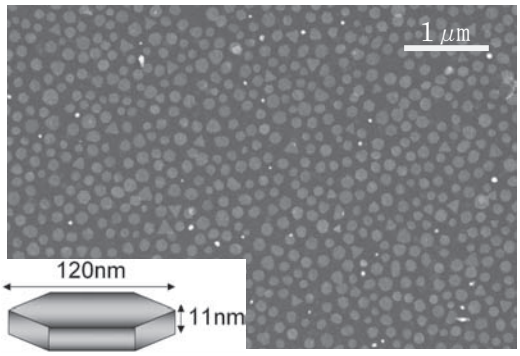

Fig. 8 SEM picture of coating film.

Fig. 9 shows the spectral performance of this coated film. The results of the optical simulation and actual measurement are consistent and have realized high visible-light transparency and high near-infrared reflectance together.

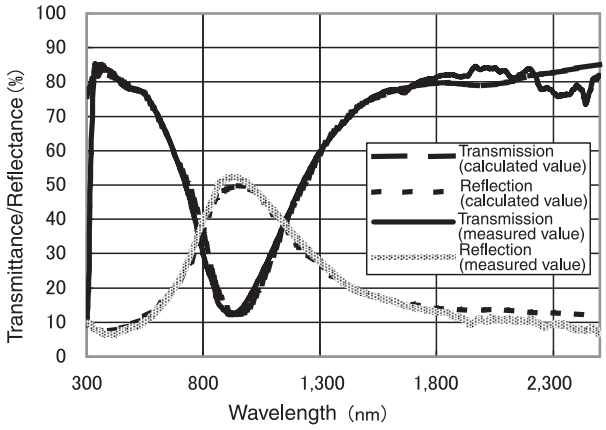

Fig. 9 Experimental and calculated spectra.

4. Characteristics of the near-infrared reflective material

The following are the characteristics of the near-infrared reflective material that we have developed.

(1) Infrared reflection: At the peak of its blocking performance, a large amount of reflection can be detected together with absorption.

(2) Radio-wave transparency: Less than 0.2 dB using the KEC measurement method

(3) No shifts by angle-of-view dependence occur at the peak of its blocking performance.

(4) Good conformation to curved surfaces

5. Application to construction-use heat barrier films

Having applied the heat barrier film made of the newly developed near-infrared reflective material to a window, we conducted an experiment to verify its performance. As a result, the temperature around the window became lower by up to 6.5°C. We then prepared two rooms, with and without the heat barrier film applied, and checked the power consumed by their air conditioners. In the room with the film, the power consumption was reduced by 15% at its peak.

Films made of this near-infrared reflective material are already available on the market for construction-use film manufacturers. They are used in heat barrier films for buildings.

6. Conclusion

Via optical simulation, we derived a film structure that is both transparent and capable of obtaining selective reflection of the near-infrared region and succeeded in the creation of a silver nanodisk-arranged film based on that structure in an actual coating. The film exhibited the property of reflecting near-infrared light as predicted by the simulation.

References

1) FUJIFILM Corporation. Polyfile. **49** (581), 32-33 (2012).

2) Hakuta, S.; Tani, T.; Kiyoto, N.; Kamada, K.; Naya, M. Wavelength-selective Shielding Film with a Silver Nanodisk Monolayer Dispersion Structure. Proceedings of the 59th Meeting of The Japan Society of Applied Physics and Related Societies. 18a-B11-2 (2012).

3) Kiyoto, N.; Hakuta, S.; Kamada, K. Development of Near-infrared Reflective Material Using Disk-shaped Silver Particles. The Society of Photography and Imaging of Japan. **75** (2), 158 (2012).

4) FUJIFILM Corporation. Matsunami, Y.; Kiyoto, N.; Hakuta, S.; Tani, T.; Naya, M.; Kamada, K. *Tokukai* (Japanese Published Unexamined Patent Application) No. 2011-118347. 2011-6-16.

5) Jin, R. et al. Nature, **425**, 487 (2003).

Wavelength Insensitive, Non-contact and Highly Efficient Fiber Optic Connector using Up-tapered Multimode Optical Fibers

Tatsuya YOSHIHIRO*, Yukitaka ONO*, and Tadashi KASAMATSU*

Abstract

A wavelength insensitive, non-contact and highly efficient fiber optic connector has been created and demonstrated excellent performance. The fiber optic connector consists of a pair of up-tapered multimode optical fibers with an insertion loss of 0.9 dB in the range of 410 to 790 nm. With anti-reflective coating applied on the sections, the loss is expected to fall to 0.6 dB. We believe this novel fiber optic connector is suitable for multi-color illumination systems or devices subject to frequent connection and disconnection of the connector.

1. Introduction

1.1 Background

In recent years, with the increased trend for higher-functionality medical equipment, wavelength bandwidth of illumination used by a single piece of equipment has become broader, covering from the near-ultraviolet to near-infrared regions. Such cases include combined optical coherence tomography (OCT, 1300 nm) and laser induced fluorescence (LIF, 325 nm) endoscopy[1] and the simultaneous irradiation of diagnostic laser light (410 nm) and therapeutic laser light (630 nm) when combining photodynamic diagnosis (PDD) with photodynamic therapy (PDT)[2]. At the same time, optical communication between consumer appliances such as audio equipment and PCs has become common, using an extensive range of wavelengths from the visible to infrared regions.

A significant characteristic of those application examples is the simultaneous use of multiple-wavelength laser illuminations. In the future, the bandwidth used is expected to increase still further, which requires a high-efficiency optical connection between the light source and the scope, independent of wavelength.

In addition, when laser illumination is applied to the medical field as described, irradiation heads need to be detachable from light sources for sterilization. For use in consumer appliances, too, connectors require plugging and unplugging. In all cases, contactless optical connection is preferable to avoid damage to light sources and irradiation heads.

Aiming to achieve an unprecedented level of high performance to meet those demands, we designed and manufactured highly efficient, non-contact and wavelength-independent fiber optic connectors using up-tapered fibers[3) to 5)] of multimode fibers. As a result, we achieved an insertion loss of 0.9 dB (transmission efficiency of 81%) at wavelengths between 410 nm and 790 nm. Moreover, with anti-reflective coating on the end faces, we expect that an insertion loss will fall down to 0.6 dB (transmission efficiency of 87%). This paper describes the details of that newly developed connector.

1.2 Conventional optical connection methods

Fig. 1 shows a lighting system, consisting of laser light sources that output light to optical fibers while multiplexing several wavelengths, an irradiation head including optical fibers and an optical connection component for them, and Table 1 indicates general optical connection methods for that case.

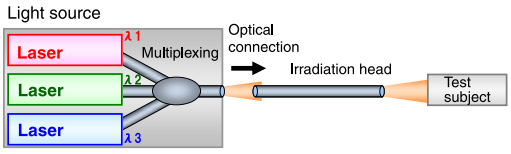

Fig. 1 Schematic diagram of multi-color laser illumination system.

Table 1 Fiber-optic connector types.

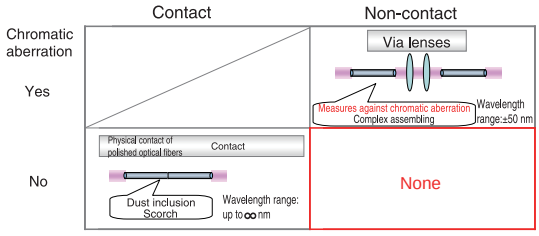

In optical communication, the most commonly used connection method is physical contact. Optical fibers, whose ends are shaped spherically via polishing for physical

Original paper (Received December 4, 2012)

* Frontier Core-Technology Laboratories
Research & Development Management Headquarters
FUJIFILM Corporation
Ushijima, Kaisei-machi, Ashigarakami-gun, Kanagawa 258-8577, Japan

contact, are made to contact each other, by which high transmission efficiency with an insertion loss of 0.3 dB or less (transmission efficiency of at least 93%) is achieved over a broad wavelength bandwidth[6]. However, the connection is susceptible to dust on the fiber ends and not suitable for uses requiring frequent connection in environments that do not allow the cleaning of the ends.

On the other hand, there is a non-contact optical connection method involving lenses, mainly used in railway systems, ship-to-shore connection and military-use fiber optic connectors[6]. As the beam diameter becomes larger at the end of connectors, the connection is resistant against damage including scratches and achieves an insertion loss of 0.8 dB or less (transmission efficiency of at least 83%). However, there are some disadvantages in this method as follows: optical fibers must be aligned with lenses inside connectors; the diameter of fiber ends is not enlarged and this may cause optical pollution there; and lenses, which collect light by utilizing refraction, are susceptible to refractive index dispersion depending on the wavelength.

As a conclusion, there are no established methods for the connection of fiber optic connectors to meet the requirements of systems using laser light sources that have broad wavelength bandwidth.

2. Principle of the up-tapered fiber optic connector

This paper introduces the up-tapered fiber optic connector using up-tapered, multimode fibers, which is a wavelength-independent, non-contact connector with high transmission efficiency. This connector forms a non-contact joint, with a gap of 0.5 mm, by aligning two up-tapered fibers whose core diameter becomes larger toward their ends. Fig. 2 shows a model of the connector.

When geometrical optics is applicable, light transmitted inside a multimode fiber with a sufficiently large core diameter follows etendue conservation (law of conservation of radiance), as expressed by formula (1) below[7], provided the diameter of the core changes adiabatically.

$$r_{in}\mathrm{NA}_{in} = r_{out}\mathrm{NA}_{out} \qquad (1)$$

Variables r_{in}, NA_{in}, r_{out}, and NA_{out} are, respectively, the core diameter of the light-incoming side, the numerical aperture of incoming light, the core diameter of the light-outgoing side and the numerical aperture of outgoing light. For example, if the core diameter of the light-outgoing side doubles while the etendue is conserved, the numerical aperture of outgoing light ($\approx$ beam divergence angle) halves. The up-tapered light connector uses this principle and reduces optical coupling loss derived from the distance between the end faces.

That change of the beam divergence angle happens because light transmitted inside the optical fiber is totally reflected in the tapered region by the angled side walls. Based on geometrical optics, the beam divergence angle decreases by the taper angle every reflection on the side walls of the tapered region. Therefore, different from optical elements such as lenses that depend on refraction, the decrease of the beam divergence angle of up-tapered fibers is almost independent of the wavelength, and this property enables high transmission efficiency over a broad wavelength range.

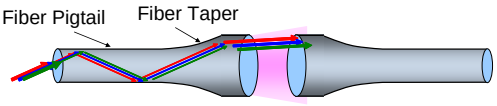

Fig. 2 Fiber optic connector using up-tapered optical fibers.

3. Design and manufacture

3.1 Design of the up-tapered fiber via geometrical optics simulation

Parameters that can be designed in the up-tapered fiber optic connector are the core diameter magnification and the taper length. To investigate optimal parameter values, with the geometrical optics simulation software ZEMAX (developed by Radiant Zemax), we calculated insertion loss for the former parameter while the latter was fixed, and obtained the former parameter value for which the insertion loss became minimum.

Fig. 3 shows the model of the up-tapered fiber optic connector used in this simulation. The core refractive index and clad refractive index of the optical fiber used (NA of 0.22) were 1.45 and 1.433 respectively. The core and clad diameters of the non-tapered region were 104 μm and 126 μm respectively. The up-tapered region approximated a 10-mm-long cone. We calculated insertion loss while enlarging the core/clad diameters respectively from 104 μm/126 μm up to two to six times those values. The simulation results are shown in Fig. 4. Note, however, that the influence of reflection at the fiber ends was ignored.

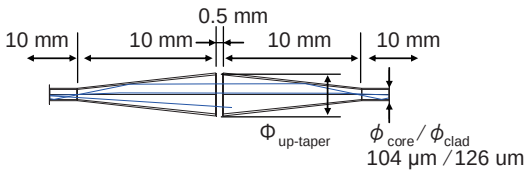

Fig. 3 Simulation model of up-tapered fiber-optic connector for ray trace.

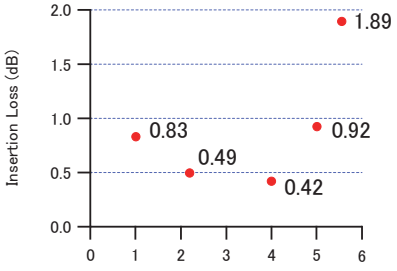

Fig. 4 Calculated insertion loss of up-tapered fiber-optic connector.

The results indicate that insertion loss became the smallest, 0.42 dB (transmission efficiency of 91%), when the core and clad diameters of the up-tapered fibers were quadrupled. For smaller magnification, insertion loss derived from the gap was considerable. On the other hand, for larger magnification, it is likely that insertion loss increased because the up-tapering angle was too steep for the fiber to be regarded as adiabatic and that prevented the ideal beam conversion.

3.2 Manufacture by heating, drawing and fusion splicing

Based on the results of the geometrical optics simulation, we manufactured, by way of a trial, a fiber tapering up from the core/clad diameters of 105 μm/125 μm to about four times those values, i.e. 400 μm/500 μm, respectively.

On the market, there already exist up-tapered fiber products whose taper length is on the order of a few meters. However, as those fibers are manufactured from preforms by changing the drawing speed, they produce much surplus in the process and are very expensive. In addition, their size reduction is not easy. To respond to that issue, we sought a new method to create a more compact product at a lower cost. Specifically, by heating and drawing, we first manufactured a down-tapered fiber[8] from a large-diameter quartz optical fiber, whose core diameter will become smaller toward the end, with core/clad diameters of 400 μm/500 μm and an NA of 0.22; then, by fusion splicing it to another non-tapered quartz optical fiber with core/clad diameters of 105 μm/125 μm and an NA of 0.22, we created an up-tapered fiber. The following are the manufacturing steps.

1. Remove the cladding from a large-diameter fiber
2. Taper down the fiber by heating and drawing
3. Cleave the down-tapered fiber
4. Fusion splice the down-tapered fiber to another non-tapered fiber to create an up-tapered fiber
5. Terminate the end of the up-tapered fiber with an FC connector
6. Apply optical polish to the fiber end

Fig. 5 shows the image of the up-tapered fiber patch cable.

Fig. 5 Up-tapered fiber optic patch cable.

4. Evaluation

4.1 Decrease of the beam divergence angle

A good-quality beam diameter conversion in the up-tapering region can decrease the divergence angle of the beam exiting from the fiber according to etendue conservation. As the magnification of the up-tapered fiber described in this paper is four, the beam divergence angle should become one-fourth that of a non-tapered fiber. The decrease of the beam divergence angle was confirmed by measuring the far-field patterns of the beam exiting from the up-tapered fiber. Fig. 6 is the cross-sectional profile of the measured far-field patterns.

By definition of the beam divergence angle as an angle that includes 63% of the total energy of the beam[9], the angle for the up-tapered fiber was 2.6° while that for the non-tapered fiber was 10.2°. The beam divergence angle was definitely reduced to one-fourth, which means a good-quality beam diameter conversion took place.

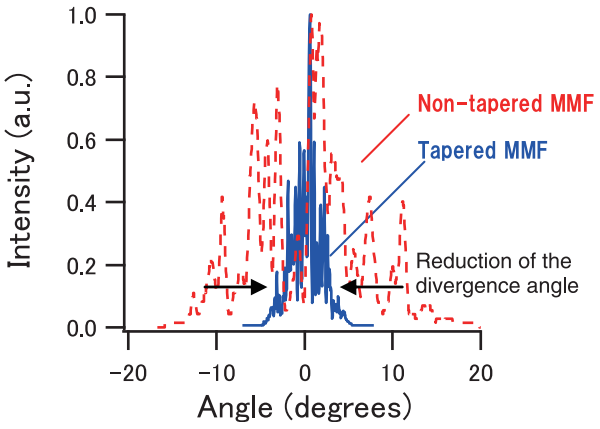

Fig. 6 Sections of far-field radiation patterns of the up-tapered multimode fiber (solid line) and non-tapered multimode fiber (dashed line).

4.2 Wavelength dependence of insertion loss

The insertion loss of the manufactured up-tapered fiber optic connector was measured at wavelengths of 410 nm, 450 nm and 790 nm. Fig. 7 shows the measured values when the distance between the fiber ends was 0.5 mm.

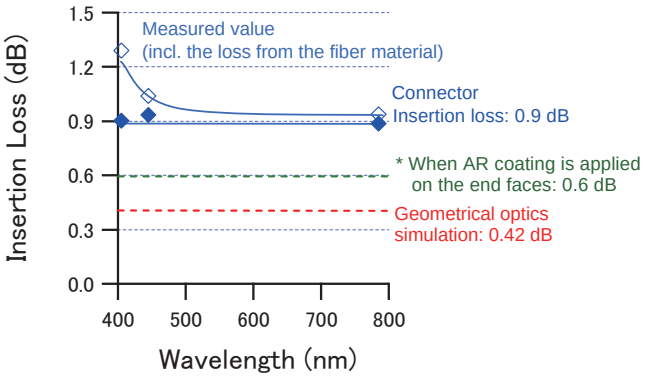

Fig. 7 Insertion loss of up-tapered fiber optic connector, the values measured and calculated by ray trace.

The results revealed that the measured insertion loss increased at a wavelength of 410 nm. The absorption and scattering characteristics of the fiber material are considered to have been the cause. After subtracting the loss from the material itself measured with a non-tapered fiber of the same length, the insertion loss of the connector, which is independent of the wavelength, is 0.9 dB (transmission efficiency of 81%)[10].

Anti-reflective coating was not applied to the ends of the trial optical connector. If the loss from the reflection at the end faces were reduced by applying the coating, the insertion loss could decrease to 0.6 dB (transmission efficiency of 87%). That value approaches the 0.42 dB (transmission efficiency of 91%) obtained in the geometrical optics simulation. We infer that the excess loss of 0.18 dB (4%) originated from the disturbance on the splice point and the tapering side walls.

5. Conclusion and prospects

With several sample up-tapered fiber optic connectors, we succeeded in achieving an insertion loss of 0.9 dB (transmission efficiency of 81%) at wavelengths of 410 nm, 450 nm and 790 nm. It also became apparent that, by applying anti-reflective coating, the insertion loss is expected to be reduced to 0.6 dB (transmission efficiency of 87%).

In spite of the non-contact type optical connection, the up-tapered fiber optic connector introduced in this paper can achieve high transmission efficiency over a broad wavelength bandwidth. Therefore, the connector is suitable for equipment that requires a broad range of wavelengths from illumination and the frequent plugging and unplugging of optical connections, for example, laser endoscopes with multi-colored excitation light sources and photo-sensing fiber devices. In addition, because of its large core diameter, the end face of the fiber optic connector can be more resistant to damage. In the future, we expect to introduce the connector into an extensive range of optical applied equipment such as optical interconnects[11] that requires users to plug and unplug connections on a daily basis.

References

1) Wall, R. Andrew.; Bonnema, Garret. T.; Barton, Jennifer K. Novel focused OCT-LIF endoscope. Biomed. Opt. Express. **2** (3), 421-430 (2011).
2) Fritsch, C.; Lang, K.; Neuse, W.; Ruzicka, T.; Lehmann, P. Photodynamic diagnosis and therapy in dermatology. Skin Pharmacol. Appl. Skin Physiol. **11**, 358-373 (1998).
3) Presby, H.M.; Benner, A.; Amitay, N. Research on an expanded beam single-mode fiber-optic connector. Appl. Opt. **27**, 3121-3123 (1988).
4) Shiraishi, K.; Aizawa, Y.; Kawakami, S. Beam expanding fiber using thermal-diffusion of the dopant. J. Lightwave Technol. **8**, 1151-1161 (1990).
5) Amitay, N.; Presby, H.M. Optical fiber up-tapers modeling and performance analysis. J. Lightwave Technol. **7**, 131-137 (1989).
6) Fiber optic connector catalog by Amphenol Japan, Ltd.
7) Ushiyama, Z. *Simulation Kogaku* (Simulation Optics). Tokai University Press (2003)
8) Birks, Timothy A.; Li, Youwei. W. The shape of fiber tapers. J. Lightwave Techol. **10**, 432-438 (1992).
9) JIS C 6802: 2011 (Safety of laser products).
10) Yoshihiro, T.; Ono, Y.; Kasamatsu T. The 73rd Fall Meeting of the Japan Society of Applied Physics. 13p-F3-2 (2012)
11) Jul. 11, 2011, issue of Nikkei Electronics

Fabrication of Solution-Processed Oxide Thin Film Transistors

Kenichi UMEDA*, Kouhei HIGASHI*, Maki NOMOTO*, Hiroyuki HIRAI*,
Atsushi TANAKA*, and Masayuki SUZUKI*

Abstract

In recent years, the transparent amorphous oxide semiconductor (TAOS) has attracted attention as an active layer for next generation TFTs. With the aim of reducing manufacturing cost, the solution-processed TAOS has been also under review. In this paper, we report on film formation, material analysis and fabrication of $InGaZnO_4$ and In-Zn-O TFTs using the solution-based process.

1. Introduction

Oxide semiconductor material has attracted increased attention because of the two characteristics that it exhibits in the visible light region: optical transparency and electrical conductivity. In particular, in recent years, indium tin oxide (ITO) known for its good transparency and conductivity has been used widely as a transparent electrode material for solar cells and displays. The material is thus becoming more and more common in our daily lives. However, the attention has been limited to its transparency and conductivity and its potential as a functional material for semiconductor devices is yet to be considered.

Under such circumstances, Professor Hideo Hosono of the Tokyo Institute of Technology et al. released, in sequence, a monocrystal transparent oxide transistor using $InGaO_3(ZnO)_5$ in 2003 and a thin film transistor (TFT) deposited at room temperature with an amorphous $InGaZnO_4$ phase in 2004[1), 2)]. In spite of the films being deposited at room temperature, the latter, in particular, was discovered to exhibit high mobility, ten times that of amorphous silicon. Since then, oxide semiconductor materials, mainly those of the In-Ga-Zn-O system, have been attracting much attention as an active layer for next-generation display-use TFTs.

The achievements by Hosono et al. encouraged various research institutes and manufacturers to launch their own research and development of transparent amorphous oxide semiconductors (TAOS) including those of the In-Ga-Zn-O system, and they achieved technological breakthroughs. In particular, Japanese, Koreans and Taiwanese panel manufacturers have been playing leading roles in vigorous trial manufacture of large displays. After much discussion about reliability and stability, and with some advanced consideration of issues relating to mass production, the technology has nearly reached a practical level[3), 4)].

With the trend for larger displays, they have also actively engaged in the establishment of a strategy for next-generation flexible displays incorporating organic material substrates as well as research and development of lower cost manufacturing techniques involving solution-based TAOS-TFTs without using vacuum processes. Among such TFTs are ZnO (2003)[5)], Zn-Sn-O (2006)[6)] and In-Zn-O (2007)[7)] reported mainly by Oregon State University. Today, the number of those reported cases has been increasing dramatically. In addition, at SID 2009, Samsung Electronics introduced to the public a solution-processed 4-inch liquid crystal display driven by a TAOS-TFT[8)]. Expectations for the manufacture of solution-based TFTs have thus been increasing in the world. However, compared with vacuum deposition, the solution-based process requires a higher processing temperature and has difficulty in forming high-quality thin films. Those are the issues yet to be overcome for the future, and there has already been a fierce competition among research institutes from a technical perspective of *how to realize high-mobility and stable elements even in a low-temperature process.*

2. Approaches at Fujifilm

This section describes an outline of our research on oxide semiconductor materials, mainly those of the In-Ga-Zn-O system. Aiming to understand the genuine properties particular to oxide semiconductor materials and their potential, our group takes diverse approaches to the materials research encompassing amorphous to monocrystalline from a wide perspective. Furthermore, we have been carrying out various other researches including evaluation of the basic physical properties of materials and studies to increase the reliability and stability of TFT devices, looking to their practical application as well. The following are some of our concrete research achievements[9)].

I. With the ceramics solid-phase reaction method, we

Original paper (Received November 12, 2012)
* Frontier Core-Technology Laboratories
Research & Development Management Headquarters
FUJIFILM Corporation
Ushijima, Kaisei-machi, Ashigarakami-gun, Kanagawa 258-8577, Japan

conducted an accurate evaluation of the basic physical properties of In_2-xGaxZnO$_4$-δ (δ: concentration of oxygen vacancy) in the region where semiconductive properties are exhibited. We elucidated the Ga solid solution region as a crystalline phase and the relevant electrical properties.

II. With reactive solid-phase epitaxy, we manufactured a single-crystal film of $InGaZnO_4$. While considering the possibility of process improvement, we evaluated the electrical properties of its single-crystal structure and, with the single-crystal film, elucidated the material-specific dependence on measurement environment.

III. We synthesized $InGaZnO_4$ and In-Zn-O ingredients that are compatible with the solution process. By applying spin coating and the inkjet method, we manufactured and evaluated devices and succeeded in the realization of oxide TFTs with good properties.

IV. To improve the reliability of the In-Ga-Zn-O TFT deposited by sputtering, we newly employed oxide gallium as its protective layer. With this, the reliability was increased in regard to the prevention of threshold shifting.

V. Aiming to improve the photostability of the In-Ga-Zn-O TFT in the visible light region, we modulated its synthesis, focusing on the In/Ga ratio of the film and thus improved the photostability by enlarging the optical band gap.

VI. We evaluated the effect of post annealing at around 200°C on the conductivity of the amorphous In-Ga-Zn-O film deposited by sputtering. By scrutinizing it via *in-situ* measurement, we revealed that moisture contained in the film greatly affects the conductivity after post annealing.

In the next section, we report the details of the manufacture of the solution-processed oxide TFTs described in III above.

3. Manufacture and evaluation of solution-processed $InGaZnO_4$ and In-Zn-O TFTs

3.1 Synthesis and evaluation of precursor materials

There are several possible ingredients that can be used to manufacture solution-processed oxide materials, such as metal alkoxide, metal organic acid salt, nitrate and chlorides. We employed, as a starting ingredient, metal alkoxide, which is an organometallic compound, and manufactured a precursor solution for oxide semiconductors. The ingredient consists of metal atoms bonding with alcohol groups and is naturally free of unnecessary elements such as chlorine, which is convenient for the manufacture of electronic devices[10].

Fig. 1 shows the synthesis sequence of $InGaZnO_4$ precursor solution. For In, Ga and Zn ingredients, In-(O-C_3H_7)$_3$ (Kojundo Chemical Laboratory, 3N), Ga-(O-C_3H_7)$_3$ (Soekawa Chemical, 3N) and $Zn(CH_3COO)_2 \cdot 2H_2O$ (Kojundo Chemical Laboratory, 3N) were used respectively. The dosages of those ingredients were measured precisely to achieve the required composition of $InGaZnO_4$ film. The solvent used to improve solubility and temporal stability was $(C_2H_5)_2NC_2H_5OH$, i.e., diethylethanolamine (Wako Pure Chemical Industries). We calculated the composition ratio of the manufactured precursor solution with an ICP measurement method and gained the result of In:Ga:Zn = 1:1:0.95.

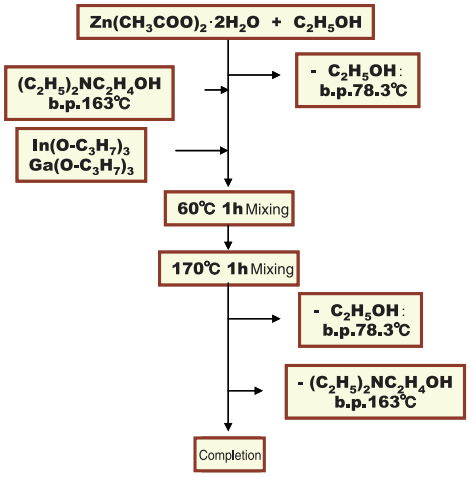

Fig. 1 Synthesis flow of $InGaZnO_4$ precursor solution.

We then measured the pyrolysis characteristic of the $InGaZnO_4$ precursor solution via thermogravimetry-differential thermal analysis (TG-DTA) (Fig 2).

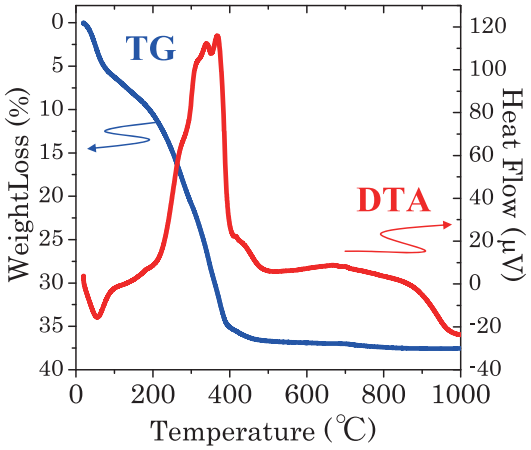

Fig. 2 TG-DTA characteristics of $InGaZnO_4$ precursor solution.

Weight loss by burning of organic matter had stopped when the temperature reached about 400°C, and it was confirmed that dehydration polycondensation progressed with the increase

of annealing temperature. Fig. 3 indicates the dependence of the X-ray diffraction (XRD) patterns on annealing temperature with the $InGaZnO_4$ solution-applied film (spin coat film). As shown, they kept a stable amorphous phase up to 600°C annealing and were crystallized in a single phase at 700°C or above. This is the same level of tendency as reported with vacuum-processed films. It was thus recognized that the precursor solution, as the starting ingredient, can form single-phase $InGaZnO_4$.

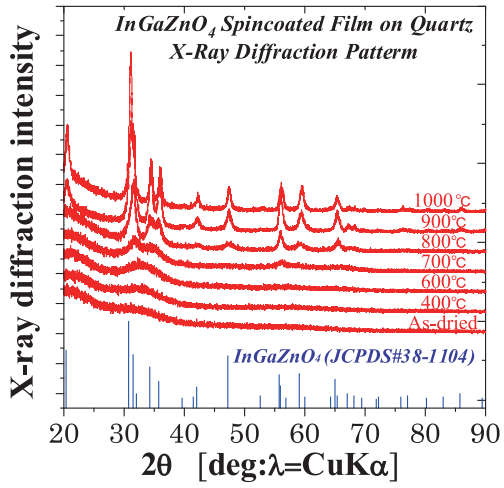

Fig. 3 Annealing temperature dependence of the XRD patterns of $InGaZnO_4$ film.

3.2 Manufacture and evaluation of TFTs

We manufactured Top-Gate TFTs from the above $InGaZnO_4$ solution, respectively with spin coating and inkjetting, and evaluated their electrical properties. For patterning deposition with the latter method, it is necessary to select optimal solution parameters, such as viscosity, surface tension and wettability, considering suitability to each inkjet equipment in use. We used the DMP2831 inkjet system manufactured by FUJIFILM Dimatix and adjusted parameters focusing on the viscosity of the solution. Specifically, by adding alcohol-soluble, high-viscosity cyclohexanol to that $InGaZnO_4$ solution (viscosity: 4.5 cps), we prepared an inkjet-compatible $InGaZnO_4$ solution (printable ink) with a viscosity of 9.89 cps.

Fig. 4 shows the TFT manufacturing sequence. We deposited

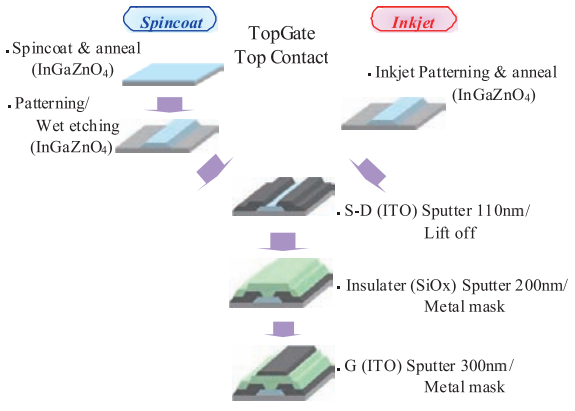

Fig. 4 Process flow of TFT fabrication.

$InGaZnO_4$ thin films on a quartz substrate. In the case of the spin-coated film, photolithography was applied for patterning. The source/drain electrode manufacturing process and the subsequent stages were the same, regardless of the deposition method of the films. Fig. 5 shows the characteristics of the TFTs manufactured with the spin-coated and inkjetted films both of which underwent 900°C annealing. Both TFTs were confirmed to have good characteristics. However, compared with the spin-coated TFT, those of the inkjetted TFT were slightly inferior. We presume that it was caused by the disorder of patterns and non-homogeneity of films derived from the drying speed during the deposition process. That is the issue in the future.

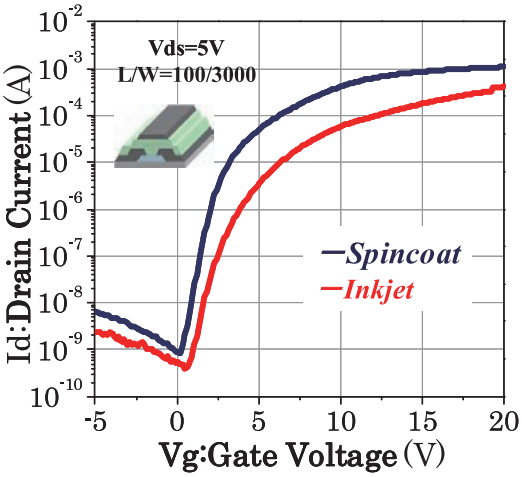

Fig. 5 Vg-Id characteristics of spin-coated and inkjetted $InGaZnO_4$ TFTs (At an annealing temperature of 900°C).

3.3 Lowering of the processing temperature

The above TFTs exhibited fine characteristics. However, the processing required a high temperature of 900°C. That will greatly limit the choice of substrate material in practical applications. Moreover, high-temperature annealing made $InGaZnO_4$ films polycrystalline; therefore, there are concerns about the impact of grain boundaries on the element properties, in particular, about non-homogeneity. When in the amorphous state, the manufactured $InGaZnO_4$ films did not exhibit satisfactory characteristics, causing the on-state current to significantly drop. Therefore, we improved the starting ingredients so that the film can achieve good TFT characteristics while keeping the oxide semiconductor layer of the active layer in the amorphous state, putting emphasis on lowering the processing temperature. To do so, there are several approaches to the composition, morphology (such as nanoparticles), solution design, process control, etc. In this section, focusing on Ga that is considered to control the density of the carriers of the In-Ga-Zn-O system, we tried to increase the on-state current while lowering the processing temperature by decreasing the Ga concentration and increasing the carrier density. In the meantime, the

In-Zn-O system without Ga (i.e., IZO, in the case of this paper, the composition is In:Zn=1:1) achieved a characteristic result. We will describe it below.

We synthesized a precursor solution of the In-Zn-O system in the same way as $InGaZnO_4$, using alkoxide as the starting ingredient. In the XRD evaluation of the spin-coated film, it was confirmed that the film retained the amorphous state in annealing up to 600°C and, including the pyrolysis characteristic, had almost the same material characteristics as those of $InGaZnO_4$.

Next, we deposited an In-Zn-O film on a silicon substrate having a thermal oxide film by spin coating and manufactured a simplified evaluation-use TFT element via 600°C annealing. In normal atmospheric conditions, it exhibited electrical conductivity but, when measured in dry air where moisture was removed, it showed TFT behavior. Furthermore, under the same conditions, TFT behavior was also observed in an In-Zn-O film annealed at 400°C. It became apparent that the processing temperature can be lowered to a level that allows the use of common glass substrates (Fig. 6). It is highly likely that composition control by decreasing the Ga concentration (i.e., Ga removal) had a positive effect on lowering the processing temperature.

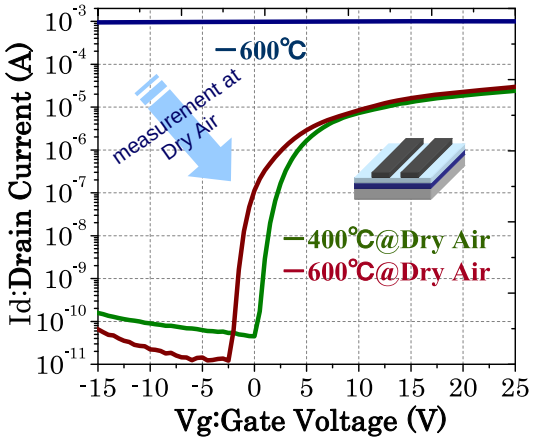

Fig. 6 Influence on measurement environment for spin-coated In-Zn-O TFTs, and annealing temperature dependence.

Structurally, as the active layer (In-Zn-O layer) of the simplified evaluation-use specimen was directly exposed to the external air, the electrical property was affected greatly by the atmosphere. A similar tendency has already been reported about vacuum-processed oxide TFTs. The film used in the current specimen was manufactured with the solution process. It is assumed that, compared with vacuum-processed specimens, such TFTs are more susceptible to the solvent ingredients of the solution, and residuals and defects in the film [11), 12)].

Finally, preparing an inkjet-compatible solution in the same way as $InGaZnO_4$, we manufactured an In-Zn-O Top-Gate TFT and evaluated its physical properties. As shown in Fig. 7, in the case of 600°C annealing, both spin-coated and inkjetted films achieved as good TFT characteristics as $InGaZnO_4$. Also, because the gate insulator of the TFT manufactured in this experiment functioned as a protective layer and isolated the active layer from the external air, TFT behavior was observed in a normal measurement atmosphere.

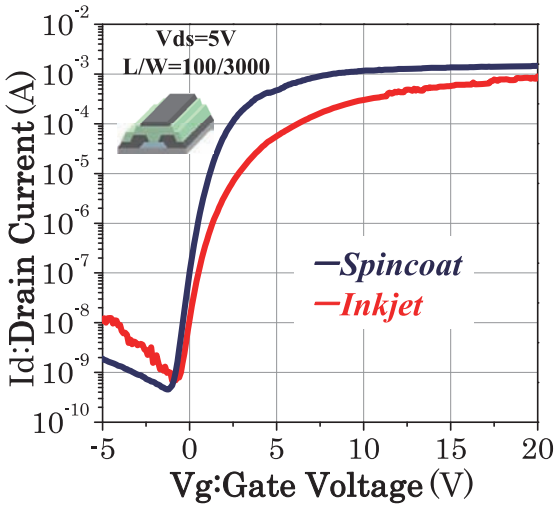

Fig. 7 Vg-Id characteristics of spin-coated and inkjetted In-Zn-O TFTs (At an annealing temperature of 600°C).

4. Conclusion

As described, based on the idea of building thin film transistors via the solution process instead of vacuum processing, solution-processed TFTs have been emerging. Under such circumstances, there is an increasing demand for diverse printing technologies and the corresponding material design. In this research, we synthesized precursor solutions for the deposition of an $InGaZnO_4$ film that allows the proper functioning of TFTs and an In-Zn-O film that is effective for the lowering of processing temperature. In addition, we succeeded in the manufacture of inkjet-compatible *printable ink*. In the future, based on these technologies, we will expand new application fields, aiming at further innovation.

References

1) Nomura, K.; Ohta, H.; Ueda, K.; Kamiya, T.; Hirano, M.; Hosono, H. Science, **300**, 1269-1272 (2003).
2) Nomura, K.; Ohta, H.; Takagi, A.; Kamiya, T.; Hirano, M.; Hosono, H. Nature, **432**, 488-492 (2004).
3) Hosono, H.; Nomura, K. The Current Trends and Prospects of Oxide TFT. Gekkan Display. January, 4-13 (2011).
4) Kamiya, T.; Nomura, K.; Hosono, H. Sci. Technol. Adv. Mater. **11**, 044305 (2010).
5) Norris, B.J.; Anderson, J.; Wager, J.F.; Keszler, D.A. J. Phys. D: Appl. Phys. **36**, L105-107 (2003).
6) Herman, G.S. TAOS2006, 3 (2006).

7) Lee, D.H.; Chang, Y.J.; Herman, G.S; Chang, C.H. Adv. Mater. **19**, 843-847 (2007).
8) Souk, J.H.; Roh, N.S. SID Symposium Digest of Technical Papers. **40** (1), 622-624 (2009).
9) The 57th Meeting of The Japan Society of Applied Physics and Related Societies (2010):
(a) Umeda, K.; Tanaka, A.; Suzuki, M. In_2-xGaxZn$O_{4-\delta}$ Solid-Solution System Synthesized by Ceramics Solid Reaction Method. 17a-TL-2.
(b) Nara, Y.; Takata, M.; Umeda, K.; Mochizuki, F.; Tanaka, A.; Suzuki, M. Fabrication and Electrical Characteristic of $InGaZnO_4$ Single Crystalline Thin Film. 17a-TL-3.
(c) Umeda, K.; Hirai, H.; Higashi, K.; Nangu, M.; Tanaka, A. Fabrication of In-Ga-Zn-O & In-Zn-O TFTs using Solution-Based Process. 17a-TL-7.
(d) Nakayama, M.; Itai, Y.; Tada, H.; Imai, S.; Mishima, Y. Effect of GaO Layer on IGZO-TFT Channel. 17a-TL-8.
(e) Hama, T.; Mochizuki, F.; Tanaka, A.; Suzuki, M. Photostability of Ga-rich Amorphous IGZO TFTs under Visible Light Irradiation. 17a-TL-9.
The 58th Meeting of The Japan Society of Applied Physics and Related Societies (2011):
(f) Takata, M.; Ono, M.; Mochizuki, F.; Tanaka, A.; Suzuki, M. In-Situ Temperature Dependence of Conductivity of IGZO Thin Films. 24a-BS-4.
10) Bradley, Donald C. Chem. Rev., **89**, 1317-1322 (1989).
11) Kim, Y.H.; Kim, H.S.; Han, J.I.; Park, S.K. Appl. Phys. Lett. **97**, 0921051-0921053 (2010).
12) Kang, D.; Lim, H.; Kim, C.; Song, I.; Park, J.; Park, Y.; Chung, J. Appl. Phys. Lett. **90**, 192101-192103 (2007).

Dewetting Flow Caused by Inter-surface Force during Hydrophobic Patterning

Kimiaki MIYAMOTO*

Abstract

Hydrophobic patterning is a method of precise pattering for printed electronics. Exposure to UV light is used to create wiring and electrode patterns on a pre-coated photo-polymer, then hydrophilic conductive ink makes the pattern according to the hydrophilicity induced by the UV light. This study clarifies effects of difference in inter-surface force of adjacent regions and effects of surface unevenness by solving a film profile equation. The results show that stripes of two different levels of hydrophobicity provide a sufficient condition to make a dewetting pattern. In other words, it is not necessary to combine the hydrophilic stripe with the hydrophobic stripe for creation of a dewetting pattern. Also, it was found that hydrophobicity in a hill of a wavy surface is better for quick dewetting. If this status is reversed, namely hydrophobicity in a valley on the surface, stabilization or slow dewetting is caused. These findings suggest that the capillary force and inter-surface force affect each other during dewetting when the thickness is in the sub-micron order and no gravity effect occurs to level the surface.

1. Introduction

Recent development of organic semi-conductors has enabled Thin Film Transistors (TFTs) to be fabricated using printing technology alone. Although many samples of printed TFTs have been exhibited at trade-shows, it is hard to start mass-production because of the printing accuracy required. Inkjet printing is preferable because it has flexible alignment features and allows printing TFTs on demand. However, the problem with IJ technology is the trade-off between productivity and drop size that is typically 10 microns. In contrast, the typical TFT requires a 5 micron gap between source and drain electrodes.

Photonic assistance or hydrophobic patterning was proposed to overcome the difference between IJ accuracy and requirements when printing TFTs [1), 2)]. This method changes the hydrophobic polymer surface allowing it to be wetted by hydrophilic IJ ink. A special hydrophobic polymer on a substrate is exposed to patterned UV light as shown in Fig. 1. Then its surface changes to hydrophilic by a chemical decomposition. This reaction has the additional effect of shrinkage of polymer which combines the chemical pattern and physical pattern. When hydrophilic IJ ink is sprayed roughly on the hydrophilic part, the ink dewets the hydrophobic surface and concentrates at the hydrophilic part. Accuracy of this process depends on the dewetting behavior of the surface-ink system.

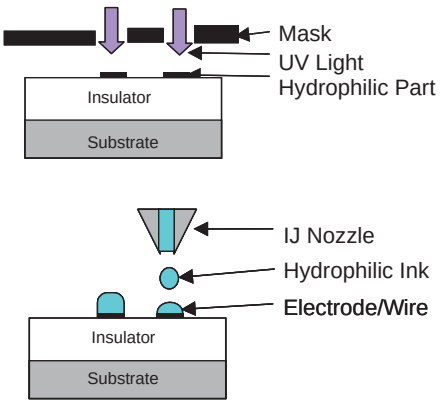

Fig. 1 Process of hydrophobic patterning.

Intensive analysis of patterned dewetting was carried out by A. Sharma et al. [3)~5)], but they limited cases to very thin film of fine patterns for use in the photo-lithography of semiconductor process. In the field of printed electronics, concerns are on much thicker film and a coarser pattern in the order of micrometers. This study elaborates on the dewetting phenomena found in the actual printed electronics process including the dewetting effect of solid surface morphology, Hamaker constant and liquid film parameters. The author adopts a theory by D. K. Owens and R. C. Wendt [6)] for the relationship between a contact angle and dispersion/non-

Original paper (Received October 26, 2012)
* Research & Development Management Headquarters
FUJIFILM Corporation
Ushijima, Kaisei-machi, Ashigarakami-gun, Kanagawa 258-8577, Japan

dispersion components of both liquid and solid (eq. 1a-1c), which is an extension of the theory by Fowkes [7]. Also the empirical relationship between surface energy components and the Hamaker constant is used according to A. Sharma and G. Reiter [4] (eq. 2).

$$\gamma_i = \gamma_i^d + \gamma_i^h \tag{1a}$$

$$\gamma_{SL} = \gamma_S + \gamma_L - 2\sqrt{\gamma_S^d \gamma_L^d} - 2\sqrt{\gamma_S^h \gamma_L^h} \tag{1b}$$

$$1 + \cos\theta = 2\sqrt{\gamma_S^d}\left(\frac{\sqrt{\gamma_L^d}}{\gamma_L}\right) + 2\sqrt{\gamma_S^h}\left(\frac{\sqrt{\gamma_L^h}}{\gamma_L}\right) \tag{1c}$$

$$a_H = -24\pi {d_0}^2 \sqrt{\gamma_L^d}\left(\sqrt{\gamma_S^d} - \sqrt{\gamma_L^d}\right) \tag{2}$$

where γι is the surface energy of liquid L or solid S in [N/m], $\gamma\iota^{d}$ is the dispersion component of surface energy, $\gamma\iota^{h}$ is the non-dispersion component of surface energy and θ is the contact angle. a_H is the Hamaker constant [J] of this system and d_0 is the separation distance at contact [m].

This relationship supports the use of the Hamaker constant as a parameter for the disjoining pressure of a liquid–solid system (eq. 3). The flow driven by the disjoining pressure was analyzed earlier by M. B. Williams and S. H. Davis [8] but the results were not precise enough. This study shows the results in greater detail with much more accuracy.

$$\Pi = \frac{a_H}{6\pi\delta^3} \tag{3}$$

where Π is the disjoining pressure [Pa], δ is the liquid film thickness [m].

2. Model

The simplest model to examine the dewetting hydrodynamics is evenly coated liquid film on a flat surface with one half of the area hydrophilic and the other half hydrophobic as shown in Fig. 2.

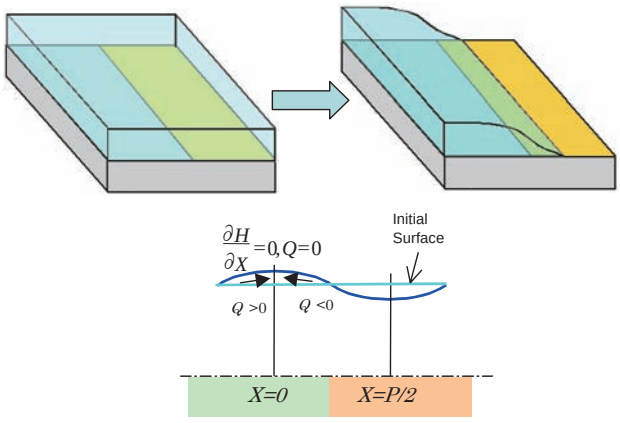

Fig. 2 Model for flat surface.

The boundary of these two regions is linear and a calculation domain corresponds to a half of the pitch of the line pattern. The well-known Film-Profile Equation (eq. 4) is used for calculation together with lubrication approximation.

$$\frac{\partial\delta}{\partial t} = -\frac{\partial q}{\partial x} \quad , \quad \frac{\partial\delta}{\partial t} = \frac{\partial}{\partial x}\left[\frac{\delta^3}{3}\left(\frac{\partial p}{\partial x}\right)\right] \tag{4}$$

where q is the unit width flow rate [m^2/s], p is the total pressure in the liquid film [Pa].

Here, the pressure gradient includes not only the gravity potential term and capillary force term but also the gradient of a Hamaker constant and that of an inter-surface force.

(eq. 5) In the equation, ρ is the density [kg/m^3], σ is the surface tension [N/m] and h is the surface position [m].

$$\frac{\partial p}{\partial x} = \rho g\frac{dh}{dx} - \sigma\frac{d^3h}{dx^3} - \frac{1}{6\pi\delta^3}\frac{da_H}{dx} + \frac{a_H}{2\pi\delta^4}\frac{d\delta}{dx} \tag{5}$$

Coverage of this model is limited to calculation from the beginning of film thinning to the instant of film breakage at the thinnest point. Thus, the process of a receding contact line is not covered in this study.

Before solving the model numerically, the analytical relationship between a Hamaker constant and parameters is deduced. Dewetting flow stops when the capillary force balances with the inter-surface force (eq. 6). Assuming that the film surface shape is a sinusoidal curve (Fig. 3), a simple equation expressing the parameter effect on the critical Hamaker constant is deduced. This shows that the Hamaker constant is proportional to the surface tension σ and the fourth power of the thickness δ, and inversely proportional to the square of the pitch p_w (eq. 7). These findings are compared with numerical results in the next section.

$$\sigma\frac{d^3h}{dx^3} \approx \frac{a_H}{2\pi\delta^4}\frac{d\delta}{dx} \tag{6}$$

$$a_H = -\frac{(2\pi)^3\delta^4}{{p_W}^2}\sigma \tag{7}$$

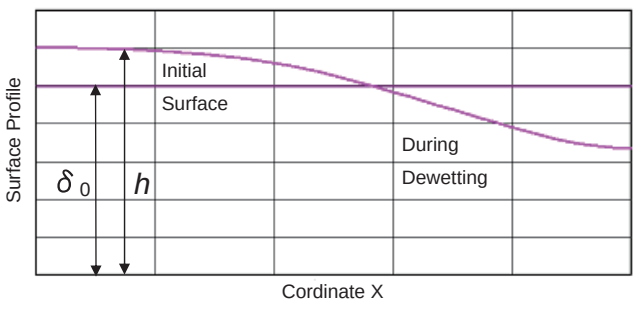

Fig. 3 Simple analytical model.

3. Parameter study by numerical calculation

Numerical analysis is performed with a flat surface, sinusoidal surface (eq. 8) and terrace surface (eq. 9).

$$h = \delta + h_0 = \delta - A_{mp}\cos(2\pi x / p_w) \tag{8}$$

$$h = \delta + h_0 = \delta + A_{mp}\tanh(\alpha(x - x_{orgn})/\delta) \tag{9}$$

where A_{mp} is the amplitude of waviness [m], a is the slope parameter [–] and h_0 is the position of a solid surface [m].

With a terrace shape, polymer shrinkage by UV light and various line-and-space ratios are well demonstrated. Solutions are acquired by using the finite difference method and Euler integration with seven point expression of third order derivatives for better accuracy. Non-dimensionalization is performed by using the initial film thickness δ_0 as the length scale and $\mu/\rho g\,\delta_0$ as the time scale. As a result, two non-dimensional parameters, the Bond number *Bo* and non-dimensional Hamaker constant A_H, are derived (eq. 10).

$$B_o = \frac{\rho g \delta_0^2}{\sigma} \quad , \quad A_H = \frac{a_H}{\rho g \delta_0^2} \tag{10}$$

Basic parameters are 0.001 Pa.s for viscosity, 0.02 N/m for surface tension, 1,000 kg/m^3 for density, 0.1 µm for the liquid film thickness, 50 µm for the pitch of a stripe and +/− 10% difference in level between the steps of a terrace. Calculations are done with each value of the Hamaker constant (mostly negative) for the right half and with zero Hamaker constant for the left half in this parameter study section. Various combinations of Hamaker constants are investigated in the next section.

Two major phenomena, wetting and dewetting, are observed by the calculation (Fig. 4a, Fig. 4b). The dewetting case shows rapid thinning at the hydrophobic side creating zero thickness at the center of a hydrophobic stripe. There is a critical Hamaker constant that distinguishes between wetting and dewetting. In addition, strong dewetting may cause droplet formation resulting in incomplete dewetting with liquid left behind on the hydrophobic part (Fig. 4c).

The hyperbolic tangent function is mainly used for a solid surface shape because this function can express a terrace shape that is commonly used in an actual printed electronics process (Fig. 5). A line-and-space ratio is usually not 1.0/1.0 because it depends on the circuit design, and a slope of the boundary between a hill and a valley varies depending on the defocus level of the UV light. These two surface morphology effects are examined first by changing parameters of the hyperbolic tangent function before calculating parameter

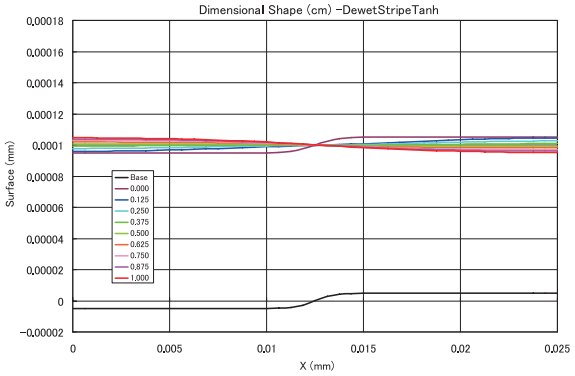

Fig. 4a Wetting.

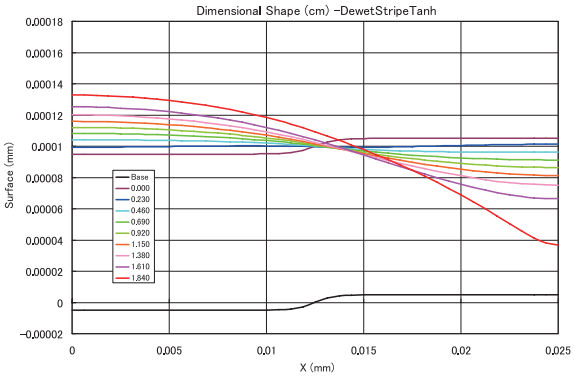

Fig. 4b Dewetting.

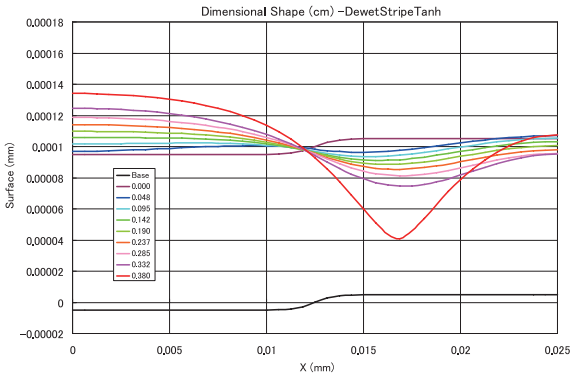

Fig. 4c Drop formation.

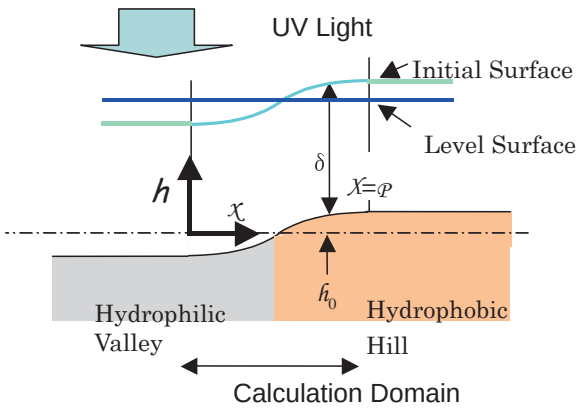

Fig. 5 Model for curved surface.

effects. Fig. 6 shows the effect of the line-and-space ratio by shifting the origin of a hyperbolic tangent function together with a hydrophobic area that is on the right side of the origin of the curve. The vertical axis shows a negative critical Hamaker constant that distinguishes between wetting and dewetting, and the area above the graph line indicates dewetting resistance. The graph shows that the critical Hamaker constant changes slightly when the line-and-space ratio is changed from 12.5/37.5 to 37.5/12.5. Also the effect of slope is found to be weak as shown in Fig. 7. Therefore, the line-and-space ratio is fixed at 1.0/1.0 and a slope parameter of 0.1 is used in further sections.

The author examined the effects of solid surface shapes by using the shape function of flat, sinusoidal and hyperbolic tangent. The results for three surface shapes and an approximate solution are compared in Fig. 8 where the vertical axis also indicates a negative critical Hamaker constant. It is found that the surface waviness does not have much influence but it assists dewetting especially for shorter pitches. Waviness helps dewetting, which suggests a capillary force created by a curvature accelerates flattening and thinning the film toward dewetting at the beginning. However, the effect of shorter pitches, unlike the waviness effect, resists thinning in a later stage with a capillary force created by a concave surface. Also the graph shows that the simple analytical model represents a fair approximation of the numerical calculation for a flat surface. The comparison between the simple model and various parameter effects will be performed.

Effects of liquid parameters are examined. The effect of viscosity is shown in Fig. 9 using the time length required for dewetting instead of a critical Hamaker constant as viscosity does not affect a critical Hamaker constant. This is because viscosity is only used in the non-dimensional time, not in the non-dimensional parameters in the differential equations. Therefore, the dewetting time required is linearly proportional to the degree of viscosity, which coincides with the empirical knowledge, “increase viscosity to prevent dewetting.”

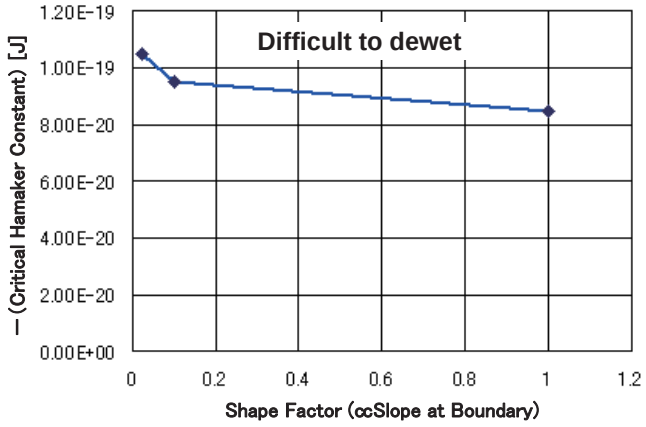

Fig. 7 Effect of slope at the boundary on the critical Hamaker constant.

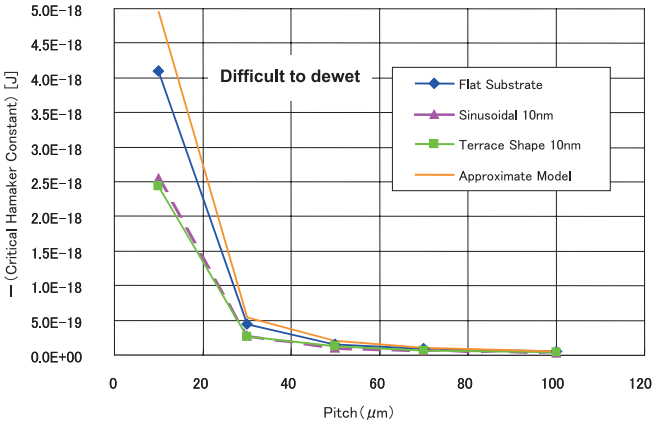

Fig. 8 Effect of pitch on the critical Hamaker constant.

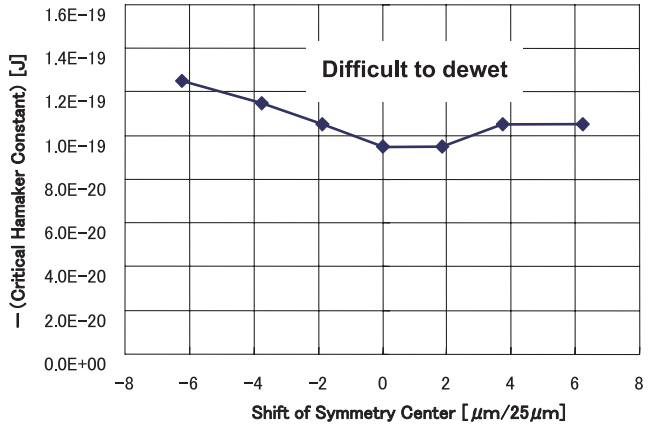

Fig. 6 Effect of line-and-space ratio on the critical Hamaker constant.

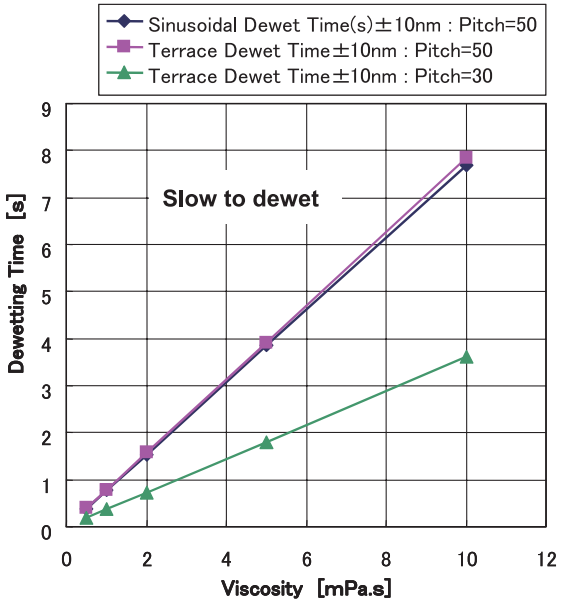

Fig. 9 Effect of viscosity on dewetting time.

The surface tension effect is examined, and in Fig. 10 the relationship between negative critical Hamaker constants and surface tension for various morphologies is shown. All the lines converge at the origin of the graph and dependence is linearly proportional to the surface tension. The effect of a pitch is shown together with the surface tension effect. These effects can be reasonably explained by a hypothesis that the flattening effect of capillarity and the dewetting effect of hydrophobicity affect the level between each other. This mechanism is much different from the conventional theory, which solved the same equation, of film leveling caused by gravity and capillarity. The simple model result agrees with the numerical result for proportionality.

The effect of film thickness to the negative critical Hamaker constant is found to be proportional to 3.82 power of the thickness, which is slightly different from the analytical value of 4 (Fig. 11). The graph shows that there is no difference between the sinusoidal surface and terrace surface.

4. Combination of two Hamaker constants for the hydrophobic area and hydrophilic area

There are various combinations of wettability of the hydrophilic area and the hydrophobic area in actual products. The result from the film on a combined surface with two Hamaker constants is of interest. Fig. 12, Fig. 13 and

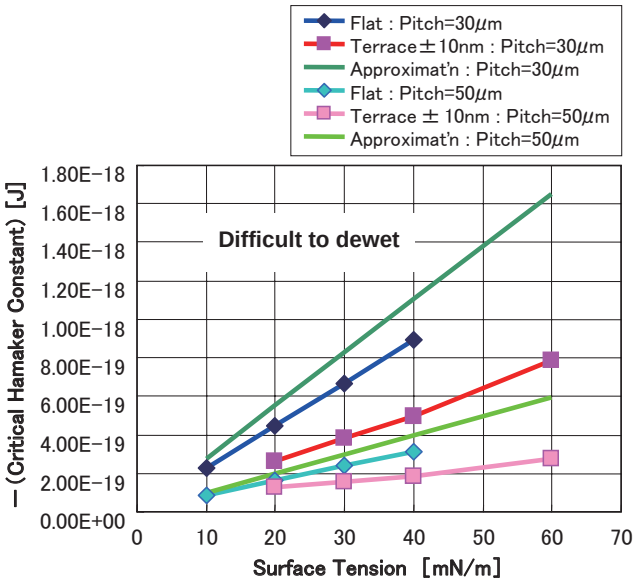

Fig. 10 Effect of surface tension on the critical Hamaker constant.

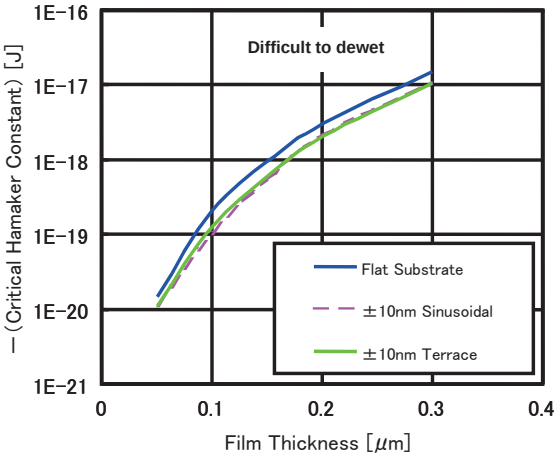

Fig. 11 Effect of film thickness on the critical Hamaker constant.

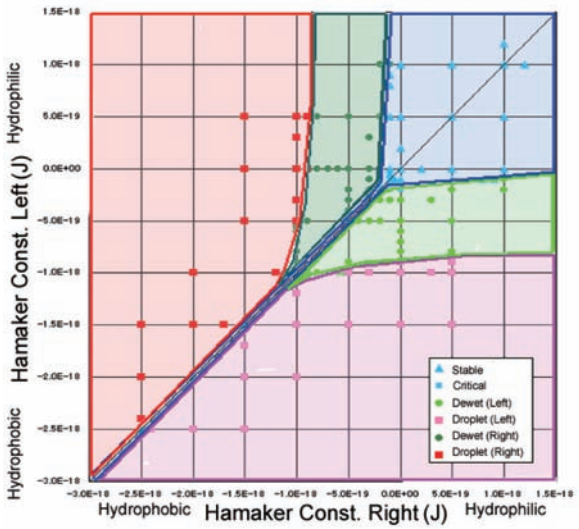

Fig. 12 Dewetting window for flat surfaceo.

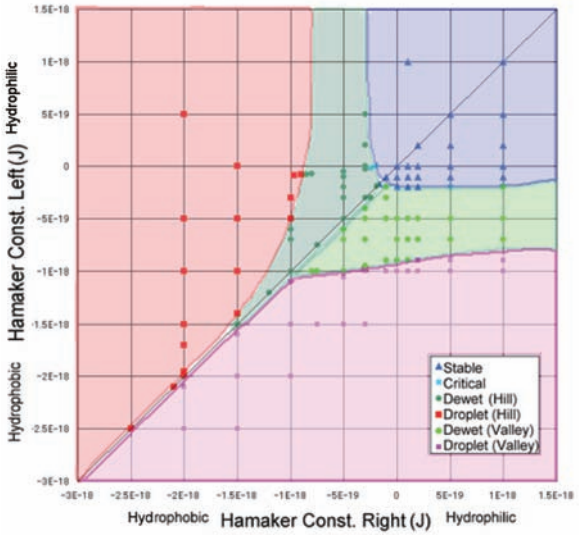

Fig. 13 Dewetting window for sinusoidal surface.

Fig. 14 visualize the dewettability of the film on a flat surface, sinusoidal surface and terrace shape surface. The horizontal axis corresponds to the Hamaker constant on the right side and the vertical axis corresponds to that on the left side. For a curved surface, the hill side is fixed to the right. In these figures, the left and/or bottom of axes represents the most hydrophobic condition. For the flat surface (Fig. 12), it is symmetric around the center so that the graph area is symmetric around the 45 degree line. It is found that the liquid dewets when a Hamaker constant on the right side is more hydrophobic than $-2x10^{-19}$J even if the one on the left side is also hydrophobic, as long as the two constants are different. In other words, it is not necessary that a Hamaker constant on the left half to be positive. Another finding is incomplete dewetting that occurs with overly strong Hamaker constants. However, these strong Hamaker constants are difficult to attain in actual practice.

Fig. 13 shows the results of a sinusoidal surface, which is similar to the flat surface case except for the dewettability on the 45 degree line. As the system is no longer symmetric around the two-surface-boundary, the difference from flat cases appears even when two Hamaker constants are the same. Because the surface shape of a coated film has a curvature, capillary force is the initial driving force to flatten the surface, namely to dewet, a pressure gradient with the same disjoining pressure at the boundary with the same Hamaker constants can be different at the point.

When the inter-surface force is strong enough, incomplete dewetting that forms droplets can also occur in the terrace surface case. The terrace shape case shown in Fig. 14 is basically similar to a flat surface case with the exception in the hydrophobic part at the valley of the terrace. In this case, hydrophobicity repels a liquid upward to the right hill although capillarity moves a liquid to the left valley, resulting in a very slow dewetting motion that might be the reason of complete dewetting free from drop formation. Finally, the author acknowledges that the weak effect of the surface shape appears to change the critical Hamaker constant to $-1x10^{-19}$J from $-2x10^{-19}$J for the flat surface.

5. Conclusion

The study of the dewetting process on hydrophobic and hydrophilic surfaces by changing parameters shows that the process is controlled by the mutual effects between the capillary and inter-surface forces. Also the results suggest that a large difference between the two Hamaker constants is not necessary but a reasonable hydrophobicity is necessary. The wider area of complete dewetting in Fig. 14 is a result of slower dewetting caused by hydrophobicity that moves the liquid against the opposing capillary force. Although these findings are helpful to find good conditions for dewetting, it is hard to estimate the practical Hamaker constants for actual systems. Future experimental confirmation of the theory is necessary for this study.

References

1) Suzuki, K. et al. All-printed Organic TFT Backplanes for Flexible Electronic Paper. International Symposium on Electronic Paper 2010 (2010).
2) Maeda, H. Printed Organic TFT with High Operating Voltages for Active-Matrix Driven Electronic Papers. International Symposium on Electronic Paper 2010 (2010).
3) Sharma, A.; Jameel, A.T. Nonlinear Stability, Rupture, and Morphological Phase Separation of Thin Fluid Films on Apolar and Polar Substrates. J. Coll. Intterf. Sci. **161**, 190-208 (1993).
4) Sharma, A.; Reiter, G. Instability on Thin Polymer Films on Coated Substrates: Rupture, Dewetting, and Drop Formation. J. Coll. Interf. Sci. **178**, 383-399 (1996).

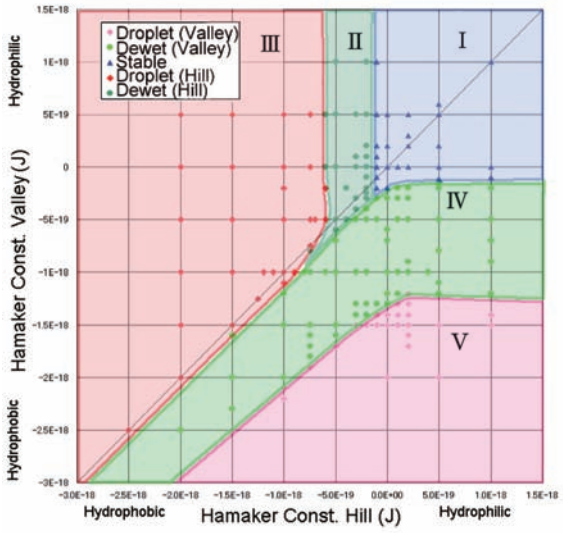

Fig. 14a (Top) Dewetting window for terrace shaped surface.

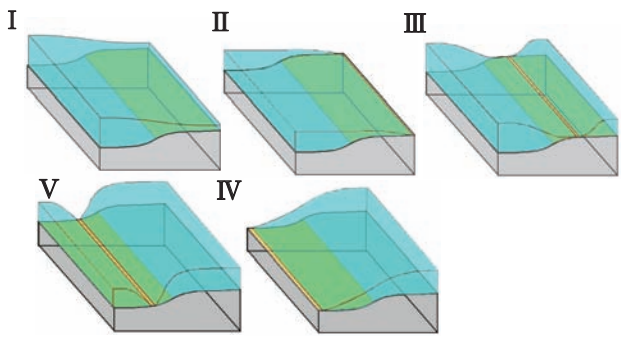

Fig. 14b (Bottom) Final shape of a liquid film.

5) Kargupta, K.; Sharma, A. Dewetting of Thin Films on Periodic Physically and Chemically Patterned Surfaces. Langmuir. **18**, 1893-1903 (2002).
6) Owens, D.K.; Wendt, R.C. Estimation of the Surface Free Energy of Polymers. J. Appl. Polym. Sci. **13**, 1741-1747 (1969).
7) Fowkes, F.M. ADDITIVITY OF INTERMOLECULAR FORCES AT INTERFACES. I. DETERMINATION OF THE CONTRIBUTION TO SURFACE AND INTERFACIAL TENSIONS OF DISPERSION FORCES IN VARIOUS LIQUIDS. J. Phys. Chem. **67**, 2538-2541 (1963).
8) Williams, M.; Davis, S.H. Nonlinear Theory of Film Rupture. J. Coll. Intterf. Sci. **90**, 220-228 (1982).

Postscript

We received many more papers for this issue than in typical years. To publish all of them was impossible because of the limited space. It was also difficult to determine the papers to be published as all of them were excellent. In the end, fifteen papers newly written for this journal and thirteen papers reproduced from recently released science and technology journals were selected, based on a very thin line, that is close to my own personal taste. At the end of the volume is a list of our papers on many technological findings which contribute to the progress of science and technology, published or submitted at conference presentations or to journals. We have integrated and enhanced science and technologies from inside and outside of the company to develop diverse application fields. I would be very pleased if this journal is able to show the vitality of the research and development we carry out.

(Chief Editor, Yoshio Inagaki)